An Optimal Kinetic Impactor Concept for Planetary Defense

Luca Elbracht

Delft University of Technology

TU Delft

OHB

An Optimal Kinetic Impactor Concept for Planetary Defense

by

Luca Elbracht

in partial fulfillment of the requirements for the degree of

Master of Science in Aerospace Engineering,

to be defended publicly on Friday, August 27th 2024 at 13:00.

Chairman:	A. Cervone PhD,	TU Delft
Supervisors:	Dr. ir. J. Bouwmeester,	TU Delft
	V. Schöneich M.Sc.,	OHB System AG
Independent examiner:	Dr. ir. B. Root	TU Delft

An electronic version of this thesis is available at `http://repository.tudelft.nl/`.

TU Delft

Preface

The thesis project was carried out as a collaboration between OHB System AG and TU Delft. In May of 2023 I was finishing up my full-time year at Delft Aerospace Rocket Engineering and started to explore opportunities for a master thesis with an industry partner. I was lucky enough to find the project called ”Astraea”, started by Viktoria Schöneich at OHB. OHB is fostering internal innovation and research through so called ”Blue Sky Projects”. The kinetic impactor for planetary defense was initially investigated by Viktoria, until it was turned into a master thesis topic and I got hired to work on it. Initially, the topic of the thesis was more focused on the structural design and shock transmission during the impact on the asteroid. Early on, it was discovered that the scope of the thesis would change, switching emphasize to the initial design and optimal deployment options for the kinetic impactor. I needed some time to adjust to the topic and figure out which questions are worth answering. After moving to Bremen, the thesis work lasted from November 2023 until July 2024.

I would like to thank Viktoria Schöneich and Jasper Bouwmeester for their supervision, as well as Rolf Janovsky for his critical feedback.

Thank you to Jaimy Thielen, Giorgio Balbo, Mateo Caruso, Loek Sanders, and Noah Tarbah for their friendship during my six years in Delft. Inga, thank you for your support and always being there for me. All of this would not be possible without my family, Mama, Papa, und Jana.

Luca Elbracht
Bremen, July 2024

Summary

Planetary defense from asteroid impacts gained recent publicity due to the Double Asteroid Redirection Test (DART) in 2022, the first successful deflection attempt of a Near-Earth Asteroid. Protecting Earth from potentially hazardous objects is a vital capability and the only large-scale natural disaster that can be prevented by available technology. The kinetic impactor is the simplest and most promising method to alter the course of an asteroid and prevent an Earth impact. A kinetic impactor deliberately collides with the asteroid, transferring its kinetic energy to the object, without the use of explosives or relying on slow-acting effects. In contrast to gravity-pull or radiation pressure methods, the kinetic impactor acts immediately and effectively.

The purpose of this thesis is to investigate the inital design of a kinetic impactor and its deployment architecture. An important effect during an hypervelocity impact of a spacecraft on a porous or rubble-pile asteroid is the momentum enhancement due to ejecta. The momentum transferred to an asteroid during the impact is enhanced by the mass of ejecta thrown out in the opposite direction of the impactor. Due to this effect, the momentum transfer exceeds the initial incident momentum of the impactor. A scaling law is implemented, which quantifies the so called β-factor of the impact, and validated with observations of the full-scale DART mission. The scaling law accounts for the obliquity of an impact and the asymmetry of the ejecta curtain, and is furthermore extended with the effect of ejecta trajectory bending due to gravity. A sensitivity study is performed to identify the driving parameters of the β-factor. The spacecraft momentum is identified as an influential parameter, which is positively correlated with the impact efficiency, and is the easiest to control by selecting an optimal mission architecture.

From a survey of possible mission configuration, seven realistic candidates are identified, numbered from ID1 to ID7. For each configuration the velocity change transferred to the asteroid is evaluated and used for quanitifying the deflection performance. The first configuration is an assembled impactor, which means that the launcher second stage is kept attached to the spacecraft for the whole mission duration and therefore enhances the impact mass. The second configuration is a classic impactor, without the second stage and directly inserted on an interplanetary trajectory by the launch vehicle. An investigation is done on the departure from Earth, where the spacecraft on-board propulsion system is used to deliver the velocity change necessary to intercept the asteroid. ID3 and ID4 are respectively departing from a circular parking orbit and a geostationary transfer orbit (GTO). ID5 is travelling to the asteroid via a low-thrust spiral, and ID6 and ID7 use a solid kick stage motor to depart from Earth.

The interplanetary transfer trajectory to the asteroid is obtained by solving Lambert's problem. For the low-thrust spacecraft, an equivalent formulation of Lambert's problem is implemented, utilizing exponential sinusoids as a shape-based method. The method is verified with existing implementations in literature. The asteroid target is filtered from a database published by the Minor Planet Center. The deflection performance for each configuration is quantified for a population of a large number of asteroids by bootstrapping the catalog of existing asteroids. The average deflection performance of each configuration was determined for a large number of potentially hazardous asteroid. In a subsequent trade-off, informed by the performance results, the assembled impactor is selected and the preliminary requirements and driving challenges are identified.

Contents

List of Figures

List of Tables

Nomenclature

Abbreviations

Abbreviation	Definition
AIDA	Asteroid Impact and Deflection Assessment
AKI	Assembled Kinetic Impactor
AOCS	Attitude and Orbit Control System
ARM	Asteroid Redirect Mission
AU	Astronomical Unit
C&DH	Command and Data Handling
CKI	Classic Kinetic Impactor
COMM	Communication subsystem
DART	Double Asteroid Redirection Test
DI	Deep Impact
EKI	Enhanced Kinetic Impactor
EOL	End of Life
EPS	Electrical Power System
ESA	European Space Agency
GEO	Geostationary Orbit
GTO	Geostationary Transfer Orbit
GNC	Guidance Navigation and Control
LEO	Low-Earth orbit
LCROSS	Lunar Crater Observation and Sensing Satellite
MMH	Monomethylhydrazine
MON	Mixed Oxides of Nitrogen
MPC	Minor Planet Center
NASA	National Aeronautics and Space Administration
NEA	Near-Earth Asteroid
NEC	Near-Earth Comet
NEO	Neart-Earth Object
NEXT-C	NASA's Evolutionary Xenon Thruster-Commercial
PHA	Potentially Hazardous Object
SPH	Smoothed Particle Hydrodynamics
STRUCT	Structure subsystem
TCS	Thermal Control System
TMTC	Telemetry and Telecommand
TRL	Technology Readiness Level

Symbols

Symbol	Definition	Unit
a	Semi-major axis, projectile radius	[m]
b	Material fitting constant	[-]
C	Projectile coupling parameter	[-]
C_1	Material fitting constant	[-]
g	Surface gravity	[m/s^2]
G	Gravitational constant	[Nm^{2}kg^{-2}]

Symbol	Definition	Unit
J	Deflection	[m/s]
k	Material fitting constant	[-]
K_s	Ejecta mass scaling	[-]
M	Remaining mass of the asteroid after impact	[kg]
m_{sc}	Spacecraft mass	[kg]
m_a	Asteroid mass	[kg]
m_{impact}	Impact mass	[kg]
M_e	Total ejected mass	[kg]
n	Ejecta mass velocity distribution slope	[-]
n_1	Minimum ejection extent factor	[-]
n_2	Maximum ejection extent factor	[-]
P	Material fitting constant	[-]
p_{ej}	Ejecta momentum	[kg m/s]
p_m	Momentum contribution of a mass element	[m/s]
q	Perihelion distance	[m]
Q	Aphelion distance	[m]
Q^*	Impact characteristic energy	[J/kg]
Q_d^*	Dispersion energy	[J/kg]
Q_s^*	Shattering energy	[J/kg]
r	Radial distance from impact point	[m]
R_{Earth}	Earth radius	[m]
R	Crater radius	[m]
U	Impact speed	[m/s]
v	Ejecta speed	[m/s]
v^*	Minimum ejection velocity	[m/s]
v_{inf}	Hyperbolic excess velocity	[m/s]
$v_{sc,i}$	Spacecraft relative velocity to the asteroid	[m/s]
v_f	Final asteroid velocity after impact	[m/s]
w	Distance from impact point in terms of projectile radius	[-]
Y	Cohesive strength	[Pa]
α	Ejection angle	[rad]
β	Momentum enhancement factor	[-]
Δv	Velocity change	[m/s]
δ	Projectile density	[kg/m^3]
ζ	Azimuth angle	[rad]
θ	Impact angle	[rad]
μ	Velocity scaling exponent	[-]
ν	Density scaling exponent	[-]
ρ	Target density	[kg/m^3]
Φ	Porosity	[-]

1 Introduction

Deflecting an asteroid with a kinetic impactor requires the deployment of the spacecraft into an interception trajectory with the asteroid. The objective of the thesis is to investigate the optimal operational configuration and deployment method, while integrating an estimation of the impact efficiency. In the following, the background and motivation for the thesis is discussed.

Although rare, asteroid impacts pose a serious threat to life on Earth. An historic example is the extinction event roughly 65 Mio years ago at the end of the Cretaceous period, which is highly likely to have been caused by an asteroid, impacting in the area of modern day Mexico [44]. More recently, an airburst event of asteroidal origin near the city of Chelyabinsk in Russia made the news in 2013. Even though the size of the object was relatively small, with a diameter of about 16 to 19 m, glass windows were shattered up to 120 km away from the explosion [38].

In recent years, space agencies made efforts towards planetary defense. For the first time in human history, the technology is available to prevent an asteroid impact. An example of an active planetary defense mission is the NASA Double Asteroid Redirection Test (DART). DART is a demonstration of a kinetic impactor. On 26th Septmeber 2022 the spacecraft successfully collided with Dimorphos, which is the smaller member of the binary asteroid system 65803 Didymos. The orbital period of Dimorphos around Didymos was reduced by 33 minutes [8], successfully demonstrating the deflection capabilities of a kinetic impactor.

The phenomenon of momentum enhancement during the impact was predicted for DART and confirmed by the test. Momentum enhancement refers to the effect of asteroid material that is ejected during the cratering process. This material is known as ejecta. The impact energy causes shattering and subsequent excavation of debris with a mass multiple times the mass of the impactor [16]. From an energy perspective, the kinetic energy of the impactor is partially redirected in the ejecta being accelerated in the opposite direction of the impactor. The ejecta carry momentum and reach a sufficiently high velocity to permanently escape the gravitational influence of the asteroid. Effectively, the total momentum transferred to the asteroid exceeds the incident momentum of the kinetic impactor, which is quantified by the factor β. The definition of β is the ratio of total transferred momentum to impactor momentum [23]. A value of 1 refers to the hypothetical situation that no ejecta are thrown out during the crater formation and the momentum transferred to the asteroid is equal to the momentum of the incoming spacecraft. Whenever β is larger than one, the debris that is thrown out with at least escape velocity contributes to the momentum transfer, making the impact more efficient. After the DART impact, the β-factor was determined to be 3.61, hinting at a highly efficient cratering process [8].

The proposed mission is a kinetic impactor, focusing on utilizing the momentum enhancement effect, to divert an incoming asteroid from a collision trajectory with Earth. The goal is to set up a design framework, that includes an impact calculation, mass estimation, launch vehicle constraints and the interception trajectory to the target. To allow for quick evaluations, the estimation of the impact parameters, most importantly the transferred momentum and the β-factor, are based on scaling laws derived from impact experiments and simulations. The design framework is then used to manually optimize

the design for the transferred momentum, by adjusting the geometry, mass and speed of the impact as well as the trajectory.

The effect of hypervelocity impacts on asteroids is an ongoing field of research. Widely accepted scaling laws for large-scale impacts date back to the work of Holsapple and Housen, who developed their relations based on laboratory-size impacts [26]. In preparation of the DART mission a range of simulations were carried out using hydrocodes. Hydrocodes are numerical methods that can describe the behaviour of material in highly dynamic events, such as a spacecraft impact. In recent years, the traditional scaling laws were expanded by simulation data with DART as a motivating case study, such as the work by Stickle et al. [45]. The simulated events are orders of magnitude larger in size than laboratory impact experiments, providing crucial data to confirm the validity of scaling laws. A relevant research area is therefore the application of a suitable scaling law for the kinetic impactor and verifying the results with the DART impact.

The properties of the asteroid material have a large influence on the efficiency of the impact, specifically the porosity, cohesive strength and density. Thanks to material samples returned by the Hayabusa missions and OSIRIS-REx, these properties can be constrained and applied to the impact calculation. The cohesion can be inferred from rotational velocity of asteroids. The cohesive force has to be at least as high as the centrifugal force of the spinning body. The density of asteroids can be determined by measuring the size and gravity field of asteroids, just like the Hera spacecraft is intended to investigate Dimorphos, the target of DART. Hera is expected to launch in 2024 and will observe the effects of the DART impact on the asteroid [32]. The material fitting constants used in the scaling laws are evaluated in the light of recent findings on asteroid composition and applicable values are selected for the chosen scenario.

An interception trajectory of the spacecraft with the target has to be found. The relative speed of the impactor with respect to the asteroid as well as the impact angle are important results and direct inputs for the impact calculation. The interception trajectory is evaluated in conjunction with the impact calculation to estimate the total transferred momentum.

The spacecraft design is not complete without taking into account the launch vehicle constraints, as well as the subsystem selection for the spacecraft itself. With interplanetary missions such as DART and Hera as the baseline, the critical requirements of the spacecraft are formulated.

The body of research on kinetic impactors for planetary defense is contributed to by combining the impact calculations with the spacecraft design. In the case of DART, the impacting spacecraft was a simple rectangular bus with no optimization towards the generated ejecta. By taking into account the momentum enhancement effect via applicable scaling laws an additional discipline is added to the spacecraft design. The model shall be able to support the design of a kinetic impactor, in light of the asteroid impact threat.

While the impact modelling is an important analysis in itself, it cannot be treated out of context of the whole mission. The disciplines that are analysed are the asteroid properties, trajectory, impact modelling, launch vehicle and spacecraft. The objective is to maximise the change in orbital velocity of the asteroid via a kinetic impact. The velocity change is used to measure the deflection performance.

The **objective** of the thesis is therefore:

> The objective is to design an enhanced kinetic impactor concept for planetary defense by optimizing the mission for the deflection performance.

Subsequently, the research questions and subquestions are formulated.

> (1) What is the design and mission concept of a kinetic impactor, optimized for the momentum transfer to the asteroid target?
>
> (1.a) What is the high level spacecraft and mission design of the kinetic impactor?
>
> (1.b) What are the sensitivities of the kinetic impactor design with respect to the design variables?
>
> (2) What are the limits of applicability of the proposed kinetic impactor concept?

(2.a) What are the limits of the parametric model implementation for the kinetic impactor design?

(2.b) What is the performance and the limits of the kinetic impactor concept in a realistic asteroid threat scenario?

The outline of the thesis is as follows. First, Chapter 2 analyzes the kinetic impactor mission and determines the design options that are evaluated for their deflection performance. The chapter also discusses the launch vehicle and the mission timeline. The impact modelling, an important step in the thesis work, is treated in Chapter 3. The implementation, verification and validation is discussed as well as the convergence of the scaling laws. Chapter 4 discusses the asteroid, how the target is selected and the dispersion threshold. Next, the methods to determine the deflection performance of the design options are described in Chapter 5. Based on the performance results, an informed trade-off is performed on the overall architecture of the spacecraft and the subsystems are treated in Chapter 7. Lastly, conclusions, limitations and an outlook on future work is given in Chapter 8.

2

Mission Analysis and Design

In light of the successful deflection attempt by DART, and the very real threat of asteroid impacts, the capabilities of asteroid avoidance shall be expanded towards an effective planetary defence system. The efforts towards developing such a system will compliment the initiatives of other nations, as carried out by China [51] and the US [7].

The mission need statement is formulated as follows.

> The global space industry needs to develop a planetary defense system to respond to the global impact threat of Near Earth Objects. Objects as small as 150m in diameter can cause the destruction of large urban areas with an explosive yield exceeding that of every man-made explosion. Such an object impacts Earth about every ten thousand years years [35].
>
> The spacecraft needs to travel to the object and deflect it by kinetic impact such that the asteroid misses Earth.

In order to fulfill the mission, a spacecraft is proposed that has to fulfill certain functions. An overview of the functional flow is given in Figure 2.1. At the start of the mission, the spacecraft is deployed by an available launch vehicle. To reach the asteroid some time before the predicted impact, the spacecraft is leaving Earth's orbit. During the mission, the spacecraft shall be available to receive commands and send telemetry. When the spacecraft approaches the asteroid, it shall navigate to the target and capture images of the surface. The operational mission is complete when the impactor strikes the target.

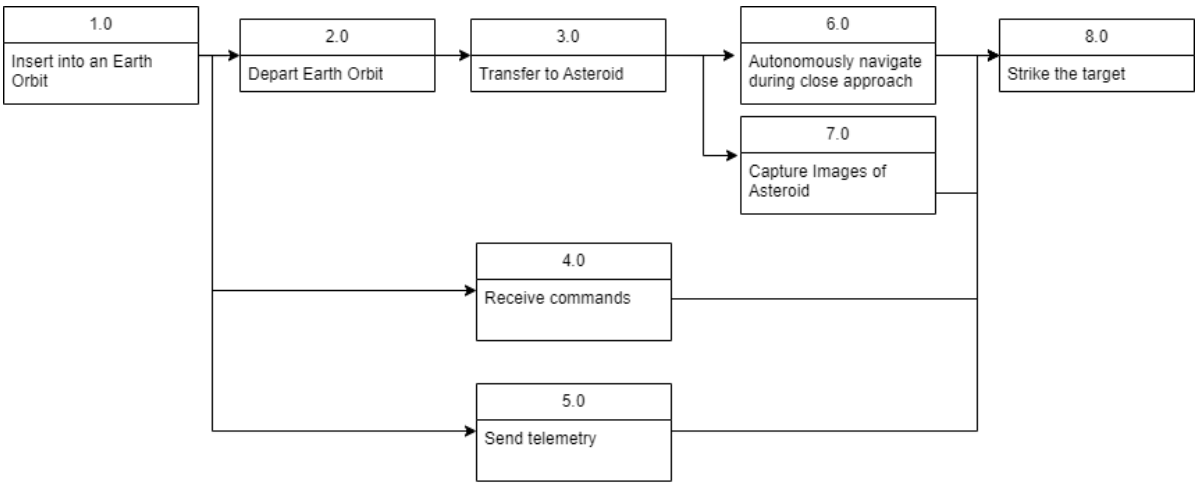

Figure 2.1: The functional flow of the spacecraft.

In the following sections, the preliminary mission design options are detailed. First, the mission phases and their characteristics are detailed in Section 2.1. The mission stakeholders and their importance are given in Section 2.2. Afterwards, options for the spacecraft design (Section 2.3), transfer trajectory (Section 2.4) and launch vehicle (Section 2.5) are given. The transition from the launch phase to the mission phase is discussed in Section 2.6. The selected configuration and how to quantify their performance is given in Section 2.7. The performance figure for the configurations is explained in Section 2.8.

2.1. Mission phases

The phases of the mission are given in Figure 2.2. The event that initiates the mission is the hypothetical discovery of an Earth-impacting asteroid. When the asteroid is detected, a solution for the orbit is obtained and a high impact probability is calculated. The asteroid is assumed to be part of the NEO population, with an orbit that crosses the Earth's path. Atens and Apollos is the designation of the respective asteroid groups that comply with these conditions. A detailed description of the target selection is given in Section 4.1.

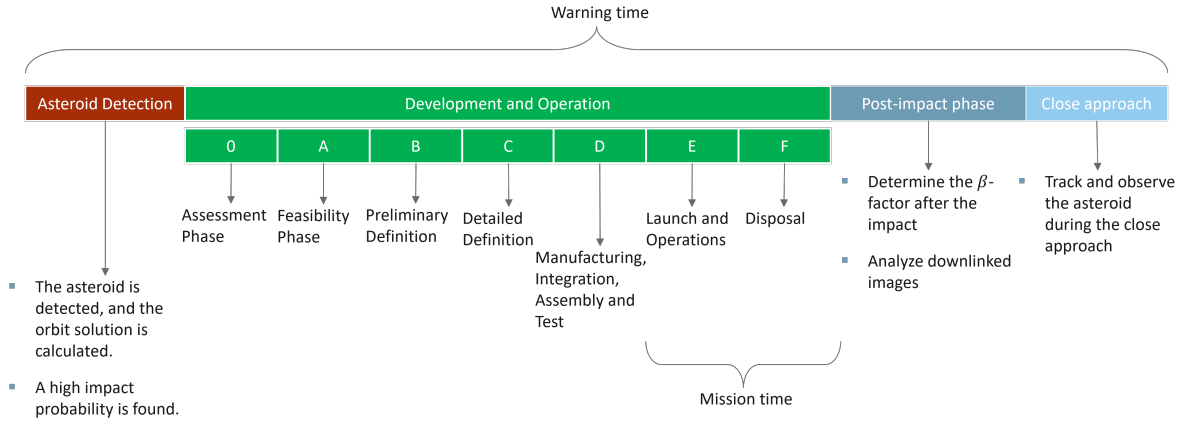

Figure 2.2: The timeline of the mission.

The development of the spacecraft, from the early assessment phase to manufacturing, is designated by the phases 0 to D. With the developments presented in this thesis, which are not based on a specific threat, the time frame of phases 0 to D might be reduced, once a real threat is discovered. Phase E comprises the launch and operations. The phase E is further broken down into E1 and E2, as shown in Figure 2.3. After the spacecraft is successfully deployed, the cruise phase starts, which can last from several weeks to months.

During cruise, some operational tasks have to be performed. In order to achieve a high accuracy in orbit determination, a combination of radio tracking and on-board optical navigation is employed.

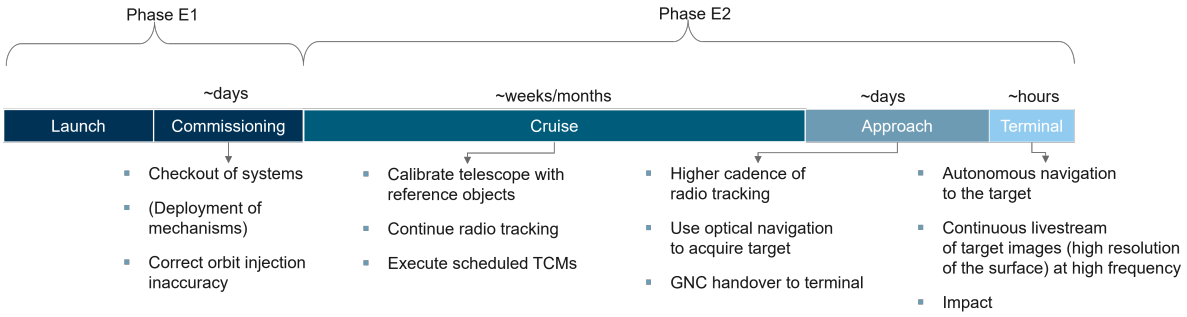

Figure 2.3: The phase E of the mission.

Since the spacecraft has to impact on a small target, on a planetary scale, strict requirements on guidance and navigation are imposed. With the DART mission as an example, Delta Differential One Way ranging (DDOR) is recommended as radio tracking method for high accuracy. Combining it with optical navigation yields a high accuracy orbit solution.

Following the cruise phase, the spacecraft enters the approach, which is characterized by the spacecraft being able to resolve the target with a telescope. The cadence of radio tracking is increased to further reduce the positional error. A critical point is the handover from the approach phase to the terminal phase. The handover uncertainty of the orbit solutions needs to comply with a requirement imposed by the autonomous navigation system.

Like DART, the terminal phase requires an autonomous navigation system that guides the spacecraft to the target. The communication delay from the spacecraft to the ground station in combination with the high impact speed prohibits the spacecraft to be remote controlled for the last hours of the mission. For the DART mission, the one-way delay was approximately 70 seconds [43]. Nevertheless, the spacecraft shall continuously downlink images of the asteroid surface because of their scientific value. The autonomous guidance system was demonstrated to perform well during the DART mission and is assigned a high Technology Readiness Level (TRL) [5].

After the impact, some actions are required to successfully close out the mission. The β-factor can be determined by comparing the deflected and original orbit of the asteroid. The close up images of the surface shall be made available to the planetary science community. It is assumed that asteroid will later have a close approach with Earth, which is an opportunity for further observations. Radar measurement and optical observations reveal the asteroid shape and crater topology to further constrain the target properties.

2.2. Stakeholders

The stakeholder identification helps in clarifying the requirements and expectations related to the kinetic impactor mission. An overview of the stakeholders is given in Figure 2.4.

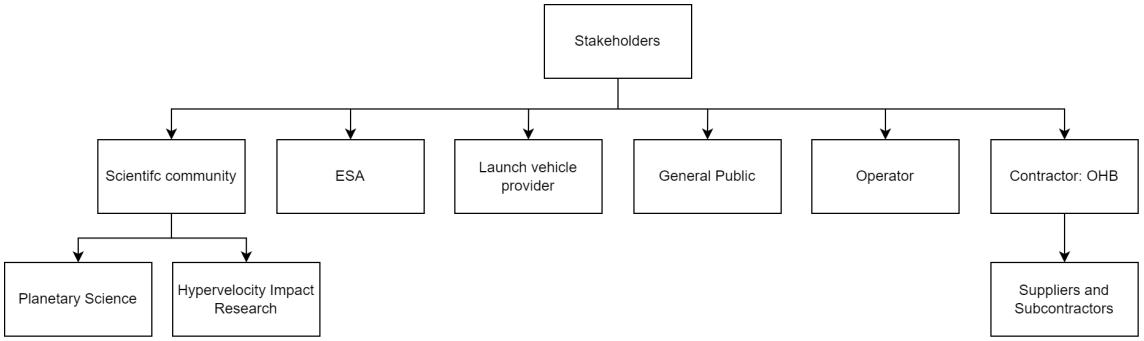

Figure 2.4: The stakeholders of the kinetic impactor mission.

From a scientific perspective, the mission is valuable for planetary scientists studying the composition and origin of asteroids. Multiple asteroids have been visited, such as Bennu, Ryugu, Itokawa, Dinkinesh and others. Some samples have been collected and a small impactor was carried by Hayabusa 2, creating an artificial crater on Ryugu [2]. In light of the DART mission, a whole range of impact simulations were performed to predict the outcome. With DART as the only full scale hypervelocity deflection attempt, a second data point is provided by an enhanced impactor mission. The imagery generated by the camera needed for autonomous navigation can be of high interest for planetary scientists.

The launch vehicle provider puts requirements on the spacecraft system. In practice, the size and mass of the spacecraft are limited by the launcher capabilities. A suitable launch vehicle adapter is required and the spacecraft structure needs to be able to withstand the acoustic load, accelerations and vibrations.

The general public has an interest in protection from natural disasters. Compared to other events, like Earth quakes, volcanic eruptions and droughts, the risk of an asteroid impact can be feasibly mitigated

with available technology. The public needs to be informed about the risk and capabilities of the mission.

The European Space Agency has issued multiple missions to small bodies in our solar systems, such as the upcoming Hera spacecraft visiting the impact site of DART on Dimorphos, or the successful Rosetta comet lander. In light of the close approach of Apophis in 2029, ESA proposed the RAMSES mission to study the asteroid [31]. Therefore, crucial experience in interplanetary missions exists in Europe. ESA as the customer of the mission puts requirements on scientific return and cost.

The operator is responsible for ground communication once the system is deployed. Adjustments to the mission, in case of unexpected events, are carried out by the operator. The status of the systems is observed and necessary actions are taken, such as enabling safe mode or triggering a mission abort.

The prime contractor for the mission is assumed to be OHB, together with necessary suppliers and subcontractors. OHB is carrying out the design and manufacturing, before handing the finished spacecraft over to the launch vehicle provider and operator.

2.3. Design options

The spacecraft, on the highest level, has to fulfill the function of navigating to the target and impacting it. In order to do that, communication, guidance, navigation and other subsystems are required in order to achieve the mission objective.

The two main options for the spacecraft are identified as the Assembled Kinetic Impactor (AKI) and the Classic Kinetic Impactor (CKI). The concept of the AKI entails that the second stage of the launch vehicle is not separated from the spcecraft after commissioning. The second stage, weighing several tons for a commercially available launcher, is kept attached and therefore increases the effective impact mass. The concept was proposed by Wang et. al. [51].

A heritage mission is the Lunar Crater Observation and Sensing Satellite (LCROSS). The mission aimed at creating an impact crater on the Moon and analysing the debris cloud to search for signs of water ice at the sout pole. LCROSS was a dual launch with the Lunar Reconnaissance Orbiter (LRO). The LRO was dispatched early in the mission and started its own transfer orbit to the Moon. LCROSS consisted of the shepherding spacecraft connected to the Centaur upper stage. Before reaching the surface of the Moon, the upper stage was separated from the craft, such that the shepherding spacecraft could observe the impact, before hitting the surface as well. The main structure of the shepherding spacecraft is a multi-launch adapter for smaller payloads, which is a standard part offered by United Launch Alliance (ULA). The cylinder has multiple ports, where the different payloads are intended to be attached. The shepherding spacecraft was designed around the payload adapter ring and consists of multiple panels that are mounted to the payload ports of the structure. Furthermore, body mounted solar panels were used and a reaction control thruster system was added [33]. The structure of LCROSS is shown as an example in Figure 2.5.

The impact accuracy requirement of LCROSS was ± 10 km [17], which, in the context of asteroid deflection, is one or two magnitudes too large. The impact accuracy is identified as a driving requirement for the mission. The performance of an assembled impactor compared to a CKI is within the scope of this work and is discussed in Chapter 6.

2.4. Transfer trajectory

The spacecraft has to travel from Earth to the asteroid. In order to do that, it needs to follow a heliocentric trajectory that ends at the target. The options for the cruise phase of the mission are summarised in Table 2.1.

A straightforward option is a ballistic elliptical transfer trajectory from Earth to the asteroid. In the simplest case, the transfer is determined by an impulsive shot at departure and then follows a Keplerian trajectory. With the patched-conics approach, the velocity change to achieve the trajectory is determined.

In order to improve the momentum transfer to the asteroid, it is an option to use on-board propulsion to accelerate the impactor before striking the target, called ”accelerated elliptical transfer trajectory” in Table 2.1. In an attempt to increase the impact velocity, the spacecraft can carry a solid propellant

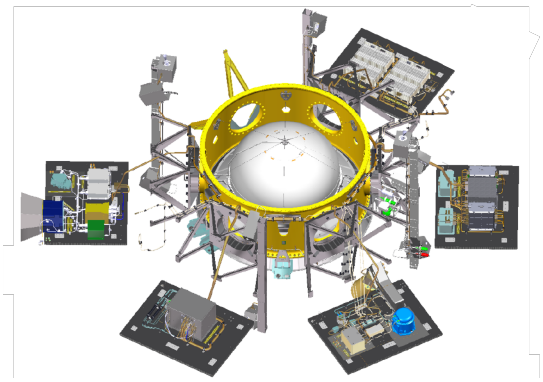

(a) The disassembled state of the shepherding spacecraft, showing the panels that are attached to the payload ring.

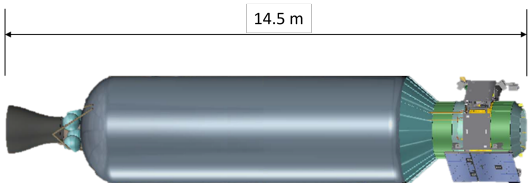

(b) The shepherding spacecraft on top of the Centaur upper stage.

Figure 2.5: The structure of LCROSS is shown in Figure 2.5a, with the payload ring in the center and the electronics panels. Figure 2.5b shows LCROSS attached to the Centaur upper stage.

kick stage and use it to accelerate shortly before the impact. The advantage is that a higher impact velocity can be achieved. As detailed in Section 7.4.1, achieving an impact accuracy good enough to hit a small target is a complex operational undertaking. Using a solid propellant kick stage in the most critical phase of the mission is detrimental to the impact accuracy. With inherent uncertainties in thrust alignment, mass flow and influence on the center of gravity, the use of a solid motor will demand corrections of trajectory errors in the terminal phase. Therefore, the accelerated trajectory is not treated in this thesis.

Another feasible option is low-thrust transfer trajectory. A high TRL commercial propulsion system is the NEXT-C electric thruster [15], which was already used on the DART spacecraft. Using an electric thruster gives the mission designer more flexibility, because the trajectory can be more effectively altered with a thruster than by only relying on the reaction control system. The advantage of electric propulsion is the higher specific impulse compared to chemical propellant options. A high specific impulse means lower fuel consumption and results in a higher impact mass.

An interesting option is H-reversal. The name refers to inverting the angular momentum of the transfer orbit, usually denoted by H. Performing an H-reversal changes the direction of the orbit from prograde to retrograde. This can be advantageous for the deflection, as the vectorial sum of the orbital velocities of the spacecraft and the asteroid is much higher compared to a situation where a spacecraft ”catches up” to the target. The H-reversal, in the context of planetary defence, was proposed for a solar sailing spacecraft [19]. H-reversal was also found to be the winning concept in the first edition of the trajectory optimization competition by ESA for a nuclear-electric spacecraft, which achieved the reversal with multiple gravity assists [37].

The H-reversal promises a high deflection performance, at the disadvantage of higher planning effort and reduced flexibility. However, the idea of reversing the orbital direction remains an interesting concept for further studies, but was not used further in the analysis done in this study.

2.5. Launch vehicle

The launch vehicle selection is limited to existing and in-development launchers with medium to heavy-lift launch capabilities. The selection includes Arianespace’s Ariane 64, SpaceX’s Falcon Heavy and Falcon 9, and United Launch Alliance’s Vulcan Centaur. The main considerations for selecting the launch vehicle is availability for a European mission, which mostly excludes Russian and Chinese options.

Ariane 64 is the newest development of the Ariane series and awaiting its maiden flight in 2024 [20]. The indication ”64” stands for 4 solid boosters, representing the highest payload mass variant of the rocket.

Falcon 9 is the a medium-lift launch vehicle by SpaceX and Falcon Heavy is three Falcon cores com-

Table 2.1: A qualitative comparison between the identified cruise options for the transfer trajectory to the asteroid. The colors give an indication of the strengths and weaknesses of each option, with green standing for ”better”, yellow for ”neutral” and red for ”worse”.

	H-reversal	**Ballistic elliptical transfer trajectory**	**Accelerated elliptical transfer trajectory**	**Low-thrust transfer trajectory**
Performance	“Head on” impact is possible	Lower performance compared to other methods	Higher impact velocity	Improved over ballistic trajectory
Flexibility	(Multiple) gravity assists required	Does not rely on flybys or propulsion	Moderate	Higher than the ballistic option
Complexity	High operational effort	Lowest	GNC needs to correct uncertainties	Higher effort in planning and operation

bined to enhance payload capability [10]. Both vehicles have been used for interplanetary missions.

After retiring the Delta and Atlas family, United Launch Alliance is replacing their capabilties with the Vulcan launch vehicle. The first flight in 2024 demonstrated that Vulcan is capable of injecting payload in an interplanetary trajectory [50]. The selected variant is the ”VC6”, with 6 solid boosters and the highest payload capacity.

A comparison between the launch vehicles is given in Table 2.2. All vehicles have the capability to inject a payload in an interplanetary orbit. The excess energy to escape Earth’s orbit and the payload mass are related by a non-linear function. Based on data published by the NASA Launch Services Program [6], the functions are plotted in Figure 2.6.

Table 2.2: Comparison of the selected launch vehicles.

	Ariane 6	**Falcon Heavy**	**Falcon 9**	**Vulcan Centaur**
Variant	Ariane 64 4 side boosters	3 Falcon 9 cores	-	VC6S 6 side boosters
Flown in this configuration?	no	yes	yes	no
Mass to GTO [kg]	11500	26700	8300	14400
Mass to LEO [kg]	20000	63800	22800	25600
Source	[3]	[10]	[10]	[48]

The details of the upper stages for each launch vehicle are also compiled. For the proposed AKI these values are relevant for calculating the impact mass and dimensions of the projectile. The parameters are collected in Table 2.3

Table 2.3: The parameters of the upper stages for the selected launch vehicles. The values are taken from the user guides of the respective launchers [3][10] [48]. The mass of the upper stage is subject to change for different mission profiles.

	Upper Liquid Propulsion Module	**Falcon Upper Stage**	**Centaur V**
Rocket	Ariane 64	Falcon 9/Heavy	Vulcan
Diameter [m]	5.4	3.66	5.4m
Length [m]	13.4	13	11.7
Mass [kg]	6000	4500	5800

2.6. Deployment options

Depending on the exact orbital position of Earth and the asteroid, a certain characteristic energy C_3 is required to put the spacecraft on a transfer trajectory. The required velocity change can either be supplied by the launch vehicle or an on-board propulsion system.

In an opposed scenario, the spacecraft is launched into a circular parking orbit, and the on-board propulsion system has to provide the the required ΔV for departure. A launch vehicle can carry a high

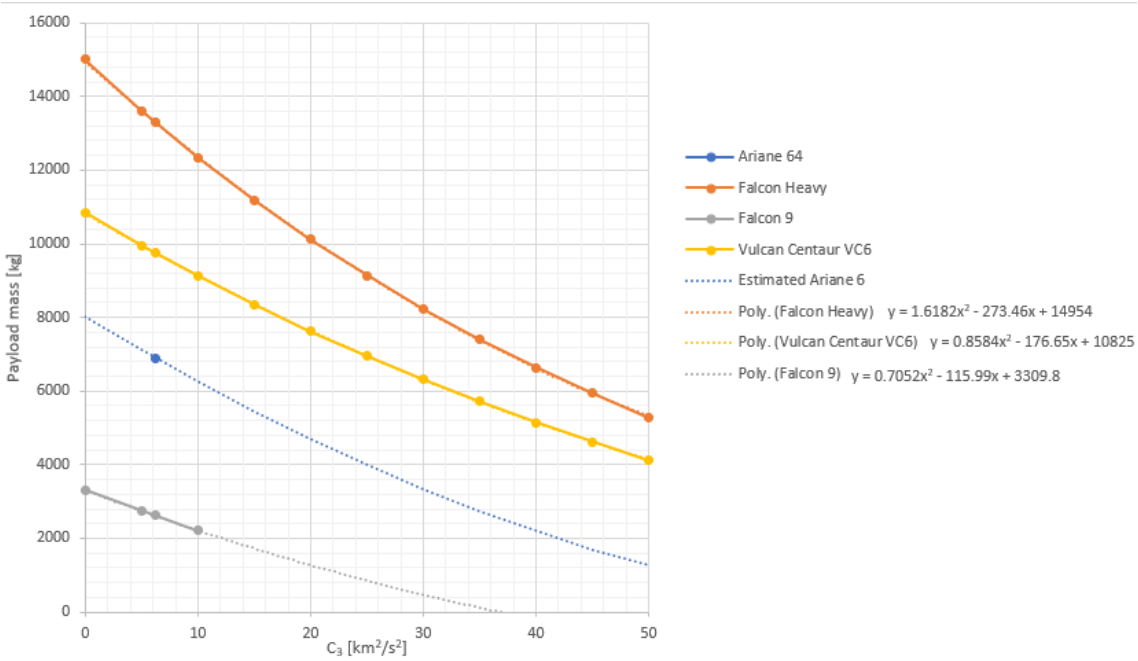

Figure 2.6: The payload mass capabilities versus the characteristic energy. The curves for Falcon Heavy, Falcon 9 and Vulcan are taken from the NASA Launch Vehicle Performance Service [6]. The curve for Ariane 64 is estimated from the data provided in the user manual [3]

.

payload mass into LEO, at the expense of fuel needed for the on-board propulsion.

The other scenario is the direct insertion, in which the launcher provides the total velocity change needed to reach the required orbital energy. Therefore, the payload capability for that scenario is lower, but no on-board propulsion is required, except for trajectory correction maneuvers.

As an intermediate step, a geostationary transfer orbit is selected as a “parking orbit”. This is a high energy elliptical orbit, that is usually used to deliver satellites to GEO. The launcher supplies a larger portion of orbital energy, at the cost of payload capacity.

For the on-board propulsion, a high impulse system is required. The two considered options are a liquid bi-propellant system and solid propellant kick motors. They are selected because of their high thrust, high specific impulse characteristics. The state of the art for liquid bi-propellant propulsion is a MMH/MON system. The hypergolic nature of the propellant mono-methyl hydrazine (MMH) and mixed oxides of nitrogen (MON) as oxidizer ensures spontaneous ignition when the two substances come into contact. It is selected as the reference liquid propulsion system due to its flight heritage and reliability. The chosen system has an average I_{sp} of 321 s. An overview of options is given in Table 2.4.

Table 2.4: Overview of typical chemical in-space propulsion systems, adapted from [52].

Propellant type	Isp [s]	Mass mixture ratio [-]	Thrust level [N]
N2 cold gas	57-65	-	0.001-266
Hydrazine Monoprop	206-235	-	0.02-572
MON/MMH	285-352	1.5-2.1	4-4,000
NTO/MMH	220-317	1.2-2.05	4.5-27,000
NTO/Hydrazine	277-290	1.3-1.65	4.5-100

For the solid-propellant case, a number of kick-stages are considered. The main requirements are that they are still in production, have flight heritage and are commercially available. The solid motors are listed in Table 2.5 and would be used to achieve a high C_3 to intercept the asteroid on its orbit.

Table 2.5: The available solid rocket motors which are still in production. Values are taken from the propulsion products catalog [21].

Solid Motor	Diameter d [m]	Length l [m]	Specific impulse I_{sp} [s]	Burn time t_b [s]	Propellant mass m_{prop} [kg]	Inert mass m_{inert} [kg]	TVC -
STAR 48BV	1.24	2.04	294.2	84.1	2010	154	Yes
Orion 38	0.97	1.34	287.0	66.8	770	93	Optional
Orion 50XL	1.28	3.08	290.7	71	3915	367	Optional
CASTOR 30	2.34	3.66	293.1	149.8	12745	1029	Yes
CASTOR 30B	2.34	4.32	300.6	126.7	12884	999	Yes
CASTOR 30XL	2.34	6.00	294.4	155	24924	1392	Yes

2.7. Operational configurations

The next step in the mission design is to trade-off the mission configurations. The configurations are determined from the design options presented in the previous sections.

The configurations are selected as follows:

1. Choose a launch vehicle from Figure 2.7.
2. Choose a commissioning option, either direkt interplanetary insertion, circular parking orbit or GTO, as given in Figure 2.8.
3. If GTO or a circular parking orbit is selected, select one of the solid motors in Figure 2.9 or a liquid bi-prop system for Earth departure.
4. If direct interplanetary insertion is selected, the available cruise options are the low-thrust transfer trajectory and the ballistic elliptical transfer trajectory.
5. If a circular parking orbit or GTO is selected, then the ballistic elliptical transfer trajectory is the available cruise option. All cruise options are shown in Figure 2.10
6. For the accelerated trajectory, one of the solid motors are selected.

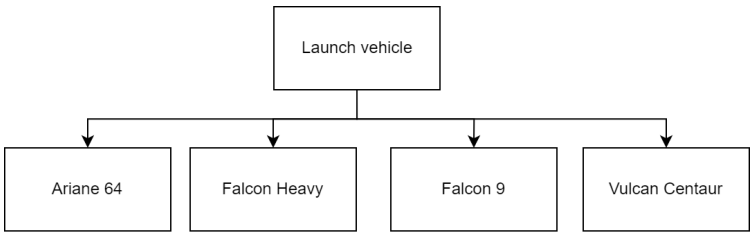

Figure 2.7: The options for the launch vehicle selection.

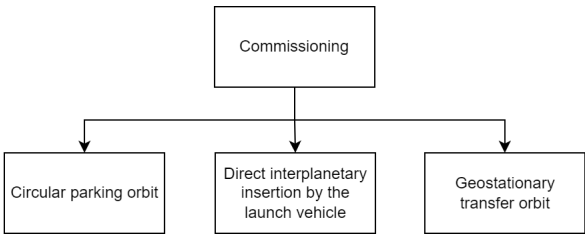

Figure 2.8: The design option tree for spacecraft commissioning

The selected configurations are given an identification number form 1 to 7, which are used throughout the thesis. An overview is given in Table 2.6

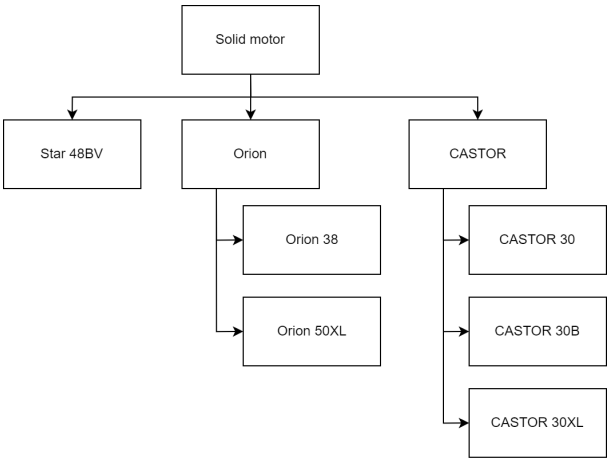

Figure 2.9: The options for commercially available solid motors.

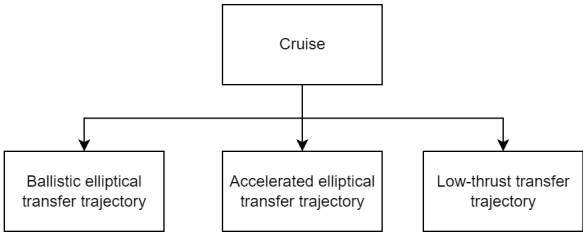

Figure 2.10: The design options for the cruise phase of the mission.

Table 2.6: The design options analysed for their deflection performance in this thesis.

ID	Deployment	Departure	Transfer trajectory	Impactor
1	Direct insertion	Launcher 2nd stage	Ballistic elliptical	Assembled
2	Direct insertion	Launcher 2nd stage	Ballistic elliptical	Classic
3	Circular parking orbit	Bi-propellant	Ballistic elliptical	Classic
4	Elliptical parking orbit (GTO)	Bi-propellant	Ballistic elliptical	Classic
5	Direct insertion	Launcher 2nd stage	Low thrust spiral	Classic
6	Circular parking orbit	Solid motor	Ballistic elliptical	Classic
7	Elliptical parking orbit (GTO)	Solid motor	Ballistic elliptical	Classic

2.8. Figure of merit

The performance indicator for the mission is the velocity change it can give to the target asteroid. Starting from Equation (3.1), with the impact mass m_{impact}, the impact velocity U, the impact efficiency β and the asteroid mass M, the velocity change is given as:

$$J = \Delta v = \beta \frac{m_{impact} U}{M} \tag{2.1}$$

The figure of merit is denoted by J to avoid confusion with other parameters throughout the thesis.

In order to evaluate the figure of merit, a hypothetical scenario is set up with an asteroid target. The process to arrive at the figure of merit is explained in the following. For each step, the inputs and outputs of the calculation are shown in a block diagram and the detailed explanation of the used methods is given in Chapter 5. Only an abbreviated version of the block diagram is shown, with the detailed figure in Appendix B.

The same asteroid target is chosen to compare the performance of each configuration. A range of start dates and times is used to check the figure of merit for multiple mission scenarios. The idea is to find the performance depending on the start date and time of flight, plot them as a contour plot, and then select the start date and time of flight for the highest J.

Due to the unique combinations of Earth and asteroid orbit geometry, the launch opportunity with the lowest C_3 does not necessarily coincide with the highest impulse. Also, in the model it is sufficient to select the launch opportunity with the largest impulse, because the β factor is positively correlated with impact speed and mass. The largest impulse results in the largest β, when the asteroid parameters and impact parameters are kept constant.

The required velocity change of the asteroid in order to avoid an Earth impact can be estimated based on the work of Ahrens and Harris [1]. The assumptions are that the Δv is applied in the direction of motion of the asteroid and the asteroid orbit is near-circular. The time ΔT is the time until impact on Earth. The required deflection distance is at least one Earth radius $R_\oplus$.

$$\Delta v \simeq \frac{R_\oplus}{3\Delta T} = \frac{0.07(m/s)}{\Delta T(yrs)} \tag{2.2}$$

As seen in the plot in Figure 2.11, the required velocity increases when the asteroid approaches Earth. With the setup in this thesis, the time for deflection is between 3 and 7 years, which results in a requirement between 0.01 m/s and 0.024 m/s.

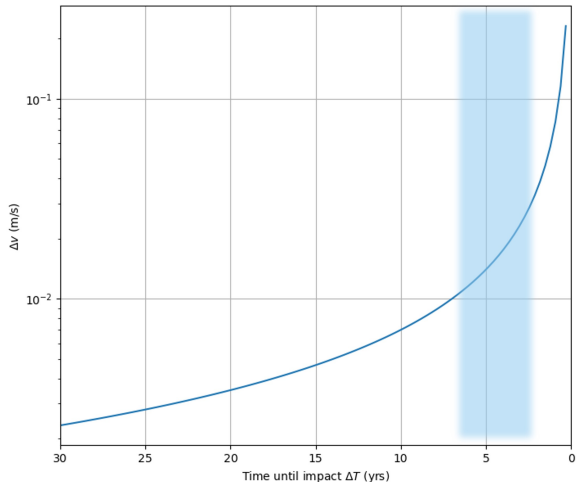

Figure 2.11: The required velocity change given to an asteroid for a succesful deflection by one Earth radius as a function of time left until impact. The shaded area indicates the time range analysed in this thesis.

Generate target

The first step is to generate the asteroid target, as shown in Figure 2.12. The ”asteroid generator” module determines the semi-major axis a, the eccentricity e and the inclination i of a representative NEO. The absolute magnitude, which is a measure of the luminosity of an asteroid, is used to constrain the size of the object. The constraints on the semi-major axis and the aphelion and perihelion distance filter the catalog for objects that cross the Earth's orbit. The last input is a so called seed for the random number generator that generates a random asteroid. The seed is useful for debugging, because when keeping the seed constant, the same random asteroid is generated on every run of the program. The asteroid generator can also select an existing asteroid from the population given in the database.

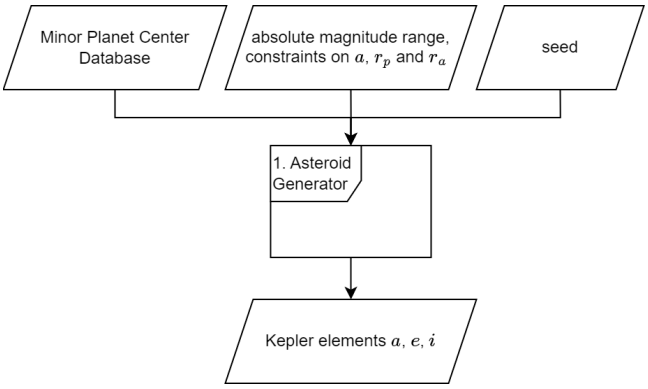

Figure 2.12: The asteroid is generated based on the Minor Planet Center catalog, the position of the Earth at the projected asteroid impact and the size. The asteroid catalog is filtered by absolute magnitude and if it is Earth crossing.

The asteroid generator determines only the a, e, i elements of the asteroid orbit. They constrain the ”shape” of the orbit, while the right ascension of the ascending node Ω, the argument of periapsis ω and the mean anomaly M determine the orientation and position of the asteroid along the trajectory. The remaining three elements are the result of constraining the asteroid orbit such that it impacts Earth within a specified warning time. The next block, the asteroid orbit generator, takes the a, e, i and the orbital position of Earth at the projected time of impact, as shown in Figure 2.13.

Information about the position of celestial elements, in this case the position of the Earth at a certain point in time, is taken from the Jet Propulsion Laboratory (JPL) ephemerides service, which is accessed via the Pykep package [28]. Pykep is an ESA developed suite of functions for astrodynamics. The target selection is further detailed in Section 4.1.

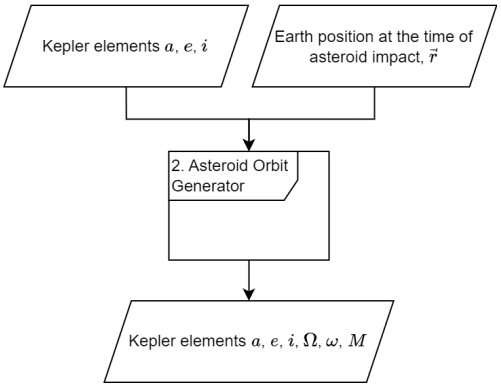

Figure 2.13: The asteroid orbit generator returns the complete set of Kepler elements for a representative target that is on an interception trajectory with Earth at a certain time in the future.

Transfer trajectory

With the orbit of the asteroid fully determined, the transfer trajectory can be calculated. The position and orbital velocity of Earth at the start date, $\vec{r}_E$ and $\vec{v}_E$, as well as the position and orbital velocity of

the asteroid at the start date plus the time of flight, $\vec{r}_A$ and $\vec{v}_A$ are required for a targeting algorithm. The module called ”Position and Velocity Converter” takes the Keplerian elements of the asteroid and converts it into the radial position and velocity. For Earth, the Pykep functionality is used to determine the position and velocity at the required epoch. The module and the inputs and outputs is shown in Figure 2.14.

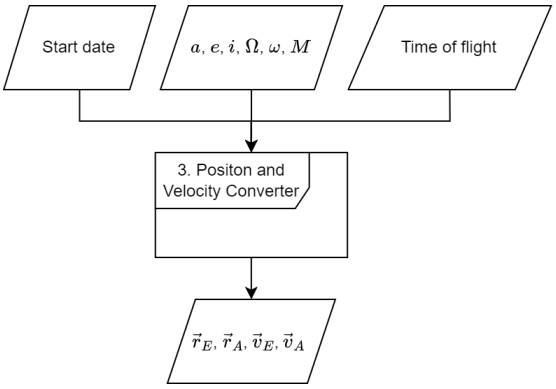

Figure 2.14: To find a transfer trajectory, the position and velocity of the start and end bodies has to be determined, based on the Kepler elements of the asteroid orbit, the start date and the time of flight.

The next step is to calculate the transfer trajectory from $\vec{r}_E$ to $\vec{r}_A$ within the time of flight TOF. This is congruent with the formulation of Lambert’s problem, and the solution is detailed in Section 5.1. The Pykep library includes a verified Lambert targeter and is used for the remainder of the thesis. The Lambert targeter can solve for an elliptic transfer trajectory, and return the velocity at the start and end point, designated by $\vec{v}_1$ and $\vec{v}_2$ and visualized in Figure 2.15. The Lambert targeter calculates a ballistic trajectory without any thrusting maneuvers.

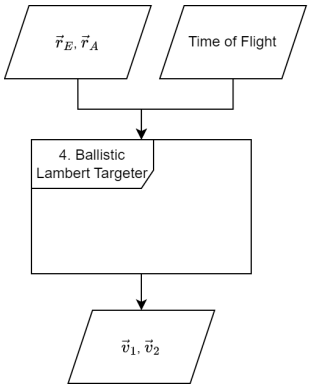

Figure 2.15: The ballistic lambert targeter requires the position of start and end of the trajectory and the time of fligt. As a result it returns the velocity vectors.

Launch vehicle

The next steps towards calculating the figure of merit is to determine the velocity change required to bring the spacecraft on the interplanetary transfer trajectory. Depending on the commissioning option, characterized by the height of the parking orbit h_{park} and the height of the perigee and apogee, h_a and h_p of a GTO, the $\Delta V_{departure}$ required for the planetary departure is calculated. The details of the planetary departure can be found in Section 5.3. For a direct interplanetary insertion, the characteristic energy is calculated from the orbital velocity of Earth v_E, and the required velocity for the transfer trajectory v_1. As a result, the ”velocity calculator” returns the C_3 or $\Delta V_{departure}$ required to determine how much mass can be brought to the asteroid, as shown in Figure 2.16.

The second result is the impact velocity of the kinetic impactor on the asteroid. The impact velocity is the vector difference of the orbital velocity of the asteroid $\vec{v}_A$ and the end velocity of the Lambert

targeter $\vec{v}_2$.

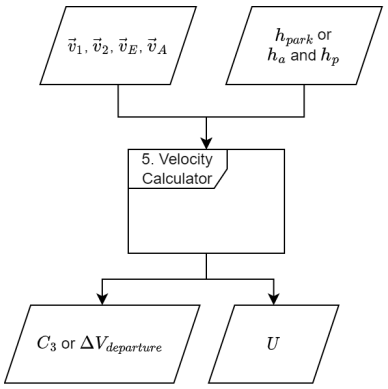

Figure 2.16: The module calculates the impact speed and the velocity change required for planetary departure. For direct interplanetary insertion, C_3 is used as a key figure. For departure from a parking orbit, the $\Delta V_{departure}$ is used.

Impact mass

The next step is to find the available launch mass, to eventually estimate the impact mass of the spacecraft on the asteroid. For the direct planetary insertion, the required C_3 is directly related to the payload mass and the curves in Figure 2.6 are used. The selected launch vehicles have different capabilities to GTO and LEO, and the values given in their respective user's manual are referred to find the launch mass. An overview of the inputs and outputs of the "launch vehicle" module is given in Figure 2.17.

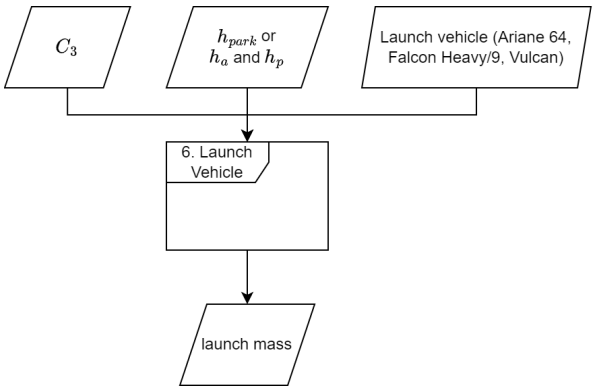

Figure 2.17: The launch vehicle module provides the launch mass depending on the required characteristic energy or the type of parking orbit.

To finally get the impact mass, the next module is estimating the performance of the propulsion system for planetary departure. The $\Delta V_{departure}$ is an input as well as the specific impulse of the bi-liquid or solid propellant system. With the well-known Tsiolkovsky rocket equation, the fuel mass for the maneuver is calculated and hence the impact mass is known. For the solid rocket motors, it is assumed that the available propellant is completely used. Furthermore, no gravity losses are taken into account and the maneuver is assumed to be an impulsive shot. For the direct interplanetary insertion, the impact mass is directly taken from the launch mass of the vehicle as a function of C_3.

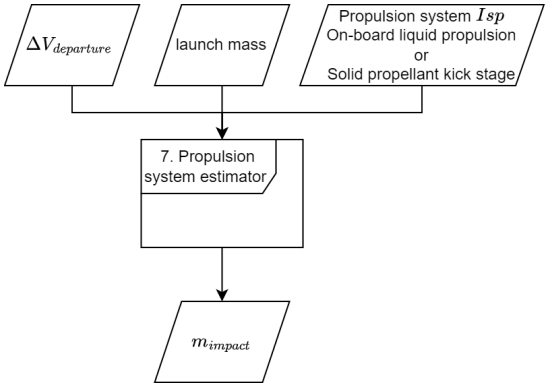

Figure 2.18: The propulsion system module return the mass that is available for impact after calculating the propellant mass required after the planetary departure maneuver.

Low-thrust transfer

In addition to the ballistic elliptical transfer, a low-thrust trajectory is estimated. A shape-based method with exponential sinusoids is implemented. The propulsion system and launcher specification are integrated into a single model, which is standalone from the previously presented modules. Along the trajectory, the ΔV and fuel consumption is calculated. The module returns the impact mass and impact speed, which is required for the figure of merit J as obvious in Equation (2.1). Further inputs are required for this module, including the launch vehicle, the allowed number of revolutions and the winding parameter k_2 of the exponential sinusoid. A detailed description of the module is given in Section 5.2. The module is shown in Figure 2.19.

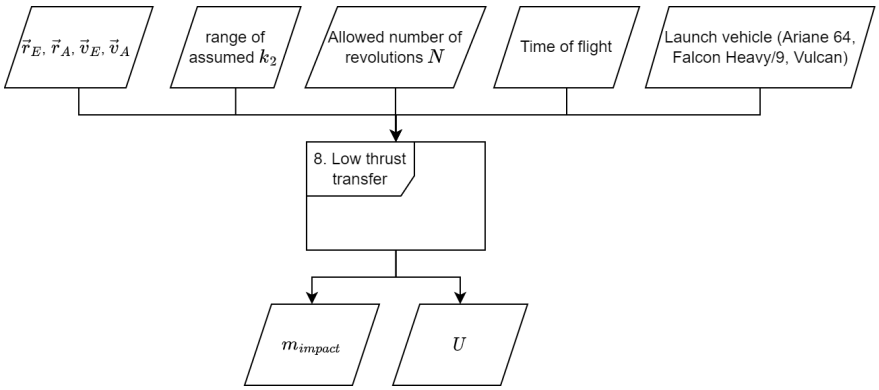

Figure 2.19: The low thrust transfer model includes the planetary departure and directly returns the impact mass and impact speed. It requires more inputs than the ballistic lambert targeter, such as the launch vehicle, the allowed number of revolutions and the winding parameter k_2.

β and the figure of merit J

The next step is to determine the impact efficiency parameter β with the method outlined in Chapter 3. The implemented scaling laws, responsible for estimating the impact efficiency, take the mass and speed as an input as well as the asteroid parameters. The β-factor is an important result, because it has a direct linear relation with the velocity change given to the asteroid, as obvious from the Equation (2.1) for J. The module is visualized in Figure 2.20.

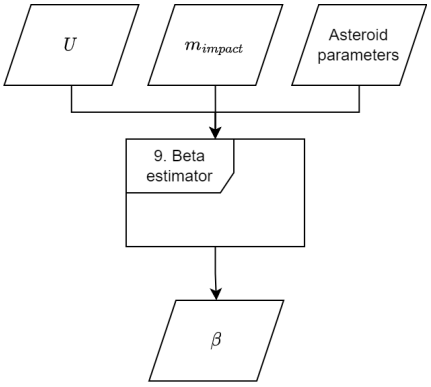

Figure 2.20: The impact module takes the impact mass and speed as an input and returns the β-factor. The asteroid parameters are also an input.

The last step is to calculate the performance parameter J. The input for that is the previously determined impact mass and speed. Combined with the asteroid mass M and the impact efficiency β, the module in Figure 2.21 returns the performance indicator.

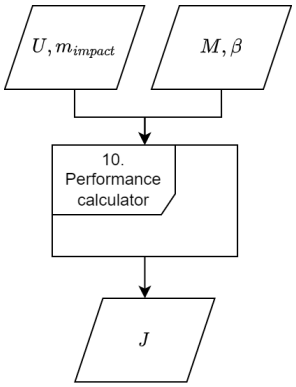

Figure 2.21: The module return the figure of merit, which indicates the velocity change of the asteroid caused by the kinetic impactor.

3

Impact modelling

The impact modelling is concerned with estimating the momentum enhancement (Section 3.1) by implementing suitable scaling laws (Section 3.2). Important steps are estimating the ejecta velocity (Section 3.3) and the ejecta mass (Section 3.4). The last step is determining the ejection angle Section 3.5, before calculating the ejecta momentum Section 3.6. A method to deal with an oblique impact angle is treated in Section 3.7. Finally, the sensitivity of the β-estimation is discussed in Section 3.8, the convergence of the method is checked in Section 3.9 and the method is verified and validated in Section 3.10.

3.1. Momentum enhancement

During the impact and crater formation, material is launched away from the impact site. The ejecta carries momentum and can enhance the momentum change of the asteroid significantly when it leaves the asteroid system with escape velocity. The β-factor is described by Holsapple and Housen [24] as the following:

> The change in the momentum of the asteroid is the sum of the momentum of the impactor and the momentum contained in the material permanently ejected backwards from the impact site. The amount of material ejected is typically many times the mass of the impactor, and much of it may be permanently ejected with initial speeds in excess of the escape velocity. Consequently, the momentum transferred to the target asteroid (i.e. to its remaining mass) can be significantly greater than the momentum of the incoming spacecraft. The ratio of the momentum imparted to the asteroid to the momentum of the impactor is commonly called the ”momentum multiplication”, and is given the symbol β. Thus β is the measure that determines the deflection effectiveness of the impact.

In mathematical terms, assume the spacecraft has a relative velocity prior to the impact of $v_{sc,i}$ and a mass of m_{sc}. Then the β-factor is given in Equation (3.1), with M the remaining mass of the asteroid and Δv the velocity change of the asteroid due to the impact.

$$\beta = \frac{M\Delta v}{m_{sc}v_{sc,i}} \tag{3.1}$$

By applying the conservation of momentum to the case of the spacecraft striking the asteroid, the β-factor can be written as [9]

$$\beta = 1 + \frac{m_{ej}v_{ej}}{m_{sc}v_{sc,i}} = 1 + \frac{p_{ej}}{m_{sc}v_{sc,i}}. \tag{3.2}$$

As evident from Equation (3.2), the ejecta momentum is directly related to the β factor. In Figure 3.1 the situation before and after impact is sketched. The first row shows a hypothetical impact without ejecta, and a resulting β-factor of 1. An inelastic collision with ejecta includes additionally the ejecta momentum $m_{ej}v_{ej}$ and the β-factor is larger than one. The following sections outline how the velocity, mass,

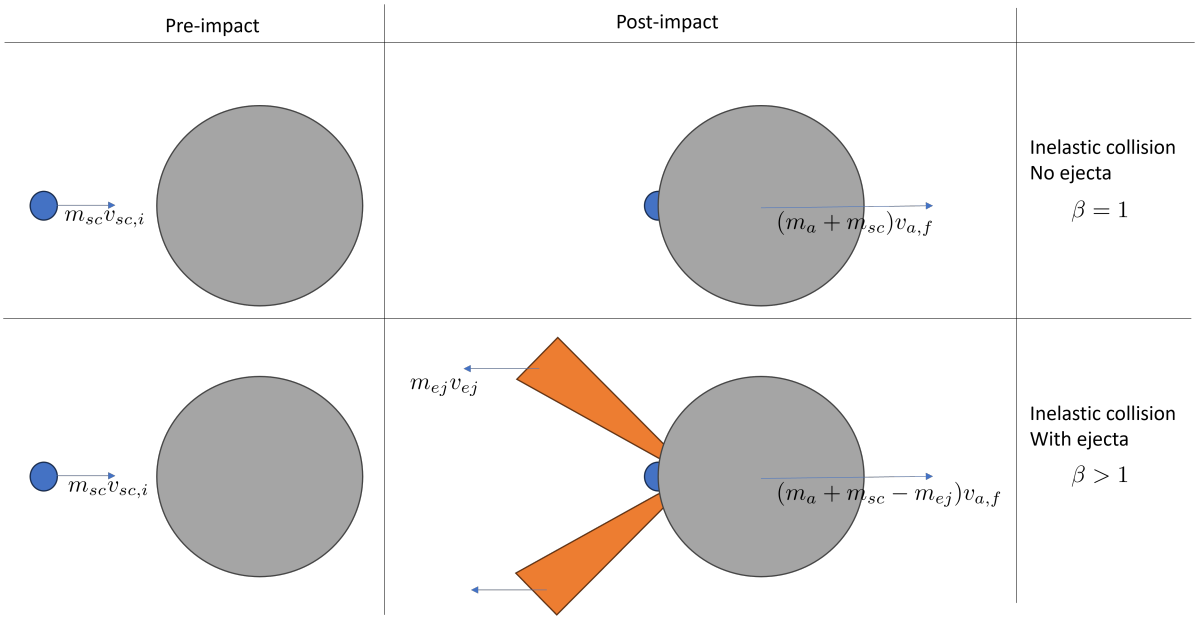

Figure 3.1: The impact efficiency factor β is larger than one when ejecta is accelerated in the opposite direction of impact. The momentum of the spacecraft, the ejecta and the asteroid are indicated.

ejection angle and eventually the momentum can be determined from scaling laws for hypervelocity impacts.

3.2. Scaling laws

The objective of scaling laws is to extrapolate the impact properties from small-scale experiments to larger impacts. A well adopted method are the scaling laws developed by Holsapple and Housen [27].

The scaling laws are based on the assumption that the impact of the projectile can be approximated by a point-source. During a hypervelocity impact, the cratering process occurs on large time and distance scales compared to the impactor. Therefore, the impactor can be replaced by a point-source of equivalent energy. The relevant properties of the projectile are a characteristic dimension a, the impact speed U and the projectile mass density δ. These parameters are combined in a coupling parameter C, with a velocity scaling exponent and μ and density scaling exponent ν [26].

$$C \propto a U^{\mu} \delta^{\nu} \tag{3.3}$$

The characteristic dimension a of a spherical impactor is usually taken as the radius. The parameter μ and ν directly influence the results of the scaling laws and are obtained from impact experiments or numerical simulations.

3.3. Ejecta velocity

The ejecta velocity, normalized by the impact speed and therefore represented by $\frac{v}{U}$, is a function of radial distance from the impact point and is represented by a power function. Depending on the regime of the impact, different forms of the velocity distribution have been proposed. For large impacts, the crater formation is dominated by the gravity of the target body, and the velocity is described by Equation (3.4). When the target has a large cohesive strength compared to the lithostatic pressure at the crater depth, the cratering process is said to be in the strength regime and the velocity distribution is calculated with Equation (3.5). Raducan et. al. [42] suggest a further modification to the velocity distribution for the fast-moving ejecta close to the impact point, see Equation (3.6).

$$\frac{v}{U} = C_1 \left(\frac{r}{a} \left(\frac{\rho}{\delta} \right) \right)^{-1/\mu} \text{ (gravity)} \tag{3.4}$$

$$\frac{v}{U} = C_1 \left(\frac{r}{a}\left(\frac{\rho}{\delta}\right)\right)^{-1/\mu} \left(1 - \frac{r}{n_2 R}\right)^{p} \text{ (strength)} \tag{3.5}$$

$$\frac{v}{U} = C_1 \left(\frac{r}{a}\left(\frac{\rho}{\delta}\right)\right)^{-1/\mu} \left(1 - \frac{r}{n_2 R}\right)^{p} \left(1 - \frac{a}{n_1 r}\right)^{q} \tag{3.6}$$

The ratio to decide between strength regime and gravity regime is given in Equation (3.7), with density ρ, surface gravity g, crater radius R and target strength Y. If the ratio is larger than unity, the cratering process is said to be in the gravity regime.

$$\frac{\rho g R}{Y} \tag{3.7}$$

The crater radius is determined, depending on the regime of the impact. Holsapple and Schmidt derived these equations from the point source assumption [26].

$$R\left(\frac{\rho}{m}\right)^{1/3} = H_2 \left(\frac{Y}{\rho U^2}\right)^{-\mu/2} \left(\frac{\rho}{\delta}\right)^{(1-3v)/3} \text{ (strength)} \tag{3.8}$$

$$R\left(\frac{\rho}{m}\right)^{1/3} = H_1 \left(\frac{ga}{U^2}\right)^{-\frac{\mu}{2+\mu}} \left(\frac{\rho}{\delta}\right)^{\frac{2+\mu-6\nu}{3(2+\mu)}} \text{ (gravity)} \tag{3.9}$$

The velocity distribution is a power function and usually visualized in a plot with two logarithmic axes. The parameters of the curve are shown on the left of Figure 3.2. The curve is a function of distance r, with $r = 0$ being equivalent to the impact point. The distance r is non-dimensionalized with the impactor dimension a. The fraction $\frac{r}{a}$ is often referred to as w and is the parameter on the x-axis of the graph on the right of Figure 3.2. The ejecta velocity decreases with growing distance from the impact point. Close to the impact point, the shape of the curve for the fast-moving ejecta are modified with the q-parameter at a distance $r = n_1 a$. A similar modification to the function is done for the slower ejecta at $r = n_2 R$, with R being the crater radius. The parameter p is used to flatten the curve to better represent the velocity cut-off at larger distances from the impact.

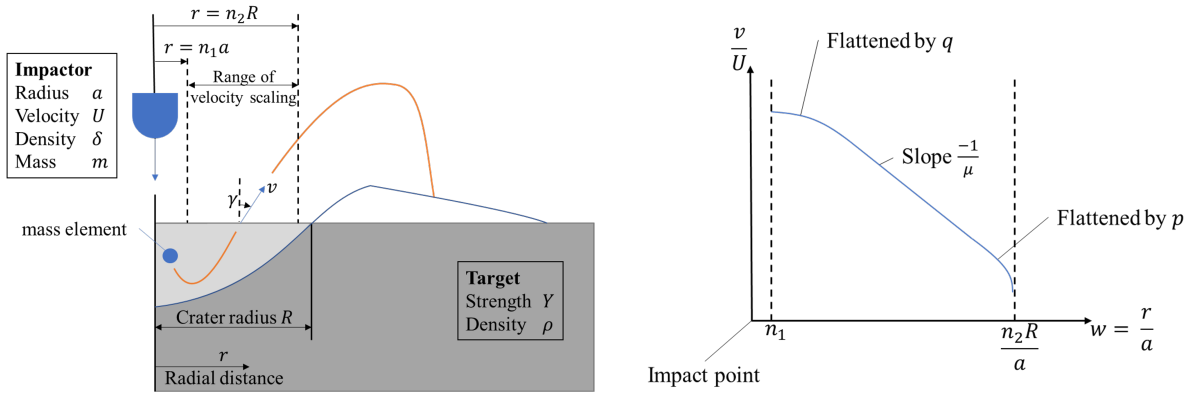

Figure 3.2: The definition of parameters for the impact. The figure on the left is adapted from [27]. On the right, the velocity distribution is shown as a function of w.

C_1 and μ further dictate the shape of the velocity distribution. The C_1 parameter is the y-intercept of the curve. μ is the velocity scaling exponent and modifies the slope of the power function. The density of the impactor δ and the density of the target material ρ

The general shape of the velocity distribution is deduced from impact experiments or numerical simulations. Then the curve described by Equation (3.6) is fitted to match the measured velocity and the non-dimensionalized parameters C_1, μ, p and q are determined.

3.4. Ejecta mass

As derived by Housen [27], the mass of debris ejected within a certain distance r can be expressed by the following equation with mass scaling constant k.

$$M = k\rho r^3. \tag{3.10}$$

Very close to the impact point, in direct vicinity to the projectile, the material is driven downward instead of being ejected. Therefore, a mass cut-off at a distance $r = n_1 a$ is implemented. Furthermore, the equation is adjusted such that it is a function of the normalized distance $\frac{r}{a}$.

$$M = k\rho \left[r^3 - (n_1 a)^3 \right] \tag{3.11}$$

The ejected mass is normalized with the mass of the impactor. For example, a spherical impactor with a mass of $m = \frac{4}{3}\pi a^3 \delta$ results in

$$\frac{M}{m} = \frac{3k}{4\pi} \frac{\rho}{\delta} \left[\left(\frac{r}{a} \right)^3 - n_1^3 \right]. \tag{3.12}$$

3.5. Ejection angle

In order to calculate the ejecta momentum, the direction and velocity of the mass particles has to be determined. Only the particles that have sufficient velocity to leave the gravitational well of the NEO contribute to the momentum enhancement with their vertical velocity component. The method to determine the velocity v_∞ and direction of the debris θ_∞ is described in the following.

It is assumed that a mass particle is launched from the impact site with a certain velocity v and the ejection angle γ with respect to the vertical. The asteroid is assumed to be spherical with radius r and the local vertical defined as the line through the center of the asteroid and the impact point. Furthermore, it is assumed that the debris particles do not interact with each other and follow a ballistic trajectory. The situation is sketched in Figure 3.3

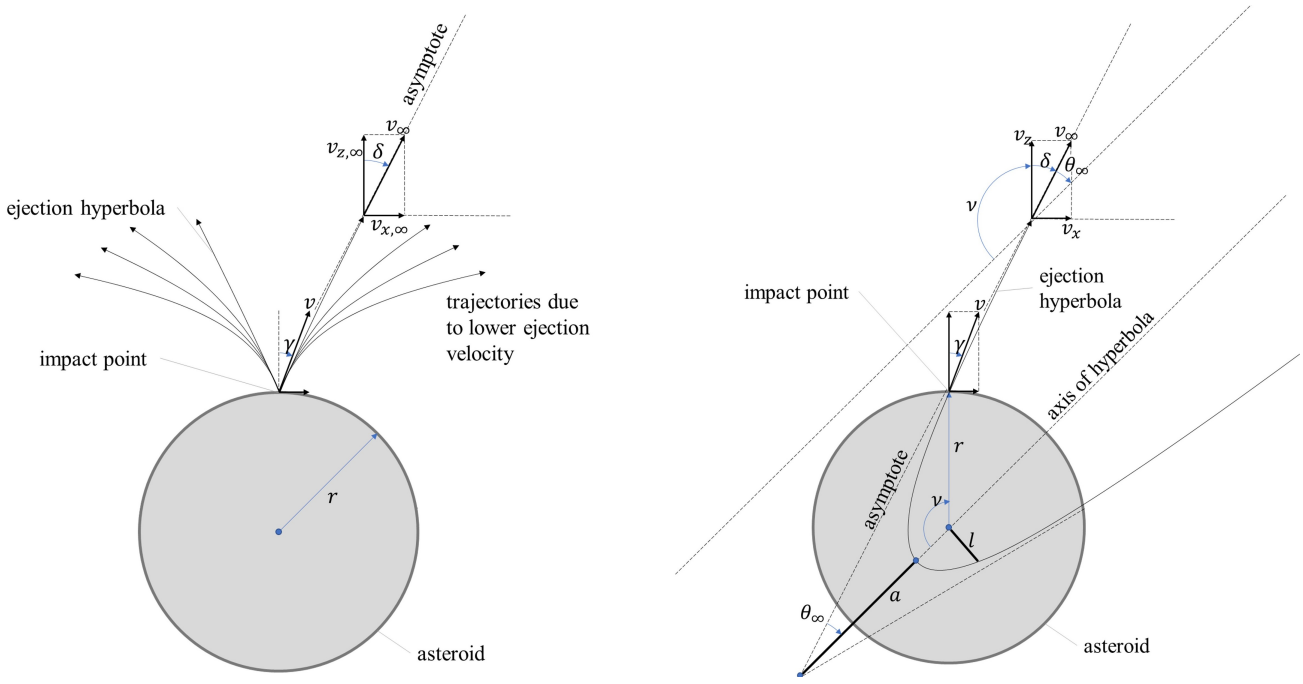

Figure 3.3: The ejection of particles at different velocities generates multiple ejection trajectories. On the right, an ejection hyperbola is sketched for a single particle and the parameters used in the calculation of the hyperbolic excess velocity and the angle θ_∞.

With those assumptions, the angular momentum of the 2D Keplerian trajectory of the particles can be computed by

$$h = rv \sin \gamma. \tag{3.13}$$

Starting from the vis-viva equation, the semi-major axis can be calculated as

$$a = \left(\frac{2}{r} - \frac{v^2}{\mu} \right)^{-1}. \tag{3.14}$$

Combining the angular momentum and the gravitational parameter of the NEO gives the semi-latus rectum of the trajectory.

$$l = \frac{h^2}{\mu} \tag{3.15}$$

With the semi-major axis and the semi-latus rectum known, the eccentricity of the conic section can be calculated. If the eccentricity is larger than one, the trajectory is hyperbolic and the particles escape the NEO.

$$e = \sqrt{\frac{l}{a} + 1} \tag{3.16}$$

Starting from the orbit equation, the true anomaly can be calculated from the semi-latus rectum and the eccentricity.

$$\begin{aligned} r &= \frac{l}{1 + e \cos \nu} \\ \Leftrightarrow \ \nu &= \arccos \left[\frac{1}{e} \left(\frac{l}{r} - 1 \right) \right] \end{aligned} \tag{3.17}$$

In order to get the angle δ, which is the angle between the local vertical and the hyperbolic excess velocity vector, the angle θ_∞ is required, which is the half-angle between the asymptotes of the hyperbola, and can be calculated by

$$\theta_\infty = \arccos \left[-\frac{1}{e} \right]. \tag{3.18}$$

Since the velocity asymptotically approaches v_∞, the angle θ_∞ is the angle between the velocity vector and the axis of the hyperbola. Combining it with the true anomaly leads to an expression for the desired angle δ.

$$\delta = \pi - (\theta_\infty + \nu) \tag{3.19}$$

The hyperbolic excess velocity is computed from the escape velocity v_e and the initial velocity v.

$$\begin{aligned} v_e &= \sqrt{\frac{2GM}{r}} \\ v_\infty &= \sqrt{v^2 - v_e^2} \end{aligned} \tag{3.20}$$

The ejecta momentum is calculated with the vertical velocity component $v_{z,\infty} = v_\infty \cdot \cos \delta$.

3.6. Ejecta momentum

The ejecta momentum can be deduced from the mass and velocity distribution. The momentum can be written as

$$p_{ej} = \int_m v_{z,\infty} dM. \tag{3.21}$$

For simplification, the distance from the impact point, normalized with the impactor dimensions, is given the symbol $w = \frac{r}{a}$. Starting from Equation (3.11), the mass distribution can be written as

$$M = k\rho a^3 \left(w^3 - n_1^3\right) \tag{3.22}$$

Finding the derivative with respect to w is straightforward.

$$dM = 3k\rho a^3 w^2 dw \tag{3.23}$$

Substituting Equation (3.23) into Equation (3.22) gives an integral over the normalized distance w. The velocity distribution is valid between the limits defined by n_1 and n_2, and is written as

$$p_{ej} = 3k\rho a^3 \int_{n_1}^{\frac{n_2 R}{a}} v_{z,\infty} w^2 dw \tag{3.24}$$

3.7. Oblique impact

In contrast to a perfectly vertical impact, an oblique impact generates a differently shaped ejecta cone. In reality, the impactor will strike the surface at an angle different from 90° to the surface, so it is necessary to account for the effects of an impact at an oblique angle. The impact angle can be influenced by the orbit control system of the spacecraft. For example, the impact angle of DART was around 73° [12]. An oblique impact has a lower momentum enhancement factor than a vertical impact. In the model proposed by Raducan et al. [40], the asymmetry of the ejecta curtain is accounted for by dividing the ejecta into a number of segments around the impact point. The segments are defined by their angle of azimuth with the incoming impactor direction. A simplifying assumption is that the ejecta cone is axisymmetric around the incident direction. A sketch of the segmentation approach is given in Figure 3.4

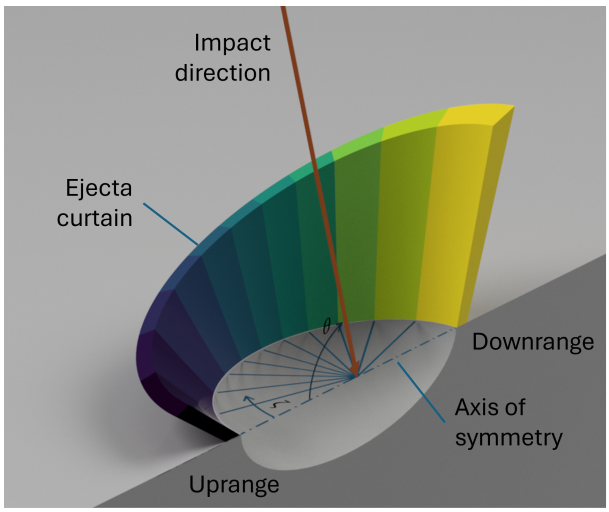

Figure 3.4: The ejecta curtain is discretized into a number of segments around the azimuth angle ζ. The curtain is assumed to be symmetric along the incident direction of the impactor, which strikes the surface at an angle θ with the horizontal.

For each azimuthal segment, the properties of the impact are calculated, in this case the ejecta momentum, and then summed over the number of segments. To calculate the ejecta momentum, Equation (3.24) is adjusted to include the summation of the azimuthal segments, with n_ζ being the number

of segments. The symmetry of the ejecta cone is utilized such that the sum is taken over one half of the ejecta cone and then doubled. Furthermore, according to the method by Raducan et. al [40], the scaling constants are defined as functions of the azimuth angle ζ and the impact angle θ, specifically $\mu(\zeta,\theta)$, $k(\zeta,\theta)$, $C_1(\zeta,\theta)$ and $R(\zeta,\theta)$. With the simulation results of Raducan et. al. [40], the velocity distribution is determined for each segment and the curve is fitted to Equation (3.6) to determine $\mu(\zeta,\theta)$ and $C_1(\zeta,\theta)$.

It is observed that the ejection velocity close to the downrange direction is lower than in the uprange direction. The $C_1(\zeta,\theta)$ is therefore increasing with increasing azimuth. The slope of the velocity distribution gets steeper with increasing angle, so the $\mu(\zeta,\theta)$-function is decreasing as it approaches the uprange region.

A similar procedure is applied to the mass distribution. Equation (3.12) is fitted to results of the impact simulation to get a function for $k(\zeta,\theta)$. The ejected mass is higher in the downrange direction, so the function of k is increasing.

The crater radius is also determined from the simulation and a function for $R(\zeta,\theta)$ is determined. As the impact becomes more oblique, the crater resembles a more and more elliptical shape. The functions for the scaling constants and the crater radius are given in Equation (3.25) It is preferred to use periodic functions, since the crater properties shall be continuous around the azimuth. Also, the functions are defined in terms of the values of the constants for the vertical impact scenario, such that any set of constants can be adjusted for an oblique impact.

$$\begin{aligned}
\mu(\zeta,\theta) &\approx \mu \cdot \left[1 + \frac{1}{2}\cos(\zeta)\cos(\theta)\right] \\
C_1(\zeta,\theta) &\approx C_1 \cdot \exp\left[-5\cos(\zeta)\cos(\theta)\right] \\
k(\zeta,\theta) &\approx \frac{k}{n_\zeta} \cdot \exp[-0.02\cos(\zeta)\cos(\theta)] \\
R(\zeta,\theta) &\approx R \cdot \left[1 - \frac{(90-\theta)}{2}\cos\zeta\right]
\end{aligned} \tag{3.25}$$

The velocity distribution in Equation (3.6) is adjusted to include the oblique impact effect.

$$\frac{v(\zeta,\theta)}{U} = C_1(\zeta,\theta)\left(\frac{r}{a}\left(\frac{\rho}{\delta}\right)\right)^{-1/\mu(\zeta,\theta)}\left(1-\frac{r}{n_2 R}\right)^p\left(1-\frac{a}{n_1 r}\right)^q \tag{3.26}$$

With the process described in Section 3.5, the excess velocity $v_{z,\infty}(\zeta,\theta)$ of the mass particles is determined for every segment and then inserted into the equation for the ejecta momentum.

$$p_{ej} = 2\sum_{i=1}^{n_\zeta} 3k(\zeta,\theta)\rho a^3 \int_{n_1}^{\frac{n_2 R}{a}} v_{z,\infty}(\zeta,\theta) w^2 dw \tag{3.27}$$

The last step is to calculate the momentum enhancement with Equation (3.2).

3.8. Sensitivity

The scaling law method includes several parameters. In order to gain insight into how they affect the solution for β a sensitivity study was performed. The parameters are divided into two categories. The first category contains the parameters related to the scaling laws themselves. The parameters are either fitting constants or adjust the model to better represent the numerical simulations or experiments. They are listed in Table 3.1. The second category are the physical constants related to the impact, such as mass and speed of the impactor. They represent the actual properties of the target and the projectile and are summarized in Table 3.2. The division in two categories is also used for the sensitivity study.

To check the sensitivity of β to each of the parameters, the value of each of them is varied by 5% and 10%. Using two percentage values allows to judge if the relation is linear. The parameters are changed in the positive and negative direction. The results are shown in Figure 3.5 and Figure 3.6.

Table 3.1: The scaling constants used in the scaling laws.

Name	Symbol	Explanation	Sensitivity
Velocity scaling constant.	C_1	A material fitting constant to adjust the velocity distribution of the ejected material.	Linear scaling, so the change is one to one.
Velocity scaling exponent.	μ	A material fitting constant to adjust the slope of the velocity distribution.	Larger than one to one
Mass scaling constant.	k	A material fitting constant to adjust the mass distribution of the ejected material.	Linear scaling, so the change is one to one.
Lower ejecta velocity cut-off.	n_1	No material is ejected very close to the impact point and n_1 sets the lower limit.	Lower than one to one.
Upper ejecta velocity cut-off.	n_2	No material is ejected far away from the impact point and n_2 sets the upper limit.	Lower than one to one.
Density scaling exponent.	ν	Density scaling exponent.	Close to one to one.
Crater radius scaling constant in the gravity regime.	H_1	Material fitting constant for the crater radius.	Not used in this case.
Crater radius scaling constant in the strength regime.	H_2	Material fitting constant for the crater radius.	Close to one to one.
Low-speed ejecta constant.	p	Adjust the velocity distribution to have a gradual decrease in ejection velocity close to the crater rim.	Lower than one to one.
High-speed ejecta constant.	q	Adjust the velocity distribution to have a slight curvature close to the impact point.	Lower than one to one.

Table 3.2: The physical parameters used in the scaling laws.

Name	Symbol	Unit	Explanation	Sensitivity
Impactor radius.	a	m	The radius of a spherical impactor.	Close to one to one.
Target density.	ρ	kg/m^3	The density of the target material.	Lower than one to one.
Impactor density.	δ	kg/m^3	The density of the impactor.	Lower than one to one.
Impact speed.	U	m/s		Lower than one to one.
Impactor mass.	m	kg		Lower than one to one.
Target porosity.	Φ	%	Not used.	
Target strength.	Y	Pa	The cohesive strength of the target material.	Lower than one to one.
Target radius.	r	m	Radius of the asteroid	Lower than one to one.
Impact angle.	θ	deg	90 degrees is a vertical impact.	Lower than one to one.
Ejection angle.	γ	deg	Angle of the ejecta curtain with the vertical. 0 degrees is a perfectly vertical ejection.	Close to one to one

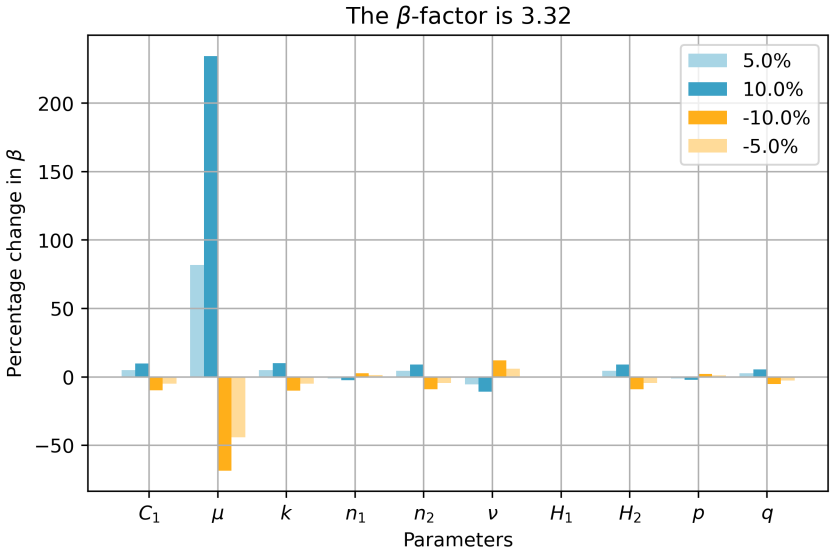

Figure 3.5: The sensitivity of the momentum enhancement β to a change in the scaling law constants.

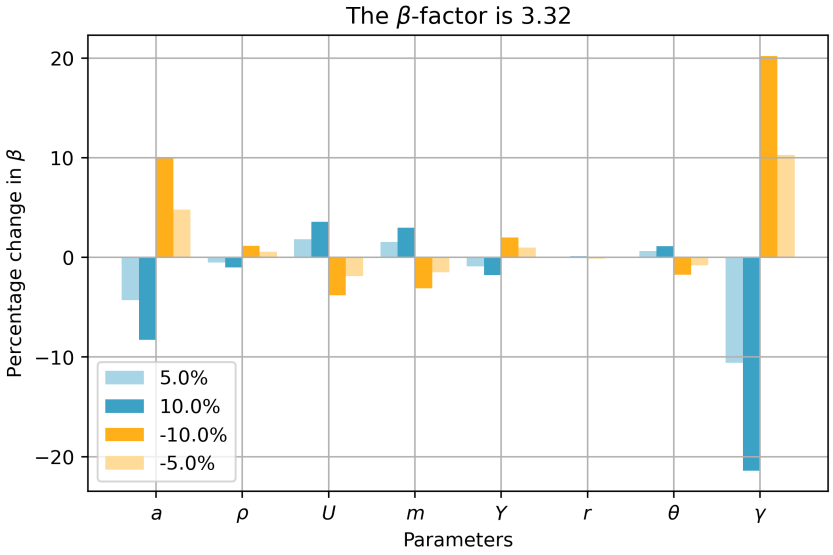

Figure 3.6: The sensitivity of the momentum enhancement β to a change in the physical impact parameters. Note the difference in x-axis scaling compared to Figure 3.5

The largest changes are observed for the scaling parameters. When the parameters are varied in isolation, the largest difference makes the velocity scaling exponent μ. According to the point-source assumption for the impact scaling laws, as conceived by Holsapple [26], the factor has a theoretical range between 1/3 and 2/3. The practical effect of varying the velocity scaling exponent is changing the slope of the velocity distribution. An increase in μ causes a larger β.

For the physical impact parameters, the impactor radius a and the target strength Y give the largest change. The impactor size is negatively correlated to β. So if the impactor gets larger but every other property stays the same, the momentum enhancement is reduced. The same correlation is observed in the target strength. The target strength plays a role in the crater formation. A weaker material allows for a larger crater and more excavated material, and therefore a larger momentum enhancement.

The target porosity Φ is a special case, because it does not directly appear in the scaling laws, but is an important factor in cratering dynamics. The porosity has an effect on the velocity distribution, and therefore on the constants C_1 and μ [42]. With the constants determined for different settings of porosity, the momentum enhancement can be calculated for the respective combination of C_1 and μ.

The result is shown in Figure 3.7. μ is continuously increasing for higher porosity and C_1 is decreasing. In the previous sensitivity study we found out that both parameters have an amplifying effect on β, so when they are increased separately, also β increases. Now, when going from 10% to 50% porosity, C_1 decreases by 74%, so the effect of decreasing C_1 is stronger than μ, which is only increased by 10%. So it makes sense that the beta is overall decreasing, but not necessarily continuously. Note, that the relative change in β is in comparison to the 10% porosity case.

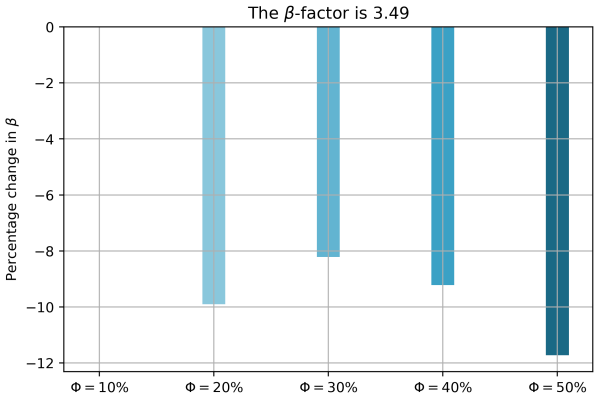

Figure 3.7: A change in porosity leads to a combined change in the C_1 and μ-factors. A general trend is a decrease in momentum enhancement for an increase in porosity.

3.9. Convergence

At two points in the method for determining β a discretization of the problem is occurring. First, the ejecta cone is separated into a number of segments, designated by n_ζ. Second, the velocity distribution is numerically integrated over the normalized distance from the impact point, given the symbol n_w. It is important to determine if and when the solution convergences for a certain size of n_ζ and n_w. The result of the convergence study is shown in Figure 3.8 for n_w and Figure 3.9 for n_ζ. Both properties converge reliably and the relative error between the current solution and the previous solution is recorded. An error of 10^{-3} is deemed acceptable and such $n_w = 800$ and $n_\zeta = 40$ are used for further calculations.

3.10. Verification and Validation

The implementation of the scaling laws are verified with the implementation by Raducan et. al. [40]. The first parameter that can be checked against the reported results is the crater size as a function of impact angle. The 3D numerical simulation performed by Raducan generate a crater, and the crater radius is an important parameter in the scaling laws. As shown in Figure 3.10, the calculated crater size with from Equation (3.25) is plotted over the simulated crater shape. The color gradient of the surface goes from dark blue, which indicates a depression, to brown, which indicates an elevation. The crater

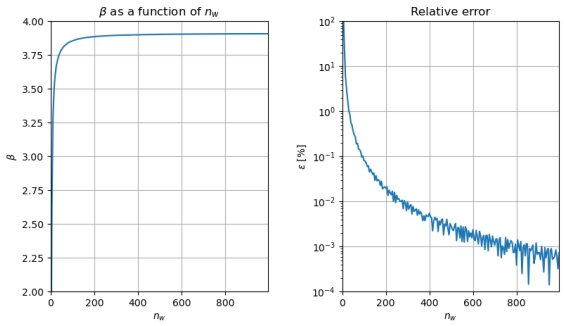

Figure 3.8: The convergence of the momentum enhancement with increasing number of evaluation points for the numerical integration of the velocity distribution and the relative error. Note the logarithmic x-axis in the error plot.

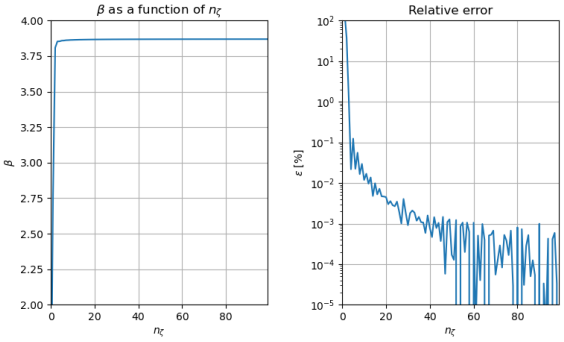

Figure 3.9: The convergence of momentum enhancement with increasing number of azimuthal segments and the relative error. Like in Figure 3.8, the error plot has a logarithmic x-axis.

rim is the white band that separates the depression from the elevation. The shape of the rim and the asymmetry around the y-axis is well represented.

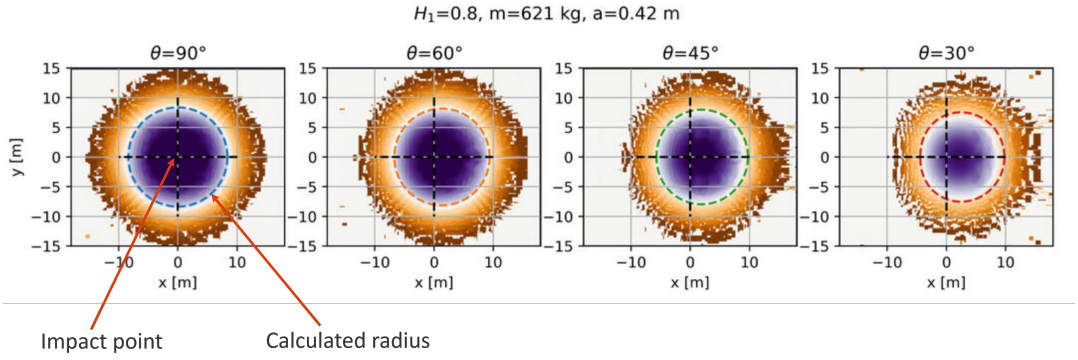

Figure 3.10: Top down view of the simulated crater shape by Raducan [40], with the recreated crater radius by the implemented scaling law. The impact point is at the center of the coordinate system and the calculated crater shape is a coloured dashed line.

A complete check is performed on the equations of the impact parameters around the azimuth in Equation (3.25) and compared to the simulation results. The results are shown in Figure 3.11

The last step is to validate the result of the scaling law with the available real life data point provided by the DART mission. The β-factor is reported to be $3.61^{+0.19}_{-0.25}(1\sigma)$ [8] and the impact angle is around 73° from the horizontal. The results for β as a function of impact angle is compared between the method by Cheng [9] and Raducan [40] in Figure 3.12. Both methods coincide in vertical 90° impact case, since they both rely on the same scaling laws. The method by Cheng assumes that for an oblique impact the ejecta curtain remains symmetric, and the impact speed is reduced to only the vertical component.

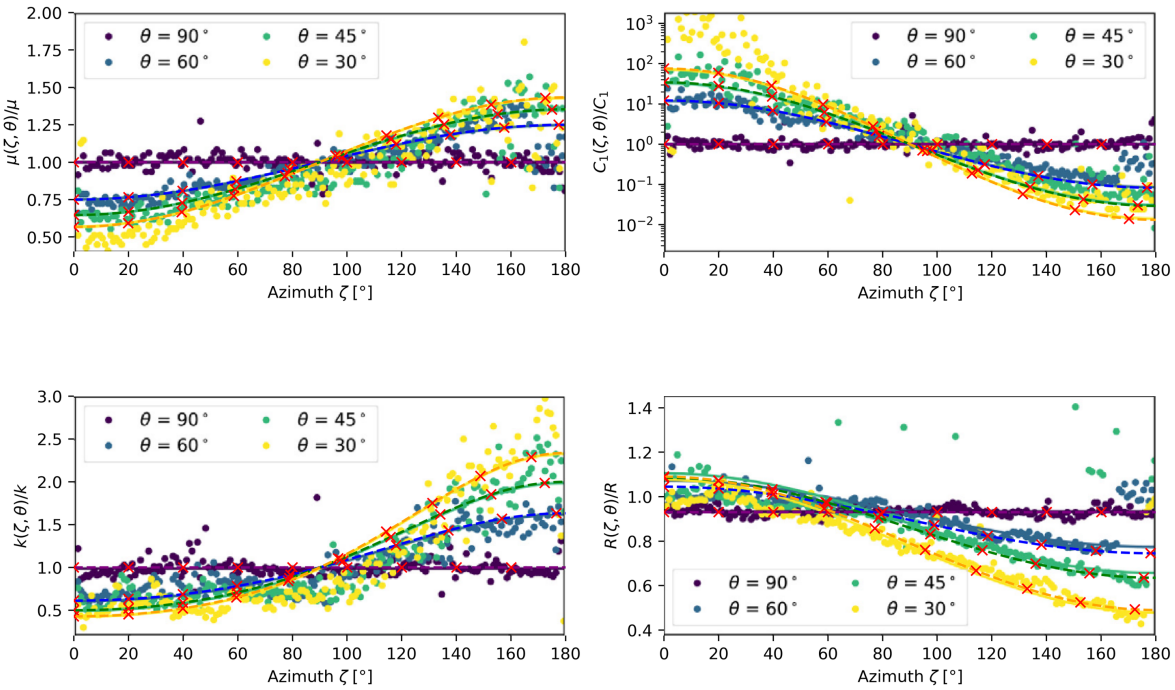

Figure 3.11: The impact parameters μ, C_1, k, and the crater radius R as a function of azimuth and impact angle. The scatter points are obtained from the simulation of Raducan et. al. [40] and the dashed lines, marked with red crosses for better visibility, are the functions used in the scaling laws.

The segmented approach by Raducan introduces the asymmetry around the incident direction of the impact and consistently predicts a lower β. The measured β for the DART impact is indicated, including the 1σ uncertainty. The scaling law prediction lies within the uncertainty and slightly underestimates the measured β. For the remainder of the thesis, the method by Raducan is employed to scale the impact properties to other impact geometries, speeds and impact mass.

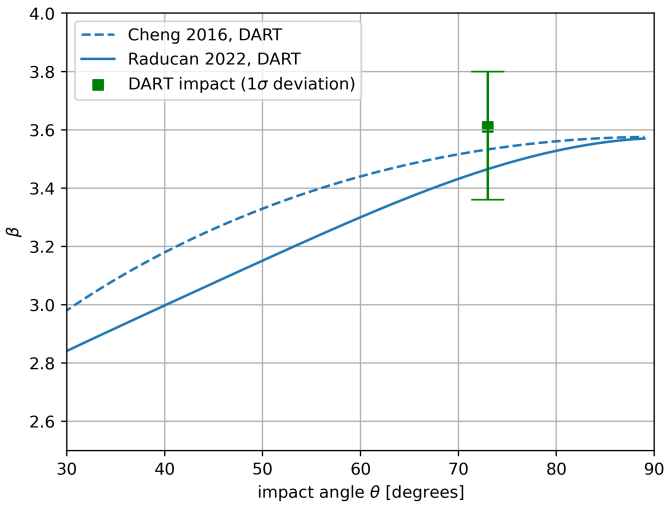

Figure 3.12: The predicted β-factor by the method of Cheng [9] and Raducan [40], compared to the measured β of the DART impact.

4

Asteroid

In this chapter, an asteroid target is selected for the kinetic impactor. The asteroid orbit is required to set up the transfer trajectory and determine the impact speed of the spacecraft on the asteroid. The method on how the target is selected is treated in Section 4.1. Dispersion thresholds are used to get an indication when the asteroid is at risk of breaking apart due to the impact, and the implemented limits are discussed in Section 4.2.

4.1. Target selection

A reference target has to be selected in order to plan and calculate a transfer trajectory to a representative asteroid. A few constraints are posed on the asteroid selection. First of all, the asteroid orbit shall comply with the conditions of an Earth-crossing NEO. For Apollo and Aten asteroids, the conditions are imposed on the semi-major axis a, the periapsis r_p and apoapsis r_a.

$$\begin{aligned} \text{Apollo} \quad & a > 1[AU] \ \wedge \ r_p < 1.017[AU] \\ \text{Aten} \quad & a < 1[AU] \ \wedge \ r_a > 0.983[AU] \end{aligned} \tag{4.1}$$

A further constraint is the asteroid size. In astronomy, the asteroid size can be inferred from its absolute magnitude H. The relationship between absolute magnitude H, diameter D and albedo α is given as [13]

$$H = -5 \cdot \log_{10} \left(\frac{D}{1.329 \cdot 10^6 \alpha^{-1/2}} \right). \tag{4.2}$$

With a range of albedos from 0.05 to 0.25, which is also used by the ESA Near-Earth Objects Coordination Centre [13] a range of absolute magnitudes for a certain diameter can be determined. The absolute magnitude as a function of diameter is shown in Figure 4.1. When assuming a diameter of 150m, which is roughly equivalent to Didymos, the target of the DART mission, a range of 23.0 to 21.2 for the absolute magnitude is determined.

To summarise, the asteroid target is constrained by the orbit type, either Apollo or Aten, and by a range of values for the absolute magnitudes. Applying these conditions to the asteroid catalog as provided by the IAU Minor Planet Center, the orbital elements for possible targets are filtered. The distribution of the semi-major axis, eccentricity and inclination is shown in Figure 4.2.

The orbital elements a, e and i are taken from the asteroid population, in order to get a representative orbit for a potentially hazardous asteroid. By constraining the orbit such that asteroid impacts earth at a certain time in the future, the remaining elements can be determined, which are the argument of periapsis ω, the right ascension of the ascending node Ω and the mean anomaly M. The Earth impact constraint means that at one point during the orbit the position vector is known, specifically $r = [r_1, r_2, r_3]$. The following steps are necessary to obtain the orbital elements ω, Ω, and M, from an asteroid with a certain a, e, and i, such that it impacts Earth at a certain position r. The objective is to get a population of asteroid orbits, that feature distinct orbit shapes, but share the property of posing an

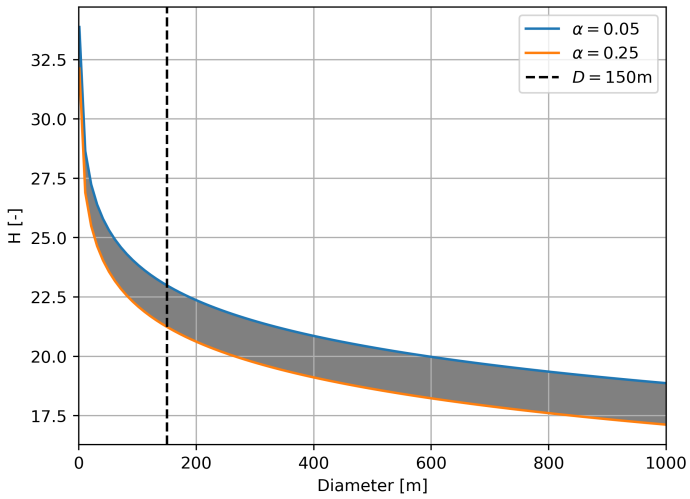

Figure 4.1: The absolute magnitude of an asteroid as a function of diameter. The shaded area indicates the result for a an albedo between 0.05 and 0.25.

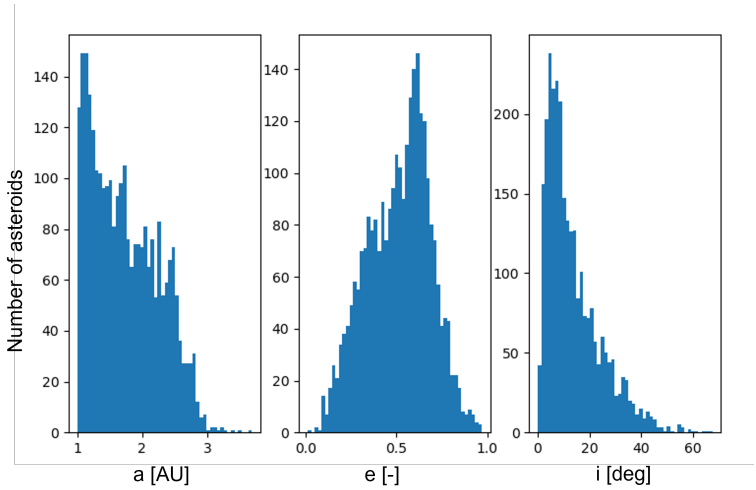

Figure 4.2: The distribution of semi-major axis, eccentricity and inclination for the asteroid population that fulfills the conditions for a suitable target asteroid.

actual threat to Earth. This asteroid population is used to generate the deflection performance results for the different spacecraft configurations.

First, the magnitude of the orbital angular momentum can be calculated with

$$h = \sqrt{\mu a(1-e^2)}. \tag{4.3}$$

The inclination of the orbit is given, so the momentum vector makes an angle i with the z-axis. The z-component of the h-vector can be determined with

$$\begin{aligned} \hat{K} \cdot \hat{h} &= |\hat{K}||\hat{h}| \cos i \\ \hat{h}_3 &= \cos i. \end{aligned} \tag{4.4}$$

The other two components of the h-vector are calculated from the constraints that $\hat{h} \perp \hat{r}$ and that $|\hat{h}| = 1$. The two respective equations are

$$\begin{aligned} 1 &= \hat{h}_1^2 + \hat{h}_1^3 + \hat{h}_3^2 \\ 0 &= \hat{h} \cdot \hat{r} = \hat{h}_1\hat{r}_1 + \hat{h}_2\hat{r}_2 + \hat{h}_3\hat{r}_3. \end{aligned} \tag{4.5}$$

An equation for $\hat{h}_2$ is set up.

$$\hat{h}_2 = -\frac{1}{\hat{r}_2}\left(\hat{h}_1\hat{r}_1 + \hat{h}_3\hat{r}_3\right) \tag{4.6}$$

By inserting the above equation into the constraint of orthogonality and performing some algebra, a quadratic equation for $\hat{h}_1$ is achieved.

$$\begin{aligned} a\hat{h}_1^2 + b\hat{h}_1 + c &= 0 \\ a &= \hat{r}_2^2 + \hat{r}_1^2 \\ b &= 2\hat{r}_1\hat{h}_3\hat{r}_3 \\ c &= \hat{h}_3^2\hat{r}_3^2 + \hat{r}_2^2\hat{h}_3^2 - \hat{r}_2^2 \end{aligned} \tag{4.7}$$

The quadratic equation is solved and the remaining two components of the momentum vector are determined.

$$\hat{h}_1 = \frac{-b \pm \sqrt{b^2 - 4ac}}{2a} \tag{4.8}$$

For a given angular momentum, inclination and position, there are two possible orientations of the orbital plane, as shown in Figure 4.3. Both of them are equally valid and can be used in further calculations.

The node line is at the intersection of the orbital plane and the reference plane, and is determined with

$$\vec{N} = \hat{K} \times \vec{h}. \tag{4.9}$$

Next, the right ascension of the ascending node Ω can be calculated.

$$\Omega = \begin{cases} \cos^{-1}\left(\frac{N_X}{N}\right) & N_Y \geqslant 0 \\ 2\pi - \cos^{-1}\left(\frac{N_X}{N}\right) & N_Y < 0 \end{cases} \tag{4.10}$$

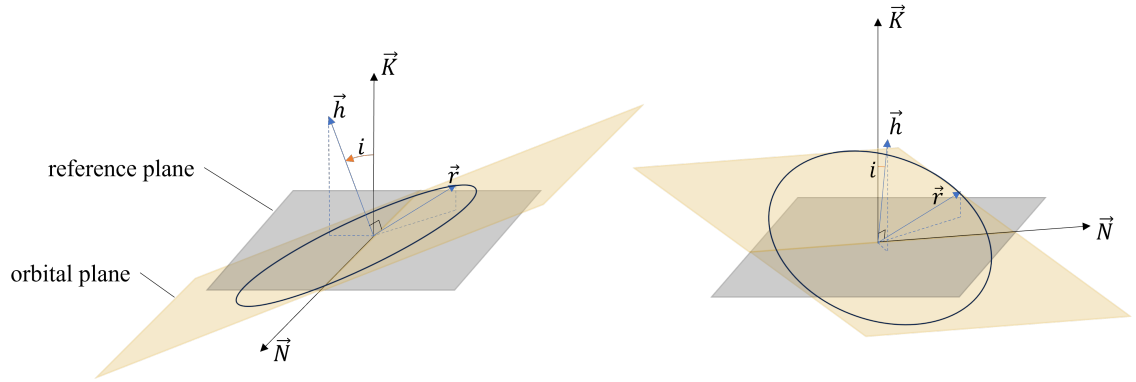

Figure 4.3: For a given angular momentum, inclination and position, there are two possible orientations of the orbital plane.

From the orbit equation, the true anomaly can be obtained. Due to the angle ambiguity of the inverse cosine, there are two solutions that satisfy the equation for a given position and eccentricity. This results in two possible orientations for the eccentricity vector. The first orientation is selected, which always creates an asteroid orbit that has a positive z-component of the eccentricity vector.

$$\begin{aligned} r &= \frac{h^2}{\mu}\frac{1}{1+e\cos\theta} \\ \theta &= \begin{cases} \arccos\left[\frac{1}{e}\left(\frac{h^2}{\mu r}-1\right)\right] \\ 2\pi - \arccos\left[\frac{1}{e}\left(\frac{h^2}{\mu r}-1\right)\right] \end{cases} \end{aligned} \tag{4.11}$$

The eccentricity vector is in the orbital plane. To get the direction of the eccentricity vector, the unit vector of the position is rotated clockwise by the true anomaly. For this, the Rodrigues' rotation formula is used [18].

$$\begin{aligned} \hat{e} &= \hat{r}\cos(-\theta) + (\hat{h}\times\hat{r})\sin(-\theta) + \hat{h}(\hat{h}\cdot\hat{r})(1-\cos(-\theta)) \\ \vec{e} &= e\cdot\hat{e} \end{aligned} \tag{4.12}$$

The argument of periapsis can then be determined.

$$\omega = \begin{cases} \cos^{-1}\left(\frac{\vec{e}\cdot\vec{N}}{eN}\right)) & e_Z \geqslant 0 \\ 2\pi - \cos^{-1}\left(\frac{\vec{e}\cdot\vec{N}}{eN}\right)) & e_Z < 0 \end{cases} \tag{4.13}$$

Next, the eccentric anomaly is calculated.

$$\begin{aligned} \tan\frac{E}{2} &= \sqrt{\frac{1-e}{1+e}}\tan\frac{\nu}{2} \\ E &= 2\arctan\left[\sqrt{\frac{1-e}{1+e}}\tan\frac{\nu}{2}\right] \end{aligned} \tag{4.14}$$

Finally, the mean anomaly, the last required orbital element, is obtained.

$$M = E - e\cdot\sin(E) \tag{4.15}$$

An example orbit is shown in Figure 4.4. With the process described in this section, the interception trajectory of a NEO with Earth, based on an existing set of a, e, i, is determined.

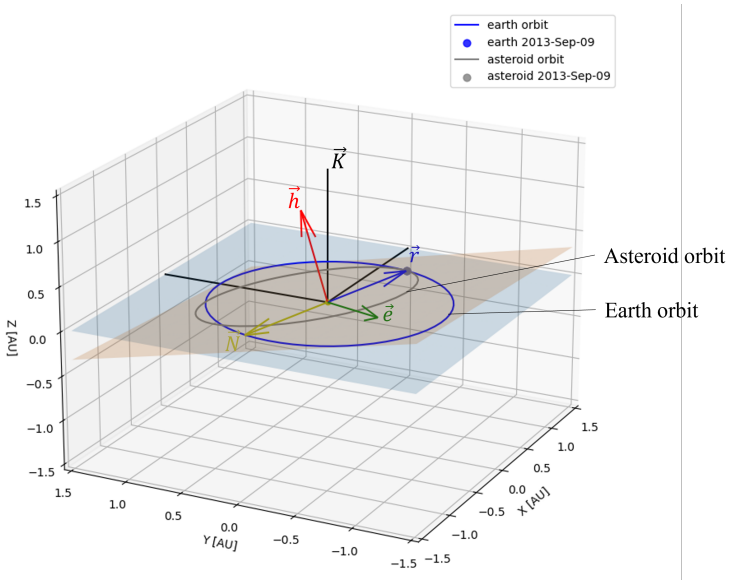

Figure 4.4: An example asteroid orbit, as determined from the asteroid population. Important vectors are the node line $\vec{N}$, eccentricity vectors $\vec{e}$, the angular momentum $\vec{h}$, and the position $\vec{r}$

.

4.2. Dispersion threshold

The momentum transfer between a projectile and the asteroid target is commonly treated under the assumption that the impactor is small, exerting minimal influence on the asteroid on a global scale. However, for smaller targets with low cohesion and weak self-gravity, there remains a possibility that a kinetic impactor could induce not cratering, but catastrophic disruption by displacing significant amounts of material. This phenomenon is quantified by the impact characteristic energy. The characteristic energy is the kinetic energy of the projectile normalized by the target mass.

Above a certain energy threshold, hypervelocity impacts can result in dispersal. Dispersal occurs when 50% of the material is displaced and permanently exits the asteroid. The respective energy threshold is denoted by Q_d*. The energy required for dispersal depends on asteroid size, density, strength, and projectile velocity.

Above the dispersal threshold for a given asteroid radius, these scaling laws are not applicable. Holsapple and Housen [25] provide an overview of dispersion thresholds as a function of radius and propose curves illustrated in Figure 4.5. The curves are generated for an example impact case at 5.5km/s and 45° impact angle as well as the impact conditions of the DART mission, with around 6.1km/s impact speed and an angle of 73°. The equations determined by Holsapple and Housen, with units J/kg and km, for a rocky S-type is

$$Q_d^* = 10^3 \cdot \left(\frac{R}{10^{-3}}\right)^{-0.33} + 10^6 \cdot \left(\frac{R}{500}\right)^{1.65} \tag{4.16}$$

and for a porous C-type is

$$Q_d^* = 2 \cdot 10^3 \cdot \left(\frac{R}{10^{-3}}\right)^{-0.25} + 4 \cdot 10 \cdot^5 \left(\frac{R}{500}\right)^{1.23} \tag{4.17}$$

In order to correct for the impact speed and angle the factors are added, for S-type and C-type respectively.

$$\left(\frac{U\cos\theta}{3.89}\right)^{0.35} \tag{4.18}$$

$$\left(\frac{U\cos\theta}{3.89}\right)^{0.6} \tag{4.19}$$

In the shape of the curves of Holsapple and Housen, two distinct regions can be discerned. For asteroids smaller than approximately 300 meters, the dispersion energy is primarily governed by rock strength. This is evident in the nearly linear decrease in dispersion energy, which correlates with the diminishing strength of rock as size increases. Larger rocks inherently contain more significant defects, such as cracks and voids, which lower the energy required for material failure compared to smaller objects. As long as asteroids fall within the size range where strength is a dominant factor, dispersion energy decreases with increasing size.

Conversely, asteroids larger than 300 meters experience an increase in dispersion energy due to their enhanced self-gravity. This gravitational force necessitates greater energy to disrupt the asteroid. The curves are based on estimates for monolithic rocky asteroids and porous targets resembling rubble piles. In the case of rubble piles, the compaction of porous material and its ability to reshape rather than fragment absorbs a significant portion of the impact energy. Consequently, within the strength-dominated regime, the energy required to disperse a loosely connected rubble pile is higher than that needed for a monolithic rock of comparable size. This relationship reverses for larger asteroids, where lower bulk density results in reduced self-gravity compared to rocky asteroids of similar dimensions.

An attempt at creating a dispersion curve for a zero-cohesion target was made by Raducan and Jutzi [41] and is shown Figure 4.5. For a cohesionless asteroid, the dispersion threshold increases with a larger diameter, since gravity force is the main force keeping the asteroid in its shape. Another useful threshold, the impact energy required to displace at least 20% of the asteroid material, is introduced as $Q_{reshape}$(20%).

The equation for the threshold by Raducan and Jutzi is

$$Q = a_g R^{3\mu_g} U^{2-3\mu_g} \tag{4.20}$$

with the factors a_g and μ_g determined by a numerical simulation of impacts into a cohesionless spherical target. For the dispersion threshold the factors are

$$\begin{aligned} &Q_d^* \\ &a_g = (1.0 \pm 0.2) \cdot 10^{-4} \\ &\mu_g = 0.39 \pm 0.01 \end{aligned} \tag{4.21}$$

and for the reshaping threshold they are

$$\begin{aligned} &Q_{reshape}(20\%) \\ &\qquad a_g = (1.8 \pm 0.5) \cdot 10^{-5} \\ &\qquad \mu_g = 0.38 \pm 0.02 \end{aligned} \tag{4.22}$$

In Figure 4.5, the impact condition of the DART spacecraft is added for reference. The impact energy was around 2.5 J/kg, and the radius of Dimorphos is around 75m. The line labelled ”DART impact conditions” assumes a constant density and a spherical target, and indicates at what point a DART-like impact could cause dispersion or reshaping. The DART impact is fairly close to the reshaping threshold.

Concerning the implementation of the threshold, the specific energy of the impact is calculated and the code prints a warning once one of them is breached. All cases of dispersion are taken into account and adjusted for impact speed and angle

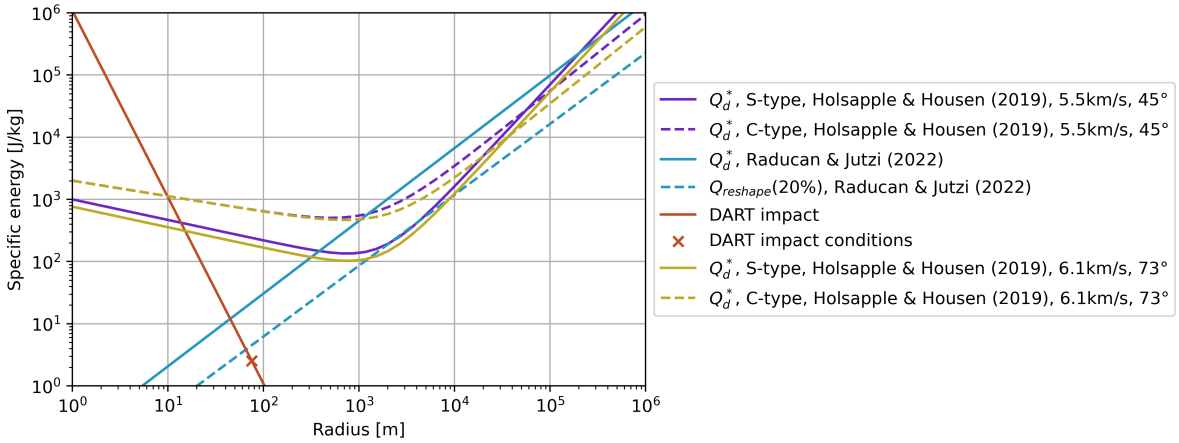

Figure 4.5: A compilation plot of the dispersion thresholds used in the implementation of the scaling laws. The thresholds are a function of specific impact energy and asteroid radius. Adapted from Raducan [39].

5

Methods

For the purpose of determining the deflection performance J, the departure from Earth, and the trajectory to the asteroid has to be analysed. Analytical methods are preferred in the preliminary design stage to keep the computational effort low, while still obtaining comparable results. A solution to Lambert's problem is used to find the required start and end velocity of the ballistic transfer trajectory, described in Section 5.1. An equivalent formulation of Lambert's problem is implemented for a low-thrust trajectory and detailed in Section 5.2. The planetary departure is modelled with the patched-conic approach, assuming an hyperbolic escape arc, connected to the elliptical or spiraling transfer trajectory. The departure is documented in Section 5.3. The geometry of the asteroid interception is explained in Section 5.4.

5.1. Lambert targeter

In order to determine the ballistic trajectory of a spacecraft departing from Earth and intercepting with the asteroid a Lambert targeter is used. Lambert's problem can be summarized as determining the velocity components $\vec{v_1}$ and $\vec{v_2}$, given two points $\vec{r_1}$ and $\vec{r_2}$ on an elliptical trajectory and the time of flight TOF in between the points, as sketched in Figure 5.1. The derivation of the Lambert targeter as presented here can be found in the work by Curtis, pages 202 until 208 [11].

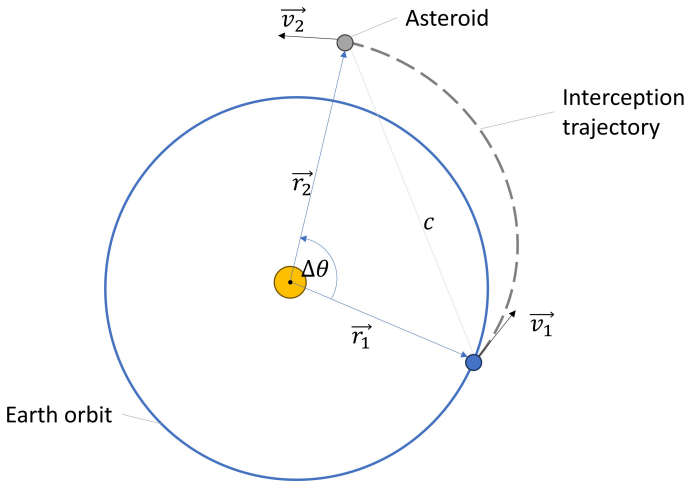

Figure 5.1: The setup of the Lambert targeter. In the general case, the spacecraft departs from Earth with a velocity v_1 and follows the dashed trajectory until it arrives at the target within flight time TOF.

The velocities in question can be written in terms of the Lagrange coefficients $f, \dot{f}$ and $g, \dot{g}$. The Lagrange coefficients are a set of 4 functions that fully determine an orbit based on an initial position and

velocity. Starting from:

$$\begin{aligned} \vec{r_2} &= f\vec{r_1} + g\vec{v_1} \\ \vec{v_2} &= \dot{f}\vec{r_1} + \dot{g}\vec{v_1} \end{aligned} \tag{5.1}$$

Now the equations are rearranged to solve for $\vec{v_1}$ and $\vec{v_2}$ in terms of the positions $\vec{r_1}$ and $\vec{r_2}$. Utilizing the constraint $f\dot{g} - \dot{f}g = 1$ the equations are:

$$\begin{aligned} \vec{v_1} &= \frac{1}{g}(\vec{r_2} - f\vec{r_1}) \\ \vec{v_2} &= \frac{1}{g}(\dot{g}\vec{r_2} - fr_1) \end{aligned} \tag{5.2}$$

The problem boils down to finding the roots of the function in Equation (5.3). The Newton secant method is used which is implemented in the SciPy package [49].

$$F(z) = \left[\frac{y(z)}{C_2(z)}\right]^{\frac{3}{2}} C_3(z) + A\sqrt{y(z)} - \sqrt{\mu}\Delta t \tag{5.3}$$

With z determined, the Lagrange coefficients can be computed with

$$\begin{aligned} f &= 1 - \frac{y(z)}{r_1} \\ g &= A\sqrt{\frac{y(z)}{\mu}} \\ \dot{f} &= \frac{\sqrt{\mu}}{r_1 r_2}\sqrt{\frac{y(z)}{C_2(z)}}[zC_3(z) - 1] \\ \dot{g} &= 1 - \frac{y(z)}{r_2}. \end{aligned} \tag{5.4}$$

The Lagrange coefficients are plugged into Equation (5.2) to get the velocity. The constant A is defined as

$$A = \sin\Delta\theta\sqrt{\frac{r_1 r_2}{1 - \cos\Delta\theta}}. \tag{5.5}$$

For reference, the Stumpff functions $C_2(z)$ and $C_3(z)$ are given, from Curtis page 136 [11].

$$\begin{aligned} C_2(z) &= \begin{cases} \frac{1-\cos\sqrt{z}}{z} & (z > 0) \\ \frac{\cosh\sqrt{-z}-1}{-z} & (z < 0) \\ \frac{1}{2} & (z = 0) \end{cases} \qquad \left(z = \alpha\chi^2\right) \\ C_3(z) &= \begin{cases} \frac{\sqrt{z}-\sin\sqrt{z}}{(\sqrt{z})^3} & (z > 0) \\ \frac{\sinh\sqrt{-z}-\sqrt{-z}}{(\sqrt{-z})^3} & (z < 0) \\ \frac{1}{6} & (z = 0) \end{cases} \end{aligned} \tag{5.6}$$

For the thesis, the Lambert solver implemented in the Pykep package is used. The tool is verified and was used for the initial design of ESA missions such as Hera [28].

5.2. Low-thrust trajectory

In order to evaluate the transfer trajectory for electric propelled spacecraft, an equivalent Lambert formulation for a continuously thrusting spacecraft is desired. To model a low-thrust transfer, a shape based method can be used.

As derived by Petropolous [36], an exponential sinusoid can represent the shape of a transfer trajectory with tangential thrust. As expanded upon by Izzo [29], the exponential sinusoid method is formulated as a Lambert targeter. In the fashion of the classic Lambert targeter for a ballistic trajectory, the input is the start and end position of the transfer and the result is the velocity at those two points.

Since no numerical propagation is required, the exponential sinusoid trajectory is fast to compute which is beneficial for evaluating a range of departure dates.

The mathematical expressions related to the exponential sinusoid are given in the following. A mass particle in a gravity field, expressed in polar coordinates r and θ, with a thrust acceleration a_{thrust} applied at an angle α, is given as

$$\begin{aligned} \ddot{r} - r\dot{\theta}^2 + \frac{\mu}{r^2} &= a_{thrust} \sin\alpha \\ \ddot{\theta} r + 2\dot{\theta}\dot{r} &= a_{thrust} \cos\alpha. \end{aligned} \tag{5.7}$$

The exponential sinusoid is defined as

$$r = k_0 \exp\left[k_1 \sin\left(k_2\theta + \phi\right)\right]. \tag{5.8}$$

Tangential thrust is assumed, where the thrust angle is equal to the flight path angle, $\alpha = \gamma$. The four parameters of the sinusoid $[k_0, k_1, k_2, \phi]$ can be linked to the angular rate of change $\dot{\theta}^2$ and the normalized thrust acceleration $a = \frac{a_{thrust}}{\mu/r^2}$.

$$\begin{aligned} \dot{\theta}^2 &= \left(\frac{\mu}{r^3}\right) \frac{1}{\tan^2\gamma + k_1 k_2^2 s + 1} \\ a &= \frac{\tan\gamma}{2\cos\gamma}\left[\frac{1}{\tan^2\gamma + k_1 k_2^2 s + 1} - \frac{k_2^2\left(1 - 2k_1 s\right)}{\left(\tan^2\gamma + k_1 k_2^2 s + 1\right)^2}\right] \end{aligned} \tag{5.9}$$

The flight path angle is defined as

$$\tan\gamma = k_1 k_2 \cos(k_2\theta + \phi). \tag{5.10}$$

For ease of formulation, the following helper functions are defined.

$$\begin{aligned} s &= \sin(k_2\theta + \phi) \\ c &= \cos(k_2\theta + \phi) \\ \tan\gamma &= k_1 k_2 c \end{aligned} \tag{5.11}$$

5.2.1. Lambert formulation

For the transfer, it is required that the exponential sinusoid passes through the start r_1 and end point r_2. This can be formulated as

$$\begin{cases} r_1 = k_0 \exp\left[k_1 \sin\phi\right] \\ r_2 = k_0 \exp\left[k_1 \sin\left(k_2\bar{\theta}_f + \phi\right)\right] \end{cases} \tag{5.12}$$

By assuming a value for the winding parameter k_2, the other two parameters k_0 and k_1 can be solved. The angle $\bar{\theta}_f$ is the angle that has to be traversed. The total traversed angle depends on the angle between the position vectors of start and end position and the number of allowed revolutions around the center body, and is related by $\bar{\theta}_f = \theta + 2\pi N$, with N the number of allowed revolutions. The angle θ can be calculated with the formula for the angle between two points on a sphere.

$$\theta_f = \arctan\frac{|\vec{r}_1 \times \vec{r}_2|}{\vec{r}_1 \cdot \vec{r}_2} \tag{5.13}$$

Dividing Equation (5.12), and taking the natural logarithm, it may be derived that

$$\frac{k_1}{|k_1|}\sqrt{k_1^2 - \frac{\tan^2\gamma_1}{k_2^2}} = \frac{\ln\frac{r_1}{r_2} + \frac{\tan\gamma_1}{k_2}\sin k_2\bar{\theta}_f}{1-\cos k_2\bar{\theta}_f}. \tag{5.14}$$

From the above equation, the sign of k_1 can be deduced.

$$sign(k_1) = sign\left(\ln\frac{r_1}{r_2} + \frac{\tan\gamma_1}{k_2}\sin k_2\bar{\theta}_f\right) \tag{5.15}$$

Determining k_1 is then straightforward with the following equation.

$$k_1^2 = \left(\frac{\ln\frac{r_1}{r_2} + \frac{\tan\gamma_1}{k_2}\sin k_2\bar{\theta}_f}{1-\cos k_2\bar{\theta}_f}\right)^2 + \frac{\tan^2\gamma_1}{k_2^2} \tag{5.16}$$

The phase angle can be calculated from Equation (5.10)

$$\phi = \arccos\left(\frac{\tan\gamma_1}{k_1 k_2}\right). \tag{5.17}$$

Then the last parameter, k_0, can be determined with

$$k_0 = \frac{r_1}{\exp\left(k_1\sin\phi\right)}. \tag{5.18}$$

Not all possible exponential sinusoids that connect the two points are feasible. The feasibility is dictated by the condition $|k_1 k_2^2| < 1$. As shown by Petropolous [36], from Equation (5.9) it is evident that when $|k_1 k_2^2|$ approaches unity, and the trajectory is at periapsis, where $s = -1$, then the $\dot{\theta}$ and a approach infinity. Petropolous further shows that, if $|k_1 k_2^2|$ is larger than 1 around the periapsis, then the angular rate of change $\dot{\theta}$ is less than zero. Starting from Equation (5.16), the feasibility condition can be rewritten as

$$\left(\frac{k_2^2\ln\frac{r_1}{r_2} + k_2\tan\gamma_1\sin k_2\bar{\theta}_f}{1-\cos k_2\bar{\theta}_f}\right)^2 + k_2^2\tan^2\gamma_1 < 1. \tag{5.19}$$

The expression is a quadratic function in γ_1, the starting flight path angle. The feasibility condition reveals that there is a range of feasible flight path angles between the two roots of the function. The minimum and maximum angle that give a feasible trajectory can be calculated by

$$\tan\gamma_{1_{max,min}} = \frac{k_2}{2}\left[-\ln\frac{r_1}{r_2}\cot\frac{k_2\bar{\theta}_f}{2} \pm \sqrt{\Delta}\right]. \tag{5.20}$$

The helper variable Δ is calculated with the following expression.

$$\Delta = \frac{2\left(1-\cos k_2\bar{\theta}_f\right)}{k_2^4} - \ln^2\frac{r_1}{r_2} \tag{5.21}$$

If $\Delta > 0$ the exponential sinusoid with a starting angle in between the two roots is feasible.

For a range of flight path angles, constrained by $\tan\gamma_{1_{max,min}}$, the time of flight curve for the possible flight path angles is obtained. A numerical root finding method is then used to find the intersection of this curve with the required time of flight. A robust and fast method is Brent's algorithm, which is available in the Scipy package [49]. An example of the time of flight curve is shown in Figure 5.4.

The time of flight is calculated by discretizing the trajectory into a number of steps, as sketched in Figure 5.2. Specifically, for a certain angle θ_i from 0 to $\bar{\theta}_f$, and a step in angle of $\Delta\theta$, the time of flight can be determined as the fraction of $\Delta\theta$ and the angular rate of change $\dot{\theta}$. The time of flight is then the sum

$$TOF = \sum_{i=1}^{i_{max}}\frac{\Delta\theta}{\dot{\theta}_i}. \tag{5.22}$$

For each segment, the necessary parameters of the trajectory are calculated. As an overview, the process to calculate the low-thrust trajectory is as follows.

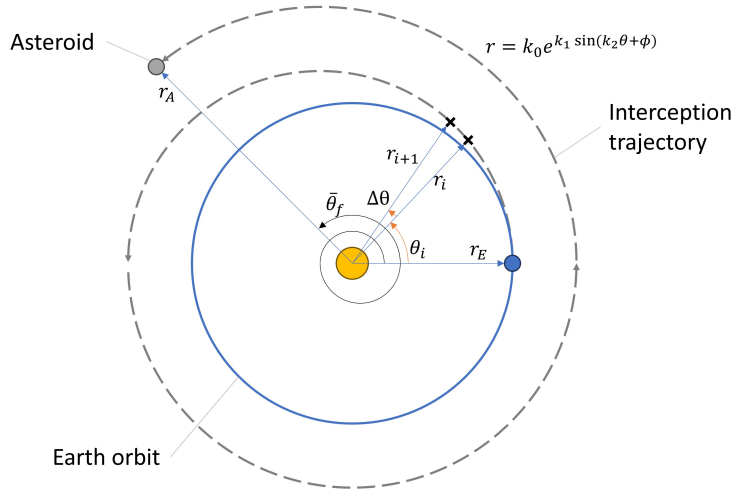

Figure 5.2: An example of an exponential sinusoid spiral. The dashed line indicates that the trajectory is discretized into segments.

1. Given are $\vec{r}_1, \vec{r}_2$ and the required time of flight TOF_{req}.
2. Calculate the angle between the start and end position, which is $\theta_f = \arctan \frac{|\hat{r}_1 \times \hat{r}_2|}{\hat{r}_1 \cdot \hat{r}_2}$.
3. Calculate the traversed angle, by assuming a number of allowed revolutions N_{rev}, which is $\bar{\theta}_f = \theta_f + 2\pi N_{rev}$.
4. For an assumed k_2-value, do the following:
   a. Calculate the boundaries $\gamma_{1_{max,min}}$ for the starting flight path angle. When $\Delta < 1$ the trajectory is infeasible.
   b. For a feasible flight path angle γ_1:
      i. Calculate k_1 and k_0 which determines a possible exponential sinusoid.
      ii. For each segment θ_i along the trajectory:
         1. Calculate the helper variables:

$$\begin{aligned} \gamma_i &= \arctan\left(k_1 k_2 c_i\right) \\ r_i &= k_0 \exp\left(k_1 s_i\right) \\ c_i &= \cos\left(k_2\theta_i + \phi\right) \\ s_i &= \sin\left(k_2\theta_i + \phi\right) \end{aligned} \tag{5.23}$$

         2. Calculate the angular velocity $\dot{\theta}_i$ and normalized thrust acceleration a_i for each segment with Equation (5.9).
         3. Calculate the thrust acceleration $a_{thrust} = a\frac{\mu}{r^2}$.
         4. Calculate the velocity change per segment and the total ΔV. This is done by integrating the thrust profile over the whole traversed angular distance. For each segment, the variable to integrate is $dV/d\theta$ from 0 to $\bar{\theta}_f$.

$$\frac{dV}{d\theta} = \frac{dV/dt}{d\theta/dt} = \frac{|a_{thrust}|}{\dot{\theta}} \tag{5.24}$$

            Then the total velocity change is the integral:

$$\Delta V = \int_0^{\bar{\theta}_f} \frac{|a_{thrust}|}{\dot{\theta}} d\theta \tag{5.25}$$

Applying the trapezoidal rule for numerical integration, the ΔV for each segment is:

$$\Delta V_i = (\theta_{i+1} - \theta_i)\,\frac{1}{2}\left(\frac{|a_{thrust,i+1}|}{\dot{\theta}_{i+1}} - \frac{|a_{thrust,i}|}{\dot{\theta}_i}\right) \tag{5.26}$$

5. Calculate the spacecraft mass at each instant with the rocket equation.

$$m_{i+1} = \exp\left(-\frac{\Delta V_i}{I_{sp} g_0}\right) \cdot m_i \tag{5.27}$$

6. Calculate the thrust force at each segment of the transfer.

$$T_i = m_i \cdot a_{thrust,i} \tag{5.28}$$

The main result of the Lambert formulation is the velocity at end of the transfer as well as the mass of the spacecraft. The equations to calculate the velocities are the following.

$$\vec{V}_r = \dot{r} \cdot \hat{r}, \quad \vec{V}_\theta = r\dot{\theta}\left[(\hat{r}_1 \times \hat{r_2}) \times \hat{r}\right], \quad \vec{V} = \vec{V}_r + \vec{V}_\theta \tag{5.29}$$

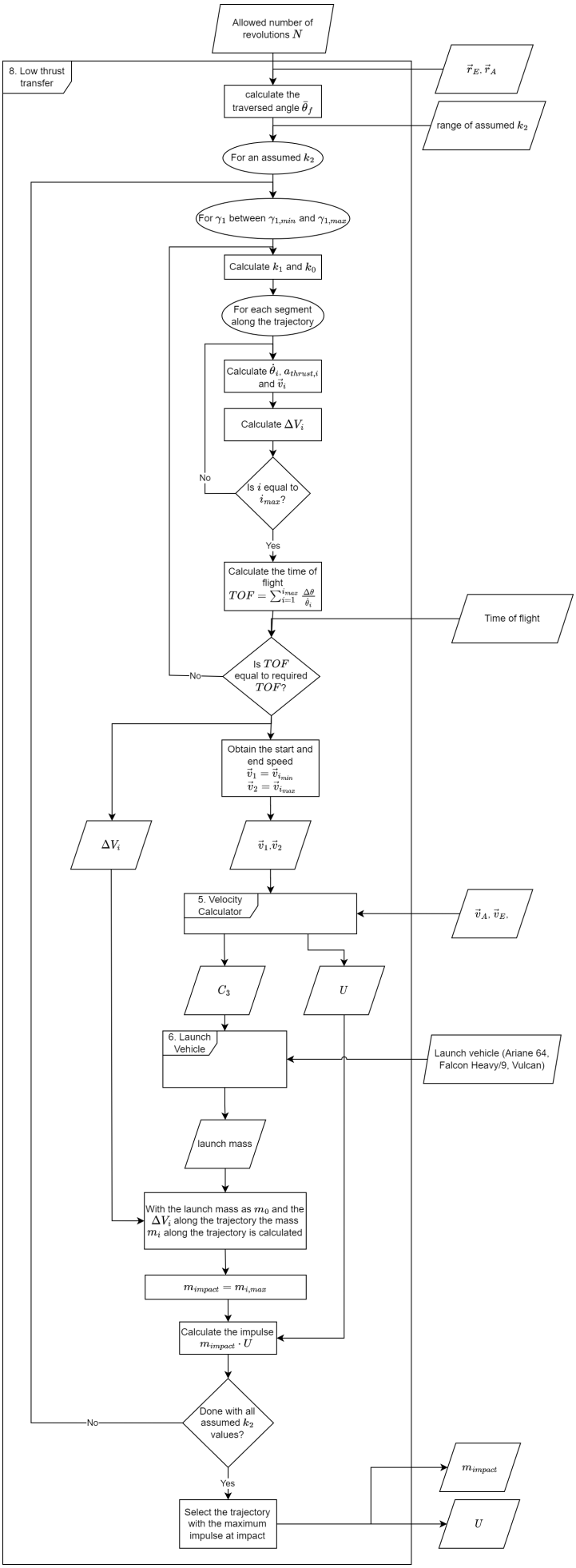

Figure 5.3: Flow chart for the impact mass and impact speed for the exponential sinusoid trajectory.

On the left side, in Figure 5.3, the flow chart details the implementation of Izzo's formulation of the Lambert problem for an exponential sinusoid. Applying the exponential sinusoid for the kinetic impactor requires that the spacecraft mass at the end of the trajectory is calculated. The shape of the trajectory is dictated by the winding parameter k_2. The impact speed and impact mass, and therefore the spacecraft momentum, are a function of k_2. The trajectories are evaluated for a a range of k_2-values and the trajectory which maximizes the momentum is selected. For an assumed k_2, a range of feasible starting flight path angles is determined. An inner loop runs Brent's algorithm, to find the flight path angle that results in a trajectory which matches the input time of flight. Brent's algorithm is evaluating the trajectory along i segments to obtain the time of flight.

When a suitable trajectory is found, the start and end velocity of the transfer trajectory are obtained with Equation (5.29). The start velocity is required to find the characteristic energy that has to be supplied by the launch vehicle to start the interplanetary trajectory. The vector difference between the end velocity and the asteroid orbital velocity gives the impact velocity of the spacecraft on the asteroid. The payload capability of the launch vehicle is a function of C_3, as shown in Section 2.5. The available launch mass, assuming a direct insertion of the spacecraft into the interplanetary trajectory, is combined with the ΔV along the trajectory to determine the propellant consumption and eventually the impact mass.

5.2.2. Verification

The exponential sinusoid trajectory can be verified with the results from Izzo [29] and Moreno [34], who implemented the Lambert formulation as well. First of all, it is checked if the time of flight is correctly calculated. For the purpose of verification, an example trajectory is used with parameters reported in Table 5.1. The trajectory represents an Earth-Mars transfer.

Table 5.1: The parameters for the verification of the time of flight for a low-thrust trajectory.

Name	Symbol	Value	Unit
Winding parameter	k_2	$1/12$	-
Start distance	r_1	1	AU
End distance	r_2	1.5	AU
Angular distance	θ_f	$\pi/2$	rad
Number of revolutions	N	0,1,2,3,4 and 5	-

The time of flight, in years, is compared to the results by Izzo and is reported as a function of the starting flight path angle γ_1. The result is shown in Figure 5.4. The number of revolutions is varied between 0 and 5. The results deviate marginally with the time of flight reported by Izzo, but agree with the implementation by Moreno. To check convergence, the number of angular segments, along which the acceleration along the trajectory is calculated, is varied from 64 to 1024. Acceptable convergence and computation time is achieved with 256 segments, which is used for the remainder of this work.

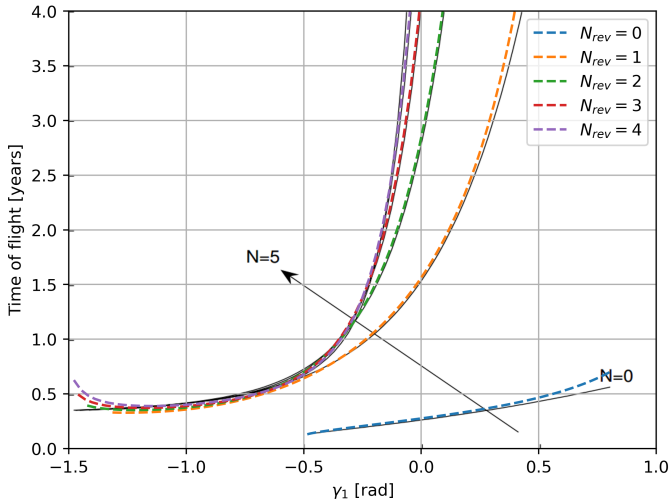

Figure 5.4: The time of flight as a function of the starting flight path angle for the exponential sinusoid with the parameters from Table 5.1. The solid lines are taken from Figure 2 in Izzo's publication [29] of the Lambert formulation. The dotted lines are the results of the implementation.

By further checking the ΔV and comparing to existing implementations, the calculation of acceleration and angular velocity can be checked. Moreno [34] reports ΔV-values for an exemplary Earth-Mars transfer, with parameters listed in Table 5.2. The position of Earth and Mars for the transfer are taken from the JPL Low Precision Ephemerides Service. The shape of the reference trajectory is compared to the current implementation in Figure 5.5.

The ΔV of the reference transfer is shown in Figure 5.6. The plot shows the ΔV along the trajectory with parameters from Table 5.2, with an additional offset in start date and time of flight. The results are in good agreement and the iplementation of the exponential sinusoid is further used in the mission design.

Table 5.2: The parameters for the reference Earth-Mars transfer. The start day is given in Modified Julian Dates (MJD).

Name	Symbol	Value	Unit
Number of revolutions	N	0	-
Winding parameter	k_2	0.928	-
Time of flight	TOF	206	days
Start of transfer	t_{start}	4401.5	MJD

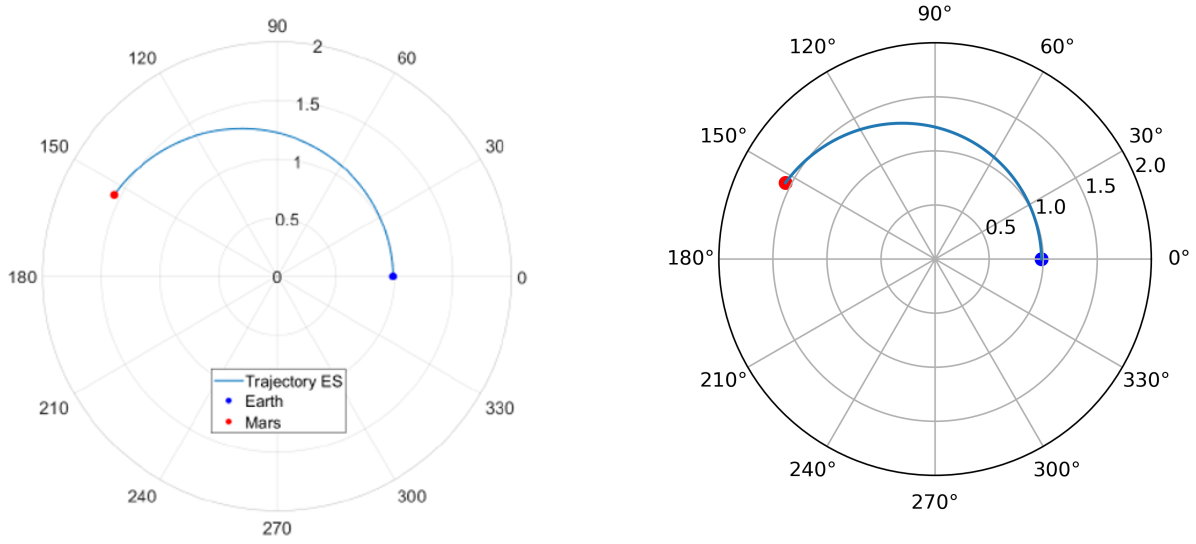

(a) The reference trajectory, taken from Moreno [34].

(b) Trajectory from the implementation.

Figure 5.5: The comparison between the reference trajectory for an Earth-Mars transfer for a time of flight of 206 days, a starting epoch of 4401.5 MJD and $k_2 = 0.928$. The unit of length is AU.

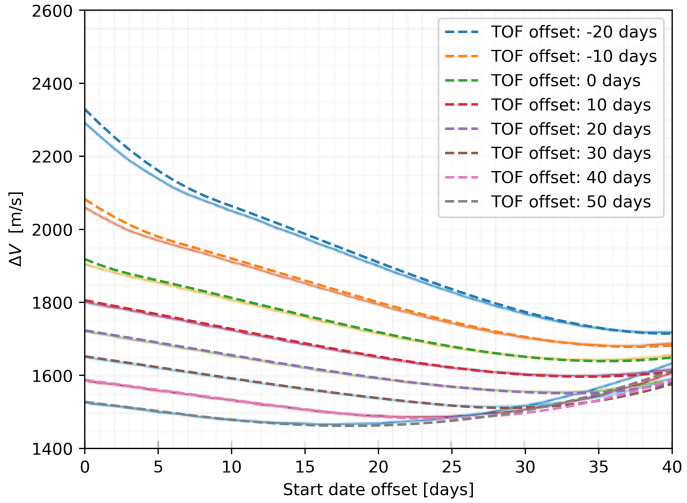

Figure 5.6: The ΔV for the reference Earth-Mars transfer. The x-axis is the deviation from the start day at 4401.5 MJD. The time of flight is varied and each line represents a deviation from the transfer time of 206 days. The dotted lines are computed with the current implementation and the solid lines are from Moreno [34].

5.3. Planetary Departure

An important result of the Lambert targeter is the velocity required to place the spacecraft on an intercepting elliptical orbit with the NEO. Relevant for the mission is the change in velocity Δv required to raise the velocity of the spacecraft in a parking orbit around Earth to the velocity required to follow the interception trajectory. The situation is sketched in Figure 5.7.

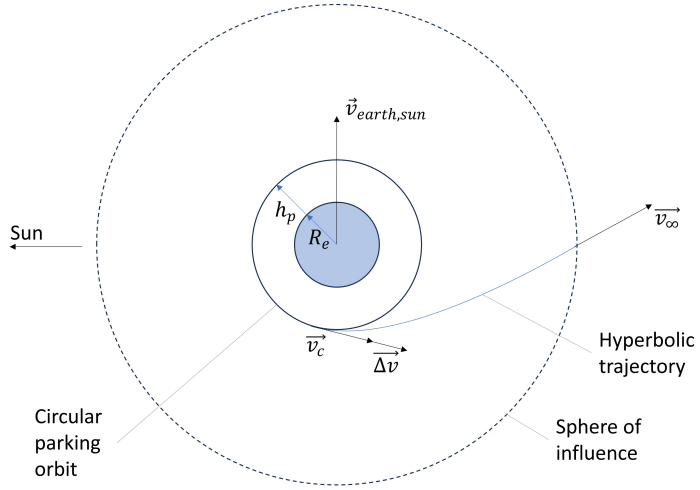

Figure 5.7: The spacecraft is in a parking orbit with height h_{park} around Earth. The objective is to find the Δv required to reach a certain hyperbolic excess velocity.

In the inertial frame, a certain velocity of the spacecraft with respect to the Sun $\vec{v}_{sc,sun}$ is required to enter the interception orbit. Due to the fact that the Earth is moving around the Sun with velocity $\vec{v}_{earth,sun}$, the hyperbolic excess velocity is the vector difference between the two.

$$v_\infty = |\vec{v}_{sc,sun} - \vec{v}_{earth,sun}| \tag{5.30}$$

The velocity of the spacecraft on the circular parking orbit is constant and computed as

$$v_c = \sqrt{\frac{\mu_{earth}}{R_e + h_{park}}}. \tag{5.31}$$

The specific orbital energy of the escape hyperbola is the following.

$$\frac{v_\infty^2}{2} = \frac{(v_c + \Delta v)^2}{2} - \frac{\mu}{(R_e + h_{park})} \tag{5.32}$$

The equation has two solutions for Δv, out of which the positive is selected.

$$\Delta v = \sqrt{v_\infty^2 + \frac{2\mu_{earth}}{R_e + h_{park}}} - v_c \tag{5.33}$$

A heavy-lift launch vehicle can be capable of supplying the required Δv, either partially or in full. Otherwise, the on-board propulsion system of the spacecraft has to be used. In this thesis, the deflection performance of a kinetic impactor departing from a circular parking orbit, from a GTO, and directly inserted by the launch vehicle is compared.

5.4. Asteroid Interception

The flight time of the spacecraft from Earth to the asteroid has to be assumed in order to find a solution for the interception trajectory. The result of the Lambert targeter is the velocity of the spacecraft in the inertial frame at the time of interception. As outlined in Section 5.3, the Δv requirement can be calculated by assuming the height of the circular parking orbit.

The impact situation of the spacecraft and the NEO is sketched in Figure 5.8. The main result is the direction of the deflection due to the kinetic impact and the velocity of the spacecraft with respect to the asteroid $\vec{v}_{sc,a}$. The velocity of the spacecraft $\vec{v}_{sc}$ is a result of the Lambert targeter.

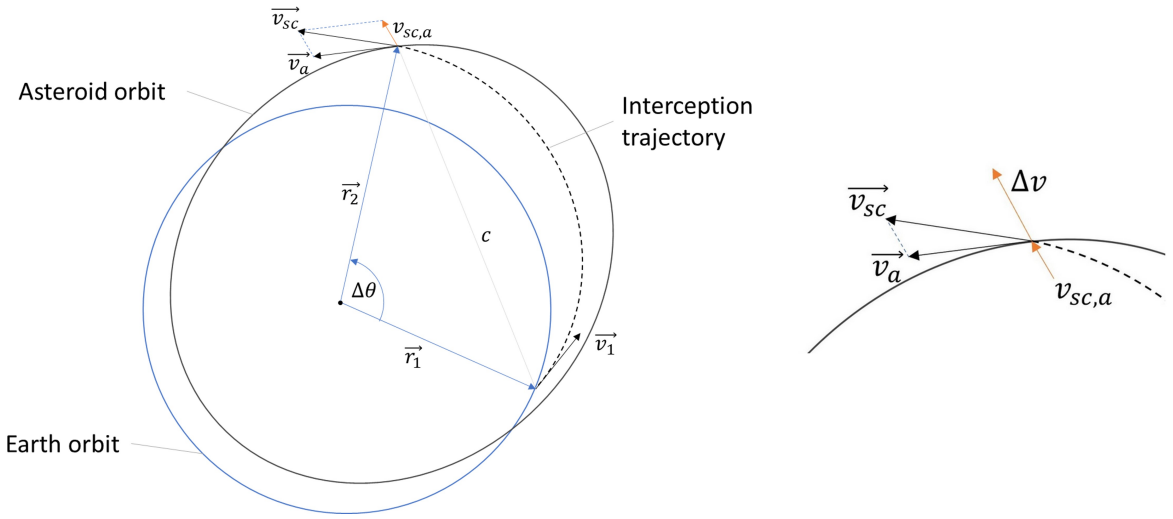

Figure 5.8: The spacecraft follows the interception trajectory, indicated by the dashed line. At the impact, a Δv is imparted to the NEO in the direction of the relative velocity $v_{sc,a}$ between the spacecraft and the asteroid.

The direction of the Δv due to the kinetic impact is the same as the relative velocity of the spacecraft with respect to the asteroid.

$$\vec{v}_{sc,a} = \vec{v}_{sc} - \vec{v}_a \tag{5.34}$$

The magnitude of the Δv follows from the momentum enhancement due to ejecta, with M the mass of the asteroid. When defining the impact speed as $U = |\vec{v}_{sc,a}|$ and the impact mass as $m_{impact} = m_{sc}$, the velocity change given to the asteroid, further used as the figure of merit J, is defined as

$$\begin{aligned} \beta &= \frac{M\Delta v}{m_{impact}U} \\ J &= \beta\frac{m_{impact}U}{M}. \end{aligned} \tag{5.35}$$

The momentum enhancement factor is calculated with the scaling laws as outlined in Chapter 3.

6 Results

In the following chapter the results of the impulse calculation for the kinetic impactor are presented. First of all, the generated asteroid orbit is described in Section 6.1. The results for the different configurations are independently presented in Section 6.2. The performance of the proposed concepts is compared in Section 6.3. After the results are presented for a single reference asteroid, the analysis is repeated for a large number of cases in Section 6.4. Conclusions are drawn in Section 6.5 and the method is reflected on in Section 6.6.

6.1. Target

The asteroid target is generated using the method explained in Section 4.1, the orbital elements are given in Table 6.1 and visualized in Figure 6.1.

Parameter	Symbol	Value	Unit
Semi-major axis	a	1.92	AU
Eccentricity	e	0.51	-
Inclination	i	15.22	degrees
Right ascension of the ascending node	Ω	100.68	degrees
Argument of periapsis	ω	328.61	degrees
Mean anomaly	M	8.97	degrees

Table 6.1: The orbital elements of the asteroid target.

The scaling constants and physical parameters used in the scaling laws are given in Appendix A.

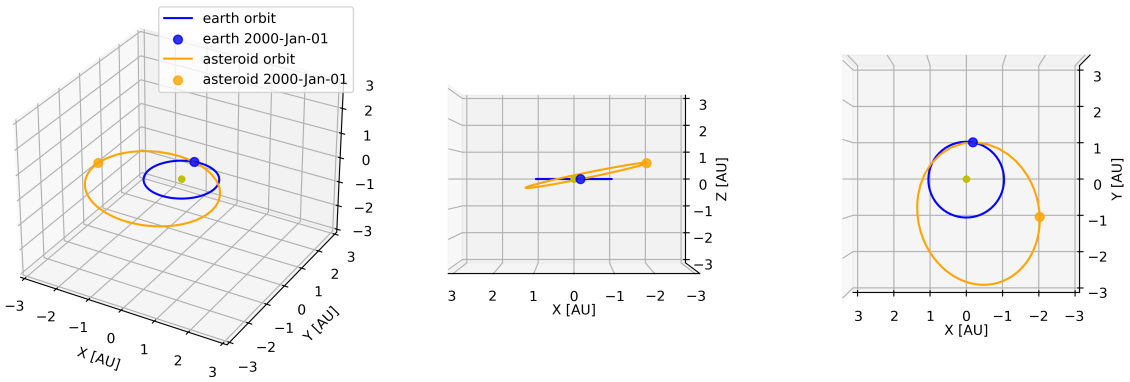

Figure 6.1: The orbit of the reference target, associated with the orbital elements in Table 6.1.

The problem is set up with a range of start dates and time of flights. The time of flight ranges from 4 months to 24 months. The start date is between January 1st 2027 and January 1st 2029. The hypothetical threat scenario is an asteroid that is projected to impact Earth in 2034.

6.2. Deflection performance

Each configuration is briefly described and the results for the mission scenario are given.

ID1: Direct insertion, assembled impactor

If the launch vehicle is providing the insertion of the spacecraft into the interception orbit with the asteroid, the launcher second stage can stay attached to the spacecraft to enhance the impact mass. The departure opportunities are analysed on a 100 by 100 point grid, which translates into a resolution of 7.3 days for the launch date and 6.1 days for the time of flight.

The porkchop plot in Figure 6.2 shows the C_3 for the selected start dates and time of flight to the asteroid. The upper threshold for the C_3 is 50 km^2/s^2, which is the maximum value of Falcon Heavy, the most capable of the selected launch vehicles [6]. The overall lowest C_3 of 16.7 km^2/s^2, indicated by a red dot in Figure 6.2, is not reachable by a Falcon 9 according to [6]. The direct insertion has to be performed by Ariane, Falcon Heavy or Vulcan.

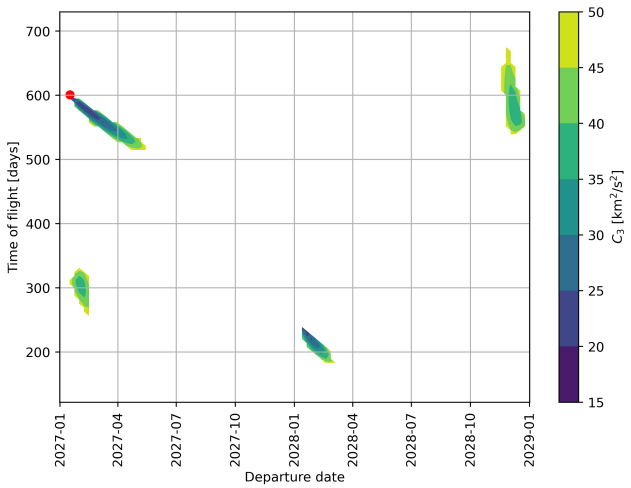

Figure 6.2: The required characteristic energy of a launch vehicle for a target insertion of a spacecraft into a transfer trajectory to the reference asteroid.

For each of the departure opportunities, the impact momentum of the spacecraft is calculated and reveals the contour plots in Figure 6.3. The difference between the launch vehicle options is the launch mass for the same C_3, therefore the maximum momentum, which is positively correlated with the impact efficiency β, differs between the plots, but the shape is the same. Selecting the trajectory with the highest momentum and going through the process of calculating the deflection performance J, the results for each launch vehicle can be plotted in Figure 6.4. The numerical values are reported in Table 6.2.

Table 6.2: The results for the deflection for an assembled impactor for each launch vehicle.

Launch vehicle	Deflection J [m/s]	Impact efficiency β [-]	Departure date [DD-MM-YYYY]	Time of flight TOF [days]
Ariane 64	0.206	5.780	16-03-2027	558
Falcon 9	NA	NA	NA	NA
Falcon Heavy	0.304	6.243	558	558
Vulcan	0.283	6.154	558	558

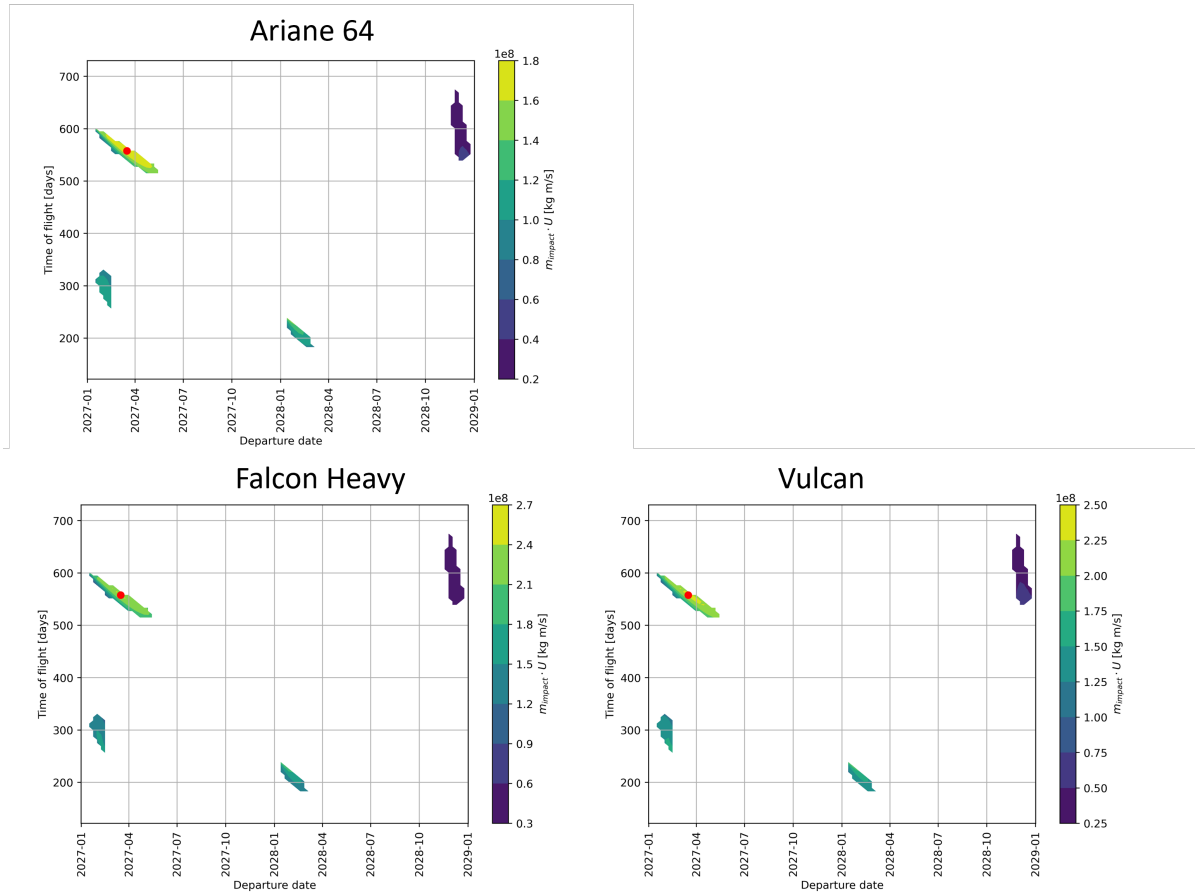

Figure 6.3: The impact momentum of the assembled kinetic impactor, deployed via direct insertion into the ballistic transfer trajectory. The momentum differs between the launch vehicles. Falcon 9 does not have sufficient C_3 and is not shown.

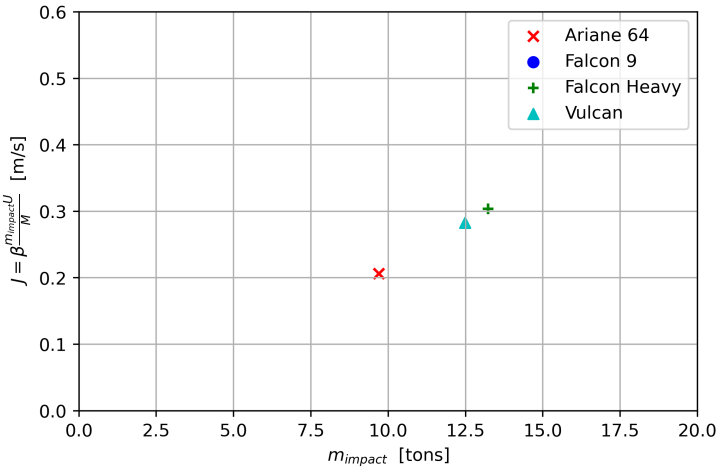

Figure 6.4: The performance parameter J for the assembled impactor, which is delivered directly to the interplanetary trajectory by the launch vehicle. Falcon 9 is not capable of directly inserting the spacecraft and is not shown in the figure.

ID2: Direct insertion, classic kinetic impactor

In contrast to the previous configuration, the classic kinetic impactor does not have the second stage of the launch vehicle attached until impact.to depart Earth's gravity well. The required C_3 stays the same, and is plotted in Figure 6.2. The difference lies in the momentum, and is compared for different launch vehicles in Figure 6.5.

The comparison of the figure of merit for the launch vehicles is shown in Figure 6.5 and reported in Table 6.3

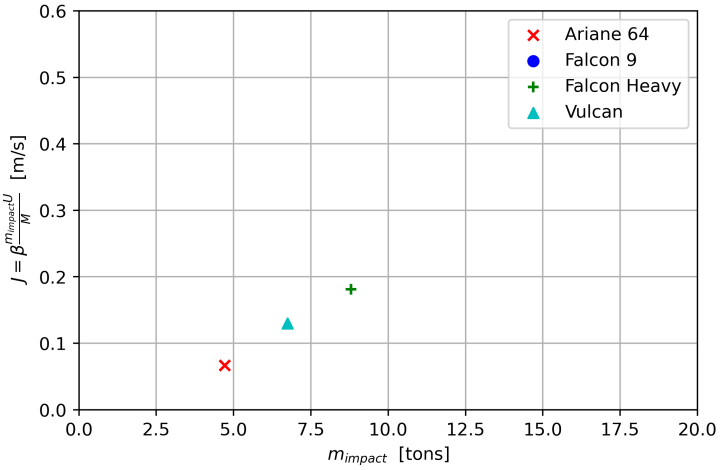

Figure 6.5: The deflection performance of the direct insertion mission is compared for different launch vehicles. Falcon 9 is missing because it cannot deliver the minimum necessary characteristic energy.

Table 6.3: The results of ID2, the classic impactor with direct insertion, for the time of flight, departure date and the deflection performance for each launch vehicle.

Launch vehicle	**Deflection** J [m/s]	**Impact efficiency** β [-]	**Departure date** [DD-MM-YYYY]	**Time of flight** TOF [days]
Ariane 64	0.067	4.595	14-02-2027	576
Falcon 9	NA	NA	NA	NA
Falcon Heavy	0.181	5.632	08-03-2027	564
Vulcan	0.130	5.276	08-03-2027	564

ID3: Circular parking orbit and bi-propellant on-board propulsion

In this scenario, each launch vehicle is used to bring a spacecraft to an orbital height of 500km. The payload capability of the launcher determines how much mass can be brought to this type of orbit. Then a porkchop plot is generated, which shows the required Δv to bring the spacecraft on an interplanetary trajectory. The plot is shown in Figure 6.6. The figure shows possible departure windows for the spacecraft, where the fuel mass required is less than the initial spacecraft mass. Otherwise the Δv requirement is so high that a transfer is infeasible.

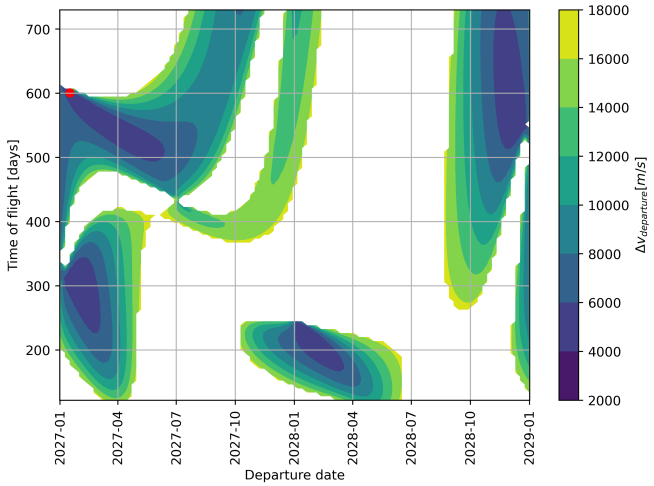

Figure 6.6: The porkchop plot for a circular parking orbit of 500km height shows possible departure windows for the spacecraft and the required $\Delta v_{departure}$. The red dot indicates the lowest $\Delta v_{departure}$.

Combined with the characteristics of the reference propulsion system, with an I_{sp} of 321s as defined in Section 2.6, the propellant mass required for Earth departure is found and hence the impact mass. Therefore, for each launch vehicle, the impact mass is slightly different, because even though they depart from the same starting orbit, the starting mass of the spacecraft is different depending on the launch vehicle.

Going through the process of calculating the impact mass and impact speed eventually reveals the departure window that result in the highest momentum. The momentum is positively correlated with β, so the highest momentum also results in the highest impact efficiency. Just like the characteristic energy, the momentum can be plotted as a contour, and is different for each of the launchers. The result is shown in Figure 6.7. As obvious from the figure, the shape of the contour plot coincides for each launch vehicle, which mean that the difference in available launch mass does not have a significant impact on the available launch opportunities. The important difference is in the momentum at impact, which can be seen the scaling of the contour plots.

Table 6.4: The results for ID3, the kinetic impactor that departs from a circular parking orbit with a bi-propellant propulsion system.

Launch vehicle	**Deflection** J [m/s]	**Impact efficiency** β [-]	**Departure date** [DD-MM-YYYY]	**Time of flight** TOF [days]
Ariane 64	0.091	4.923	16-03-2027	558
Falcon 9	0.107	5.082	16-03-2027	558
Falcon Heavy	0.387	6.552	16-03-2027	558
Vulcan	0.124	5.227	16-03-2027	558

For the departure window with the highest momentum, the impact efficiency is calculated with the method described in Chapter 3 and the performance indicator, the velocity change of the asteroid, is obtained. The figure of merit as calculated for the different launch vehicles is shown in Figure 6.8. It turns out that the launch vehicle capability drives the performance, with the Falcon Heavy outperforming all other options due to its high payload capability to low earth orbit. The numerical values are reported in Table 6.4

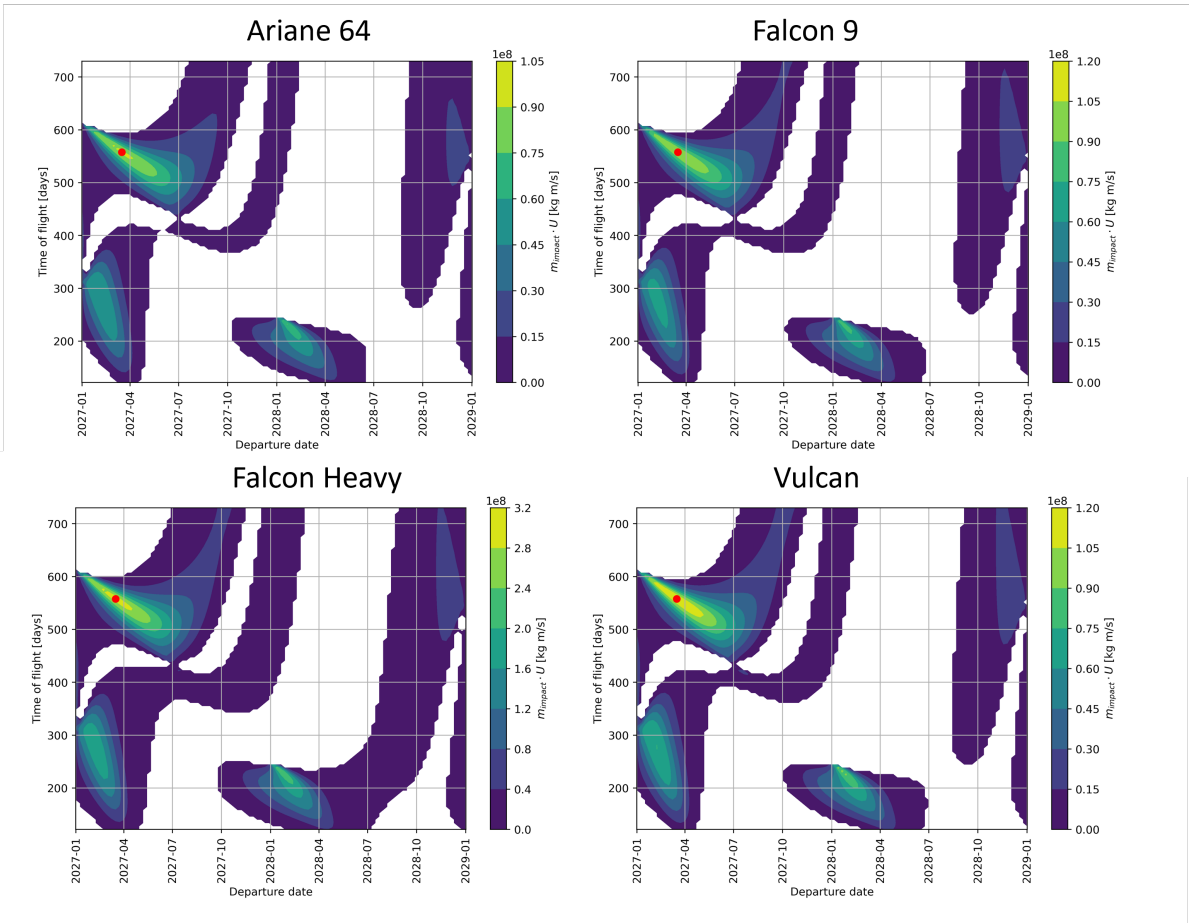

Figure 6.7: The spacecraft impact momentum, which is expressed as impact speed multiplied by impact mass, for the circular 500km parking orbit with a liquid bi-propellant system used for Earth departure. The red dot indicates the highest momentum.

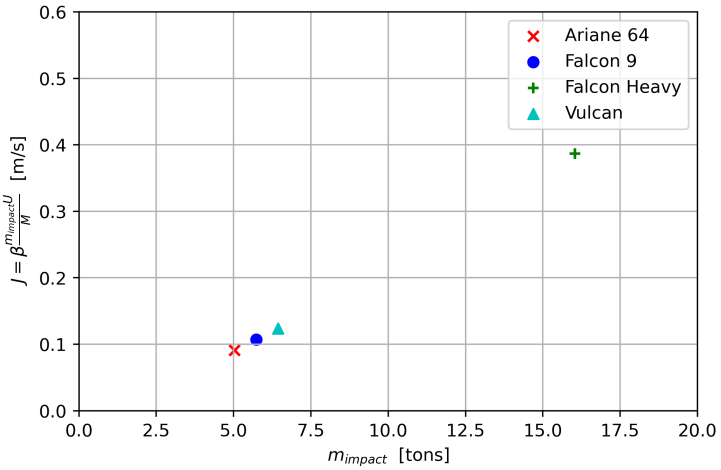

Figure 6.8: The figure of merit for a spacecraft departing from a circular parking orbit, delivered by different launch vehicles.

ID4: GTO parking orbit and bi-propellant on-board propulsion

The results for an elliptical parking orbit, specifically a GTO, are presented in the following. Again, the required $\Delta v_{departure}$ to reach the reference asteroid is shown in Figure 6.9.

The resulting momentum of the spacecraft is then shown as a function of launch date and time of flight

in Figure 6.10. The spacecraft is assumed to depart Earth via an impulsive shot at periapsis of the parking orbit. Due to the fact that the orbital velocity is highest at periapsis, the C_3 requirement for departure is reduced in comparison to the circular parking orbit.

The figure of merit for the different launch vehicles is shown in Figure 6.11 and the numerical values are given in Table 6.5. The influence of the launch vehicle performance is clearly visible and the spacecraft launched by Falcon Heavy is outperforming the others.

Table 6.5: The results for ID4, the kinetic impactor departing from a GTO with a bi-propellant propulsion system.

Launch vehicle	**Deflection** J [m/s]	**Impact efficiency** β [-]	**Departure date** [DD-MM-YYYY]	**Time of flight** TOF [days]
Ariane 64	0.118	5.181	16-03-2027	558
Falcon 9	0.079	4.788	16-03-2027	558
Falcon Heavy	0.338	6.379	16-03-2027	558
Vulcan	0.157	5.474	16-03-2027	558

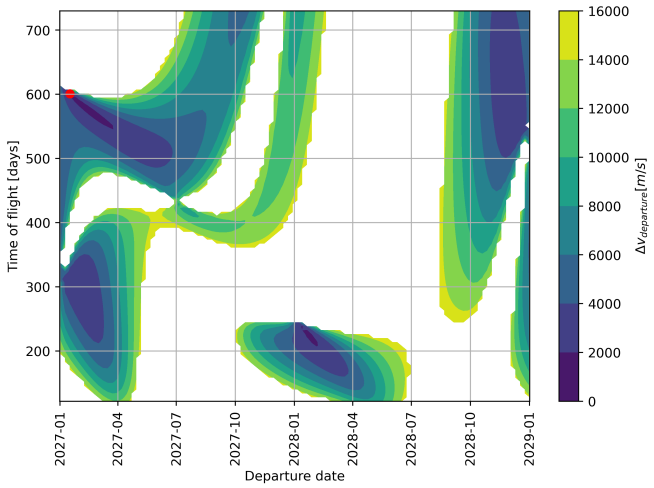

Figure 6.9: The porkchop plot for Earth departure from a GTO parking orbit.

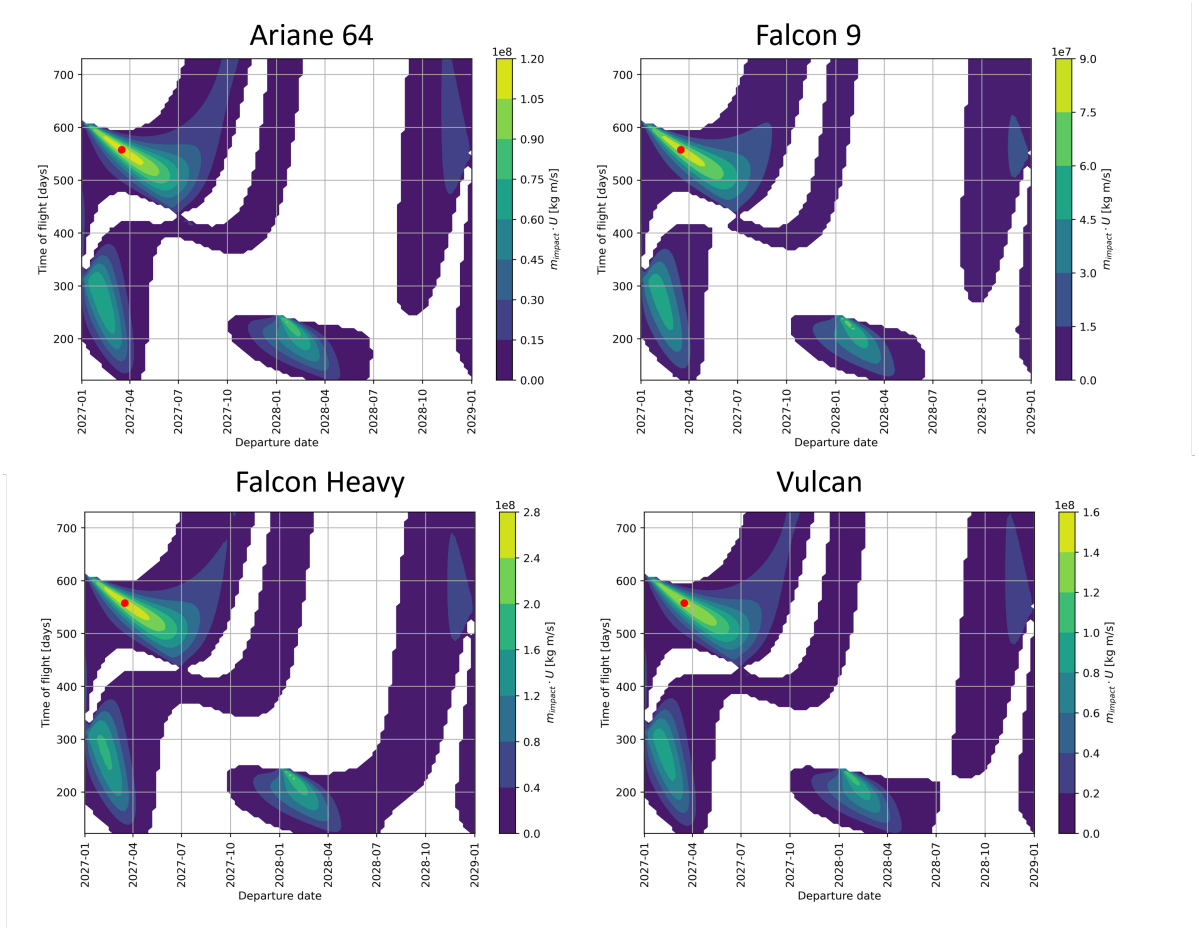

Figure 6.10: The spacecraft momentum for a spacecraft departing from a GTO with a bi-propellant propulsion system, grouped by launch vehicle. The red dot indicates the highest momentum.

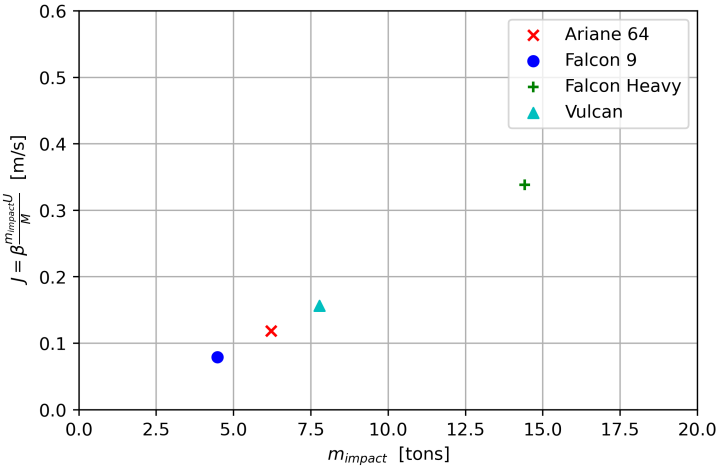

Figure 6.11: The comparison of the figure of merit for the GTO commissioning option with a biliquid propulsion system.

ID5: Low thrust trajectory

The results of the low-thrust trajectory, including the required C_3 and the resulting J, are presented in the following. The implemented exponential sinusoid has the functionality to vary the number of allowed revolutions. For example, when the number of revolutions is allowed to be 1, the transfer

trajectory can complete a full revolution before arriving at the target. It is assumed that the low-thrust spacecraft is delivered to the interplanetary trajectory directly by the launch vehicle. The difference between the launch vehicles is the payload mass that can be delivered for the same C_3. When the number of allowed revolutions N_{rev} is changed, the C_3 requirement changes, as seen in Figure 6.12.

The impact momentum is different for each launch vehicle due to the difference in payload capacity for the same C_3. As an example, the results for Ariane 64 are shown in Figure 6.13. Comparing to Figure 6.12, it is evident that the point of lowest C_3 does not necessarily coincide with the highest momentum.

The shape of the orbit for the case with Ariane 64 as the launcher, to show the difference between the number of revolutions, is shown in Figure 6.14. The green arrows indicate the direction and magnitude of the start and end velocity of the low-thrust trajectory, represented by the dashed line.

The comparison of the performance for the low-thrust trajectory is grouped by launch vehicle and then compared with the result for different numbers of allowed revolutions. Again, the performance of the launch vehicle plays a role as seen in Figure 6.15. The respective numerical values of the results are given in Table 6.6

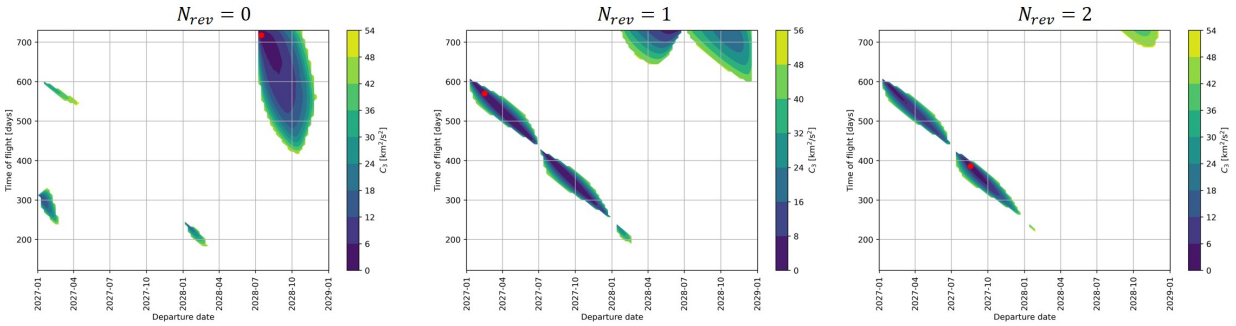

Figure 6.12: The required C_3 for a low thrust transfer to the reference asteroid.

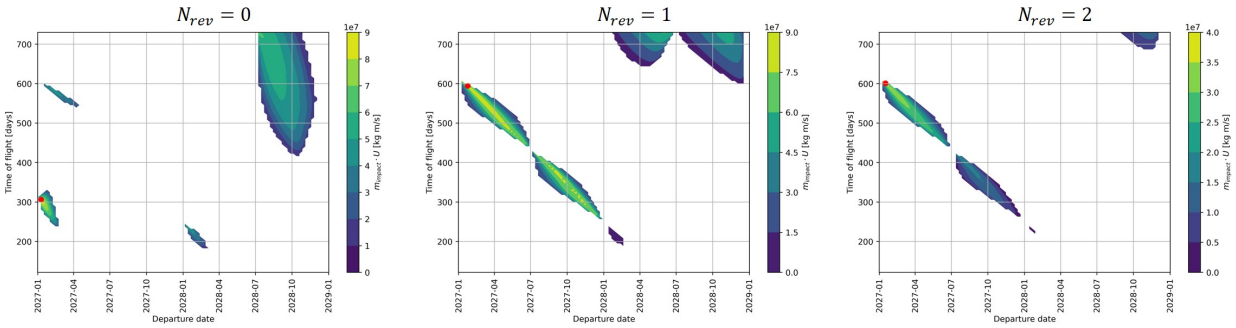

Figure 6.13: The impact momentum for the low-thrust trajectory for different numbers of revolution.

ID6: Circular parking orbit and solid kick stage

Instead of using a bipropellant system, a solid kick motor is considered for departure from Earth. Similar to the bipropellant case, a circular parking orbit and a GTO are analysed. Since the circular parking orbit is the same, the same Δv requirement as shown in Figure 6.6 applies. Starting from the Δv, the mass fraction of the spacecraft can be calculated from the rocket equation and, with the propellant mass of the solid motor, the impact mass of the spacecraft is determined.

Therefore, depending on the type of solid motor, the resulting momentum varies. The figure of merit J is determined for each solid motor (Figure 6.16). Because the propellant mass, the parking orbit and the ΔV are constrained, the impact mass of the spacecraft is decoupled from the launch vehicle. One caveat is that the largest solid motor, the Castor 30XL, can only be launched by a Falcon Heavy due to

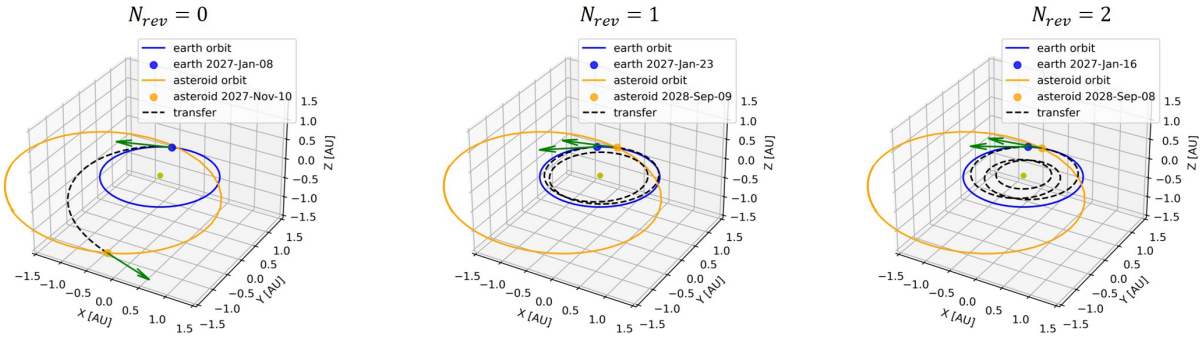

Figure 6.14: The maximum momentum trajectory from Earth to the reference asteroid with different numbers of revolution. The black dashed line is the transfer, with the green arrows indicating the start and end velocity of the transfer.

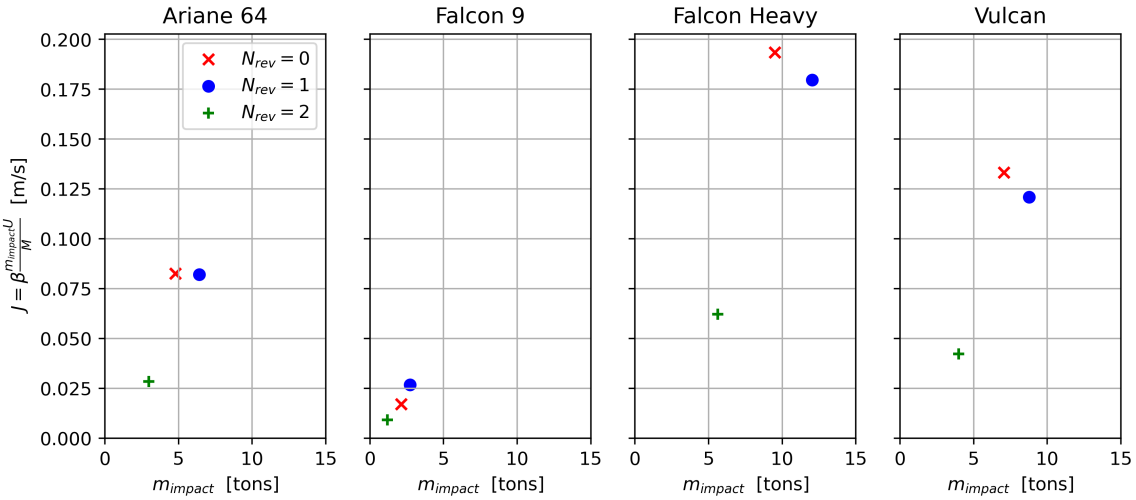

Figure 6.15: The performance of the low-thrust spacecraft, compared for different launch vehicles and allowed revolutions around the Sun before impacting the asteroid.

Table 6.6: The results for the configuration ID5. The results are grouped by allowed revolutions of the low-thrust spiral trajectory.

N_{rev}	Launch vehicle	Deflection J [m/s]	Impact efficiency β [-]	Departure date [DD-MM-YYYY]	Time of flight TOF [days]
0	Ariane 64	0.082	4.824	08-01-2027	306
	Falcon 9	0.018	3.533	08-07-2028	730
	Falcon Heavy	0.195	5.712	08-01-2027	306
	Vulcan	0.135	5.310	08-01-2027	306
1	Ariane 64	0.080	4.729	23-01-2027	595
	Falcon 9	0.026	3.812	16-01-2027	601
	Falcon Heavy	0.176	5.512	23-01-2027	595
	Vulcan	0.118	5.100	23-01-2027	595
2	Ariane 64	0.026	3.811	16-01-2027	595
	Falcon 9	0.009	3.095	16-01-2027	601
	Falcon Heavy	0.058	4.423	16-01-2027	595
	Vulcan	0.039	4.114	23-01-2027	595

its high wet mass. Otherwise, all launch vehicles can bring every solid stage into the circular parking orbit, and the performance J is the same for each solid motor and launch vehicle. The results are given in Table 6.7.

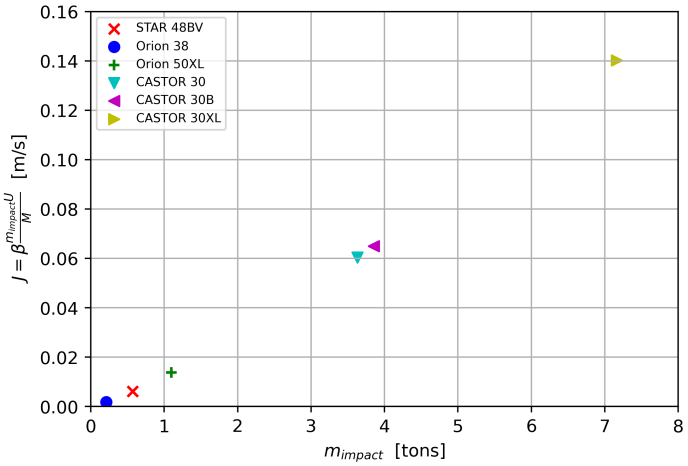

Figure 6.16: The change in velocity J of the asteroid due to the kinetic impact for each solid motor used for Earth departure from a 500km parking orbit.

Table 6.7: The results for the configuration ID6, a solid kick motor departing from a circular parking orbit.

Solid motor	**Deflection** J [m/s]	**Impact efficiency** β [-]	**Departure date** [DD-MM-YYYY]	**Time of flight** TOF [days]
STAR 48BV	0.006	2.976	08-03-2027	564
Orion 38	0.002	2.415	08-03-2027	564
Orion 50XL	0.014	3.442	08-03-2027	564
CASTOR 30	0.06	4.545	08-03-2027	564
CASTOR 30B	0.065	4.61	08-03-2027	564
CASTOR 30XL	0.14	5.355	08-03-2027	564

ID7: GTO parking orbit and solid kick stage

A solid motor can also be used to depart from an elliptical GTO. For this options, the limitations of the launch vehicle become more pronounced, because the payload mass to a GTO is more constrained than to a LEO.

The propellant mass and specific impulse for each of the commercial solid motors is known. At the same time, the spacecraft has to reach a specific v_1 at the start of the ballistic transfer trajectory. So, from the required Δv to reach the starting velocity and the I_{sp}, the ratio of final and initial mass is determined. From this, the mass of the spacecraft at launch can be determined. If the mass at launch is higher than the payload capability of the launch vehicle to GTO, the solution is infeasible. A similar constraint is true for the dry mass of the spacecraft, which has a lower limit of 100kg.

The performance parameter J is shown for each of the launch vehicles and solid motors in Figure 6.17. In the figure it can be seen that the departure and commissioning for the three smallest solid motors is the same, which means that all launchers can deliver them to the GTO, and they depart on the same transfer trajectory that results in the maximum momentum at impact. Vulcan is additionally able to deliver Castor 30 and Castor 30B, but the sparse departure opportunities result in a less optimal transfer trajectory and therefore a lower momentum. This can be seen in Figure 6.18, which compares the resulting impact momentum for Vulcan, grouped by solid motor. The Falcon Heavy can deliver all kick stages, and the results are given in table 6.8

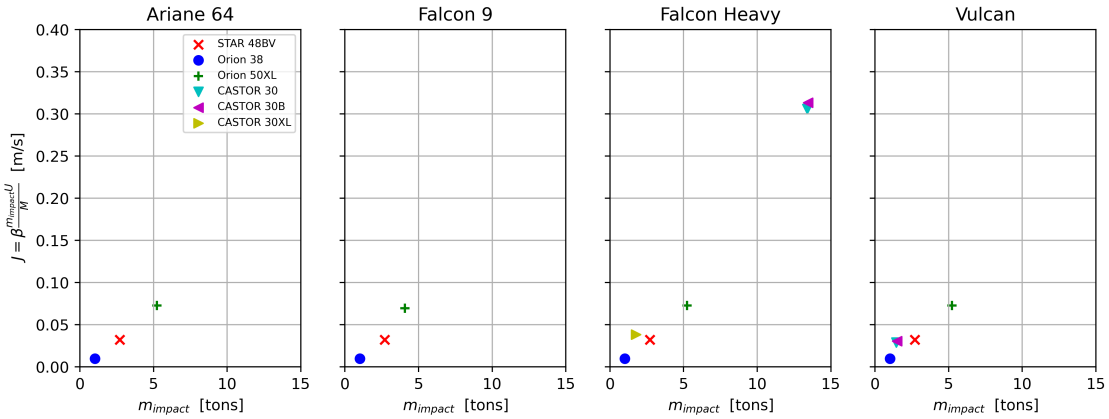

Figure 6.17: The velocity change given to the asteroid J as a function of impact mass for the solid kick stages, used to depart from a GTO around Earth to the reference asteroid, grouped by launch vehicle.

Table 6.8: The results for ID7, departing with a solid kick motor from a GTO. Only the Falcon Heavy launcher is capable of launching all six kick stages to an optimal orbit.

Solid motor	**Deflection** J [m/s]	**Impact efficiency** β [-]	**Departure date** [DD-MM-YYYY]	**Time of flight** TOF [days]
STAR 48BV	0.032	3.991	08-03-2027	583
Orion 38	0.010	3.192	08-03-2027	583
Orion 50XL	0.073	4.665	08-03-2027	583
CASTOR 30	0.306	6.250	08-03-2027	564
CASTOR 30B	0.313	6.284	08-03-2027	552
CASTOR 30XL	0.038	4.238	08-03-2027	177

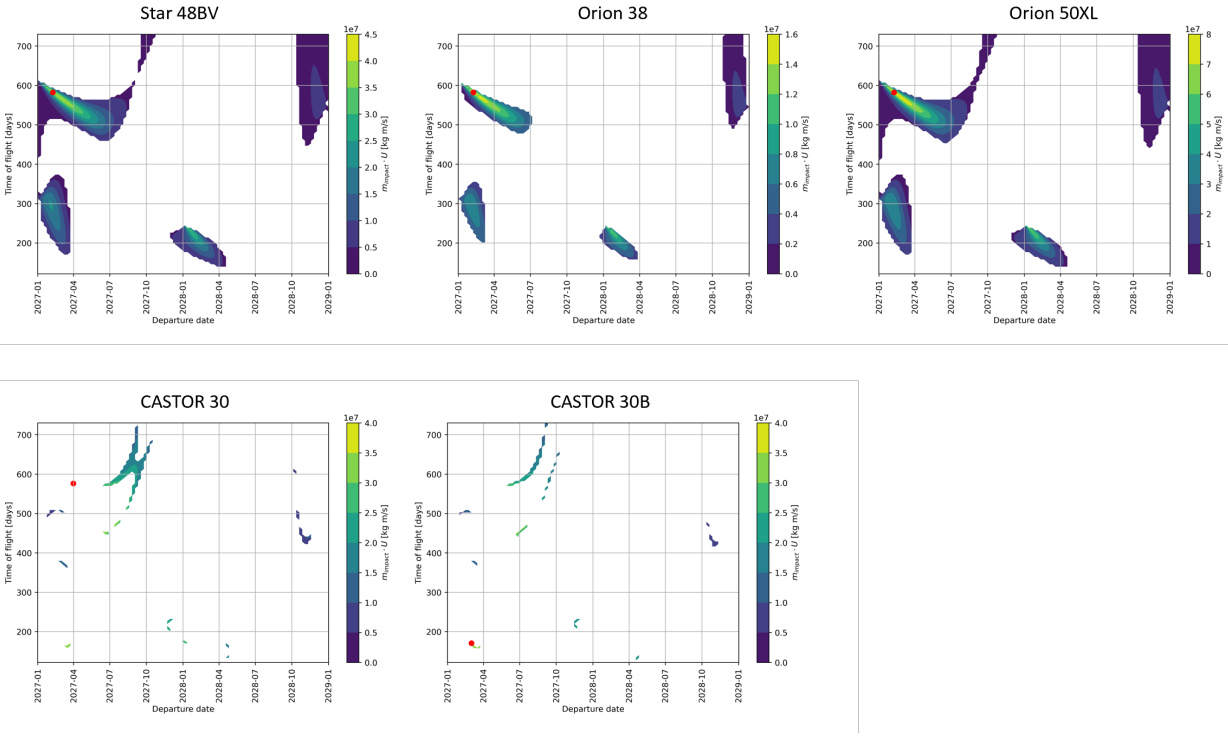

Figure 6.18: For the Vulcan launch vehicle, the departure opportunities and the resulting momentum at asteroid impact is different for each solid motor option. For the largest motor, the Castor 30XL, the plot is missing because the launch vehicle is not able to deliver a spacecraft equipped with such a motor to a GTO.

6.3. Comparison

Since all the design options were presented separately in the previous section, it is useful to compile the results across launch vehicles to see the performance differences regardless of launch vehicle capability.

Figure 6.19 compiles the results for the different configurations in the same plot, grouped by launch vehicle. The first row shows the option with bi-propellant propulsion, departing from a circular parking orbit or a GTO. The second row is the low-thrust trajectory, with results for different number of allowed revolutions of the transfer trajectory. The second row is therefore the same as Figure 6.15, but in comparison to the other configurations. The third and fourth row are the performance of a kinetic impactor, which departs with a solid kick stage from a circular orbit or GTO.

When looking at a single column of Figure 6.19, the most performant option given a specific launch vehicle can be determined. For Ariane 64, the first column, it can be seen that a directly inserted assembled impactor scores the highest. For Falcon 9, a direct insertion is not possible, so a circular orbit with a bipropellant propulsion system is giving the highest J. In the case of Falcon Heavy, with a very high mass capability to LEO, the same option comes out on top. The situation for the Vulcan rocket is similar to Ariane, where the direct insertion of an assembled impactor gives the largest J. In comparison to the direct insertion and bi-propellant departure, all other options show a consistently lower performance by almost one order of magnitude.

6.4. Monte Carlo Analysis

The model to estimate the deflection performance J depends on the asteroid target. Crucially, the energy required for the spacecraft to go on an interception trajectory and the impact speed depends on the specific orbit geometry and the relative positions between Earth, the spacecraft and the asteroid. The asteroid orbit is the single largest influence on the mission and it is therefore required to quantify the performance for a range of targets. In the previous section, a single reference asteroid was analysed, which is helpful in determining the difference that the launch vehicle makes and to demonstrate the method for determining the trajectory with the highest impulse. The same method is now used on a population of asteroids.

The method is tested on a population of real asteroids taken from the Minor Planet Center (MPC) Orbit Catalog. The ephemerides database is available online [47]. A random number generator is used to select an asteroid from the database and the orbit is determined as detailed in Chapter 4. The method ensures that the asteroid is on an interception trajectory with Earth. As an example, 50 randomly drawn asteroid orbits are shown in Figure 6.20.

By bootstrapping the population, which means drawing random samples with replacement from the catalog, which is comprised of 3134 asteroids with an absolute magnitude H between 21.2 and 23, corresponding to a size of about 150m in diameter, the deflection performance of the different configurations is evaluated. The asteroids are conveniently sampled from the available and observed asteroids. The population is biased because only observed asteroids are in the catalog. Only Apollo and Aten asteroids are used in the sampling, because they cross the Earth's path. Out of the two, Apollo-type asteroids, with a semi-major axis larger than 1 AU, are more numerous in the catalog because they can be better detected from Earth. Atens orbits are mostly inferior to Earths orbit, and are therefore harder to observe due to the solar glare. The Sun's brightness overwhelms the reflected light from the asteroid and makes it difficult to observe the Atens, resulting in a sampling bias of the asteroid population.

The deflection performance as a function of asteroid target is calculated for each of the configurations. Starting with ID1 to ID4, the results can be seen in Figure 6.21. The point cloud is generated for a sample size of 500 asteroids. The mean impact mass and J is indicated by a crosshair.

The deflection performance of ID5, the low-thrust electric propulsion spiral, is shown in Figure 6.22. The indication of the mean velocity change shows that, on average, a transfer with at least 1 revolution gives the highest deflection.

For the solid kick stages, the deflection is evaluated with the available commercial kick stages. First, for the departure from a circular parking orbit in Figure 6.23 and from an elliptical GTO in Figure 6.24. For some kick stages, the launch vehicle is not capable of lifting them into the required parking orbit.

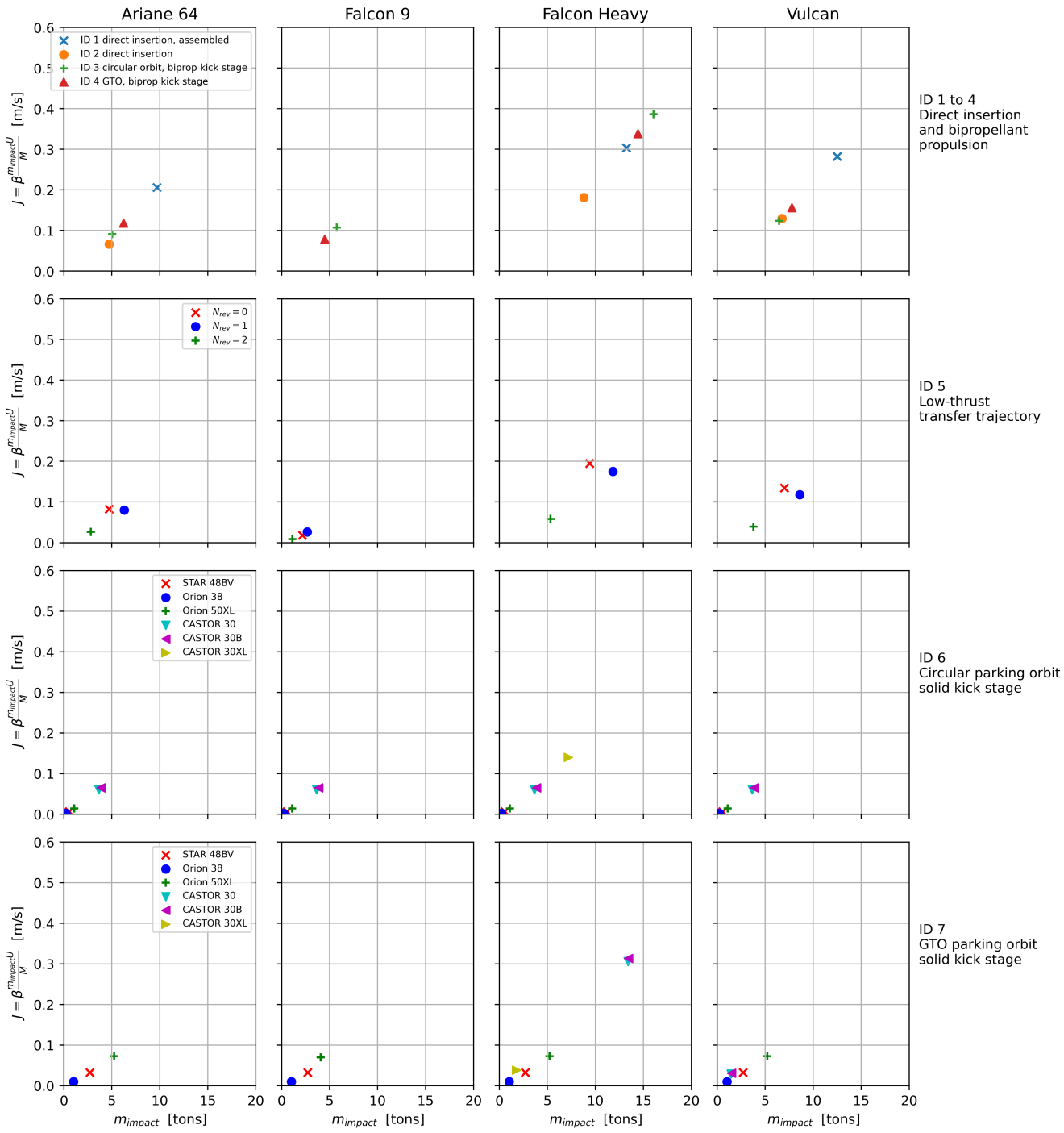

Figure 6.19: A compilation of the results for J as a function of impact mass for the different mission configurations.

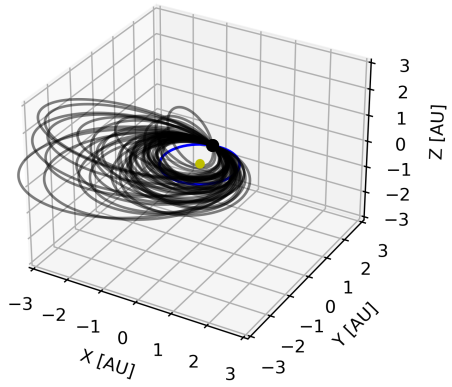

Figure 6.20: An exemplary population of 50 randomly drawn asteroids from the Minor Planet Center Catalog. The asteroids intercept Earth at a common point and are used as input for the calculation of the deflection performance. The Earth's orbit is shown in blue.

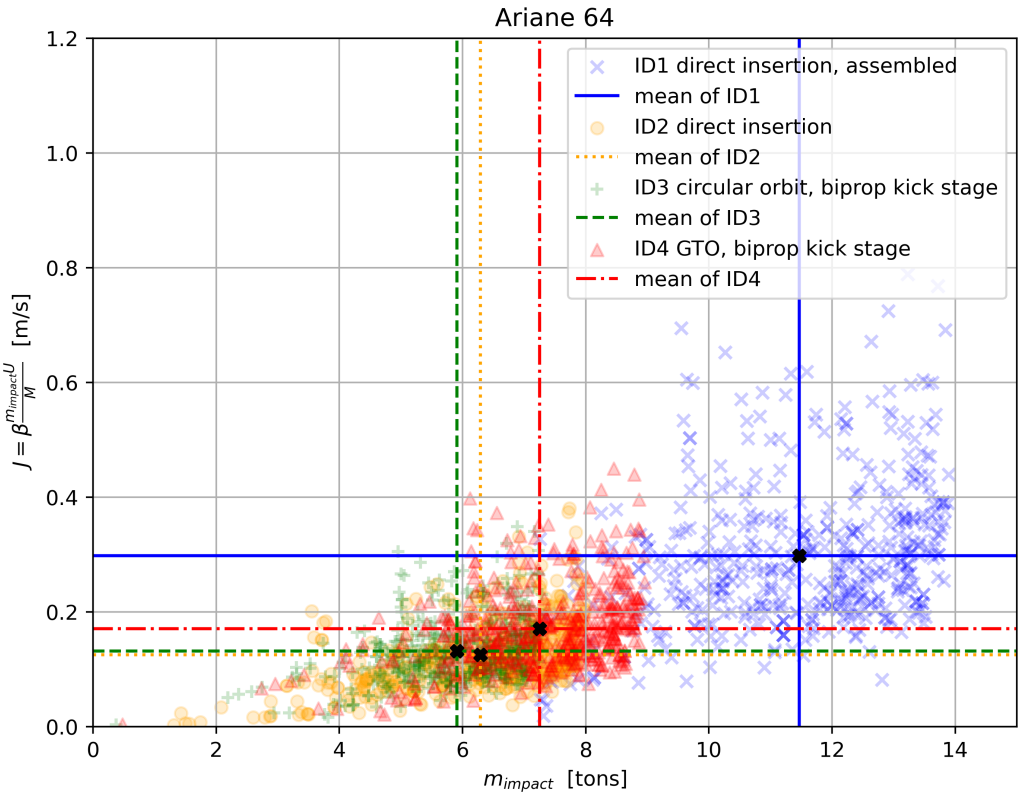

Figure 6.21: For the configurations ID1 to ID4, the velocity change given to the asteroid is calculated for a random sample of 500 potentially hazardous near-Earth asteroids. The black marker in the center of the cross hair indicates the mean J and m_{impact}

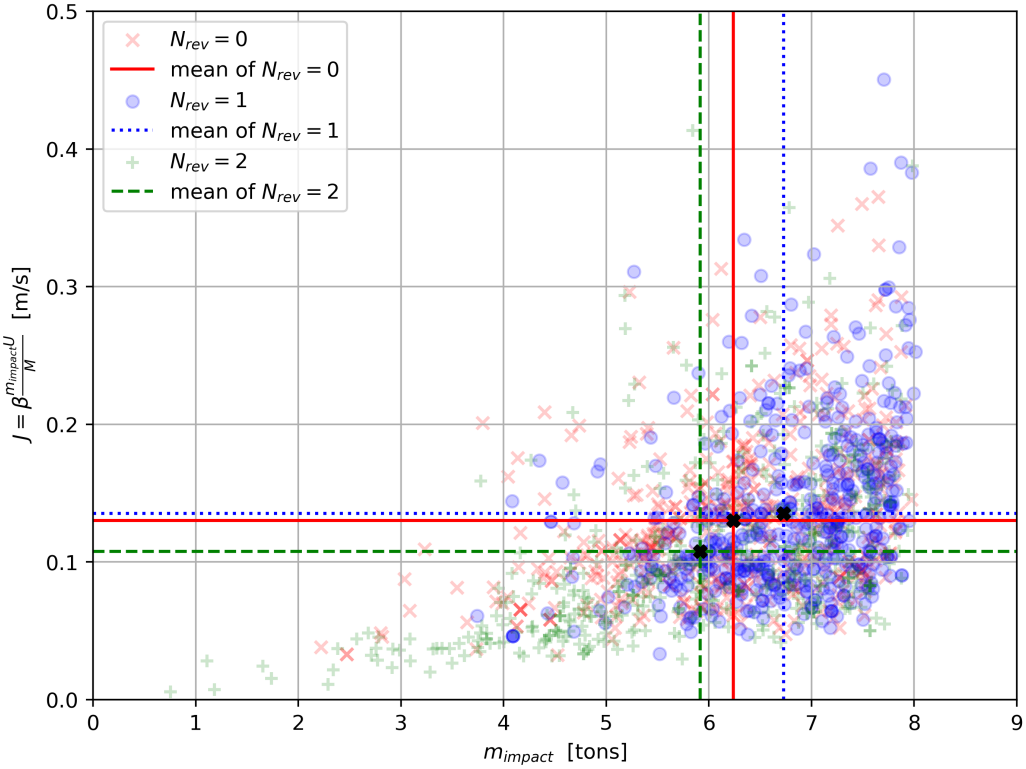

Figure 6.22: The deflection performance of ID5 with a low-thrust transfer trajectory with different numbers of allowed revolutions. The point cloud shows the deflection performance for a sample of 500 asteroids, and the mean impact mass and J are indicated.

For the circular parking orbit, the CASTOR 30XL is too heavy for Ariane 64. In the case of the GTO, the CASTOR 30XL is omitted from the graph because it cannot be launched to a 500 km parking orbit by an Ariane.

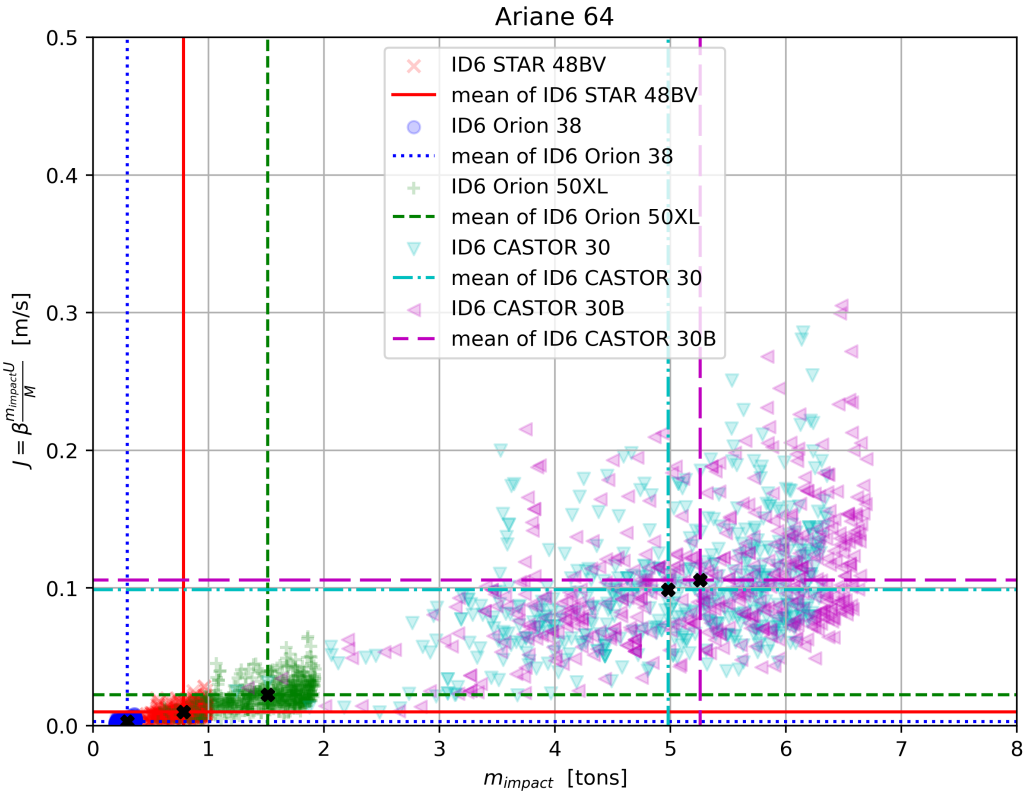

Figure 6.23: For the configuration ID 6 the spacecraft is brought into a circular parking orbit and departs with a solid kick motor. The mean impact mass and deflection is indicated by a crosshair.

The results are compiled for better comparability in a single plot with common axes in Figure 6.25. In order to make tangible statements about the results, it is useful to display the deflection performance as a boxplot for each of the mission configuration, as shown in Figure 6.26. For the low-thrust trajectory, the option with at least 1 revolution is selected because it has the best performance on average, compared to $N_{rev} = 0$ and $N_{rev} = 2$. In the case of ID6, the Castor 30B solid motor yields the best performance and is used to represent ID6 in the boxplot. Similarly, the Orion 50XL motor is selected for ID7.

The boxplot is graphically representing the data using the five number summary. The horizontal middle line is the median value, and the box extends from the first quartile to the third quartile. The first quartile represents the point where 25% of the data is below this point, while the third quartile has 75% of the date under it. The distance between the first and third quartile, the interqartile range (IQR), is used to define the length of the whisker. Measured from the upper third quartile, the whisker is drawn up to the largest data point that falls within a distance of 1.5 times the IQR. The lower whisker is drawn to the lowest data point within 1.5 times the IQR from the first quartile. Outside of this range, the outliers are displayed as scatter points.

For the same seven configurations, with a sample size of $n = 500$ as in the boxplot, the sample mean (Equation (6.1)), sample variance (Equation (6.2)) and confidence interval are reported in Table 6.9.

$$\bar{J} = \frac{1}{n} \sum_{i=1}^{n} J_i \tag{6.1}$$

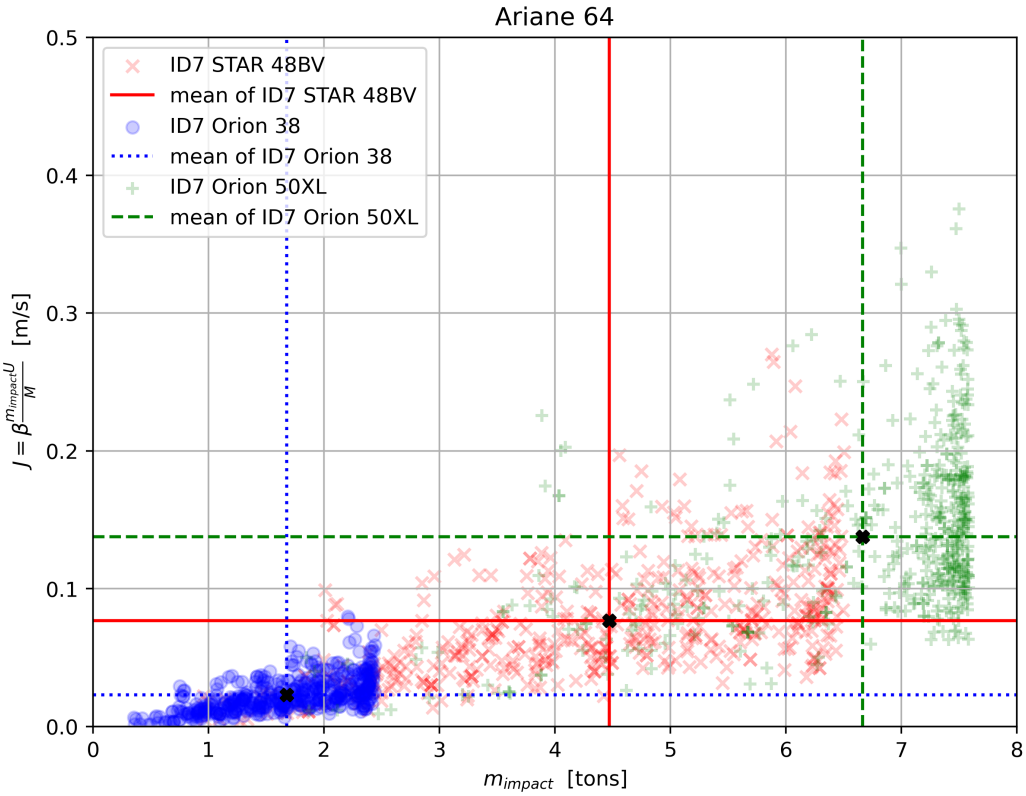

Figure 6.24: The deflection performance for a combination of an elliptical parking orbit and a solid kick motor for Earth departure for a population of 500 randomly drawn asteroids.

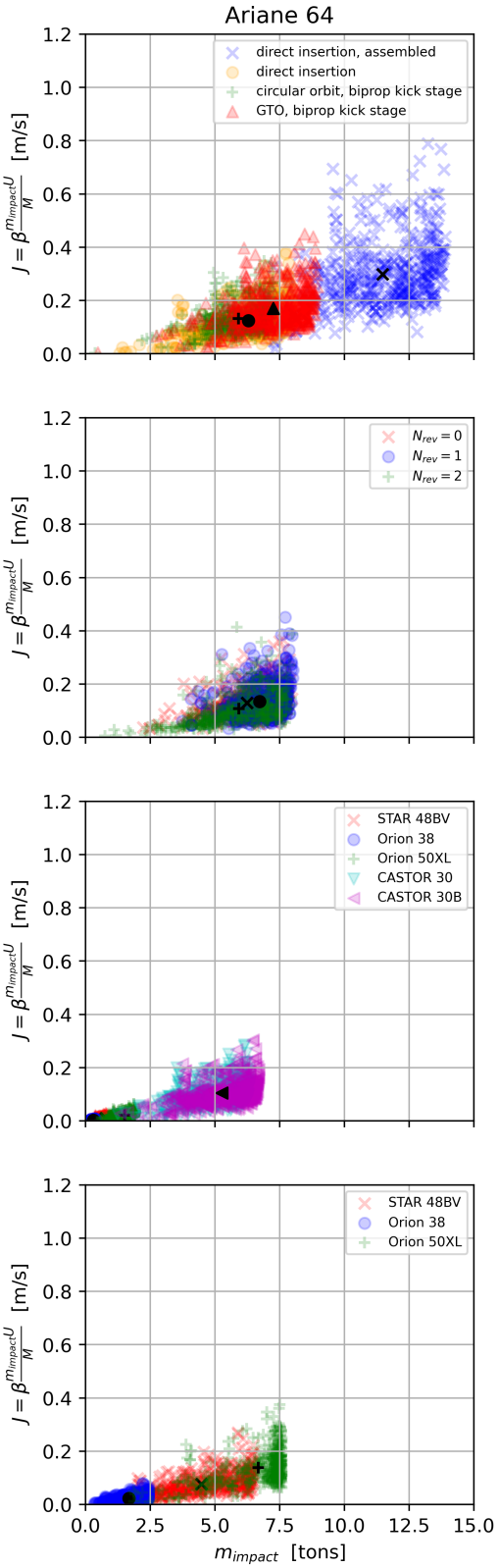

ID1 - ID4
Direct insertion
and bipropellant
propulsion

ID 5
Low-thrust
transfer trajectory

ID 6
Circular parking orbit
solid kick stage

ID 7
GTO parking orbit
solid kick stage

Figure 6.25: A comparison between the deflection evaluated for a kinetic impactor with varying mission architecture, evaluated for 500 randomly selected asteroids with a size of around 150m in diameter.

$$s^2 = \frac{1}{n}\sum_{i=1}^{n} |J_i - \bar{J}|^2 \tag{6.2}$$

The confidence interval is then constructed as

$$\left[\bar{J} - z_{(1-\frac{\alpha}{2})}\frac{s}{\sqrt{n}}; \bar{J} + z_{(1-\frac{\alpha}{2})}\frac{s}{\sqrt{n}}\right]. \tag{6.3}$$

With a significance level of $\alpha = 0.01$, the probability of the standard normal distribution is $z_{(1-\frac{\alpha}{2})} = z_{0.995} = 2.5758$. With a probability of 99%, the velocity given to the asteroid, denoted by the deflection performance J, is in the range of 0.284 m/s and 0.313 m/s for ID1. As obvious from the boxplot in Figure 6.26, the assembled impactor with direct insertion is the best performing option for the Ariane 64 launch vehicle.

In order to make the results of the Monte-Carlo analysis comparable, a single launch vehicle was selected to generate the results for a population of asteroids. Especially in the case of a super heavy-lift launch vehicle, represented by Falcon Heavy, the payload capability to a low-Earth orbit is significantly higher, resulting in a different distribution of the deflection performance, as suggested by Figure 6.19. As shown in Figure 6.27, the results are as expected, with ID3 having the highest average deflection speed.

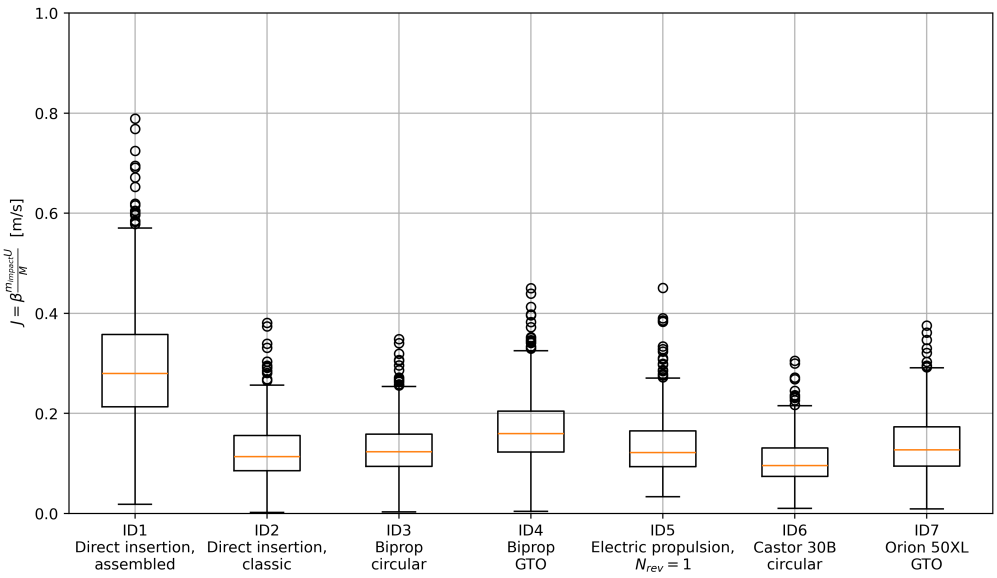

Figure 6.26: The boxplot shows the statistical distribution of the deflection performance for each of the proposed configurations, with a sample size of 500 asteroids from the MPC database.

6.4.1. Asteroid normal distribution

As an additional investigation, the asteroid population is modelled as a multivariate normal distribution of the orbital elements a, e, i. The results are included in Appendix C. The three orbital elements have a real distribution as shown in the first row of Figure C.1. The distribution is normalized to a probability density function (PDF) with a density of unity, shown in the second row. By calculating the mean and covariance of the real distribution, a normal distribution probability density function can be plotted over it.

The numpy package [22] is used to set up a multivariate normal distribution from the data for each of the orbital elements. Then, samples can be drawn and the distribution can be compared to the original data set, which is shown in the last row of Figure C.1, with the same number of samples.

Table 6.9: The 99% confidence interval for the deflection performance as tested on 500 asteroids for each of the configurations, denoted by their ID.

ID	Sample mean $\bar{J}$ [m/s]	Sample variance s^2 [m^2/s^2]	Lower bound CI_l [m/s]	Upper bound CI_u [m/s]	Comment
1	0.298	0.015	0.284	0.313	
2	0.125	0.004	0.118	0.132	
3	0.132	0.003	0.126	0.138	
4	0.171	0.005	0.163	0.179	
5	0.135	0.004	0.128	0.142	$N_{rev} = 1$
6	0.106	0.002	0.100	0.111	Castor 30B
7	0.138	0.004	0.131	0.145	Orion 50XL

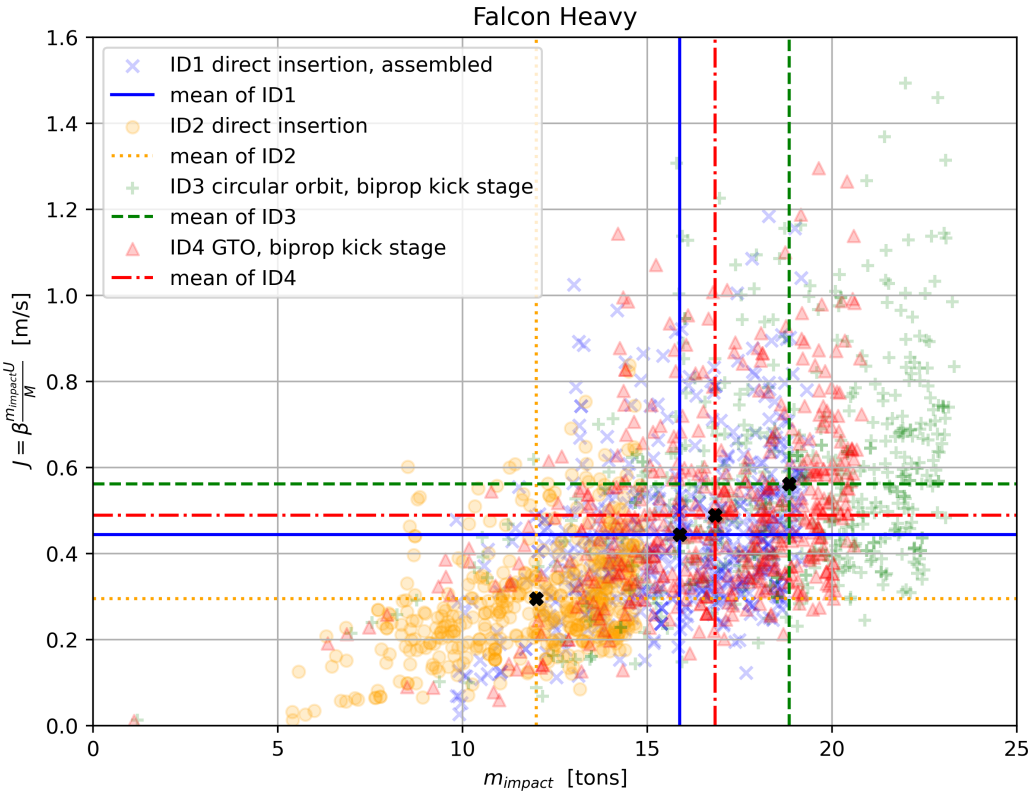

Figure 6.27: The deflection performance of configuration ID1 to ID4 for 500 asteroid samples for the Falcon Heavy launch vehicle.

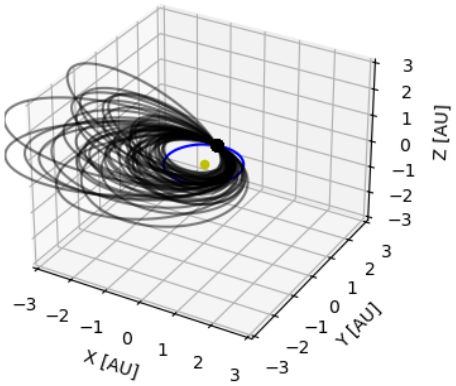

Figure 6.28: An orbit population of 50 asteroids, drawn from a multivariate normal distribution.

The same filtering is applied to the asteroid catalog, with the condition of Earth-crossing near-Earth and a size of approximately 150m in diameter, which translates to an absolute magnitude H between 21.2 and 23.0. Going forward, the orbital elements a, e, i are used to set up a Keplerian orbit that intercepts Earth at a certain date in the future. This results in an asteroid orbit that can be used further in the model to estimate the deflection performance. A visualization of the generated target asteroids is given in Figure 6.28, for an exemplary sample size of 50. The orbits all intercept in one point, which is the position of the orbit at the time of impact with Earth. Such a set of orbits is now used for a Monte Carlo analysis of the deflection performance, to check the analyse the effect of the orbital parameters.

Now the results can be generated for larger sample sizes, for example 500 asteroid targets are feasible. To make the results comparable, Ariane 64 was selected as a launch vehicle. The influence of the asteroid orbit can be seen in the result for the figure of merit. The results are organised in the same way as the compilation of the reference case in Figure 6.19, with the same colors and markers corresponding to the same cases. The the bi-propellant departure and the direct insertion the results are shown in Figure C.2 through Figure C.5. Table 6.10 documents the mean deflection and the confidence intervals for each configuration.

Table 6.10: The sample properties of the deflection performance for 500 randomly generated asteroid from a multivariate normal distribution. The confidence interval CI is given for a confidence level of 0.99 and three significant digits.

ID	Sample mean $\bar{J}$ [m/s]	Sample variance s^2 [m^2/s^2]	Lower bound CI_l [m/s]	Upper bound CI_u [m/s]	Comment
1	0.328	0.012	0.315	0.341	
2	0.142	0.003	0.135	0.148	
3	0.144	0.002	0.139	0.150	
4	0.187	0.004	0.180	0.194	
5	0.149	0.003	0.142	0.155	$N_{rev} = 1$
6	0.118	0.002	0.112	0.123	Castor 30B
7	0.153	0.004	0.146	0.16	Orion 50XL

6.5. Conclusion of the performance results

From the compilation of the results in Figure 6.19, it can concluded that the performance of the kinetic impactor depends on the launch vehicle, and the selection of the most performant option can be done based on the classification of the launch vehicle.

For a medium-lift launch vehicle, specifically the Falcon 9, the direct insertion of a kinetic impactor into a transfer trajectory to the reference orbit is not possible. In that case, a spacecraft departing from a circular parking orbit with a liquid-bipropellant system is giving the highest performance.

For a heavy-lift launch vehicle, like Ariane 64 and Vulcan Centaur VC6, the direct insertion is possible. The assembled impactor, because of its mass advantage, outperforms the classic impactor. In the special case of the Vulcan rocket, it is able to lift heavy solid rocket motors for Earth departure, but the constraints on launch mass and minimum spacecraft mass limit the available launch opportunities. The feasible launch opportunities are less optimal in terms of impact momentum, such that the higher performing solid motors do not translate to a higher deflection performance.

For a super heavy-lift launch vehicle, Falcon Heavy as an example, the direct insertion of an assembled impactor is possible. It can be observed however that, due to the high payload capacity to LEO, a bi-propellant spacecraft, departing from a circular parking orbit, results in the highest deflection performance. Even for the Falcon Heavy the limitation of launch mass is evident, because a spacecraft with the heaviest commercial solid motor, the Castor 30XL, cannot embark on the trajectory that maximizes the momentum.

When doing a cross-comparison between the configurations, disregarding the launch vehicle, some clear trends can be identified. Overall, the departure from a parking orbit with a bi-propellant kick stage and a direct insertion gives a higher deflection performance than the other commissioning options. A pattern in the impact mass can be seen, where the solution which is allowed a full revolution gives the highest momentum, followed by $N_{rev} = 0$ and $N_{rev} = 2$.

The Monte-Carlo analysis strengthens the conclusions. By employing the same method on multiple potentially hazardous asteroids, a statement can be made about the configuration that is most likely to give the best deflection performance. In the case of the European launcher Ariane 64, the results clearly show, that an assembled impactor, designated by ID1, is the superior option. The 99% confidence interval for the deflection is between 0.284 m/s and 0.313 m/s, for an asteroid of 150m in diameter and an assumed mass of $5{\cdot}10^9$ kg.

6.6. Discussion of the method

The methods used to arrive at the results and the conclusions do not come without caveats. This section will go over the main assumptions and critically reflect on their influence.

First of, convenience sampling was applied at different points throughout the development of the method. An instance is the selection of launch vehicles, with a focus on data availablity. From a European perspective, it is deemed interesting to include the Ariane 64 vehicle, because of its availability and good relations between the launch provider and European prime contractors. The Falcon rockets have been proven to be reliable, also for European interplanetary missions, and can be a cost effective alternative. The Vulcan rocket is relatively new, but the manufacturer has a long history of launcher families such as Atlas and Delta. Countries like India and China have medium to super heavy-lift launch vehicles, but these were disregarded for the thesis.

A similar sampling was applied to the selection of analysed solid motors. The selection criteria are once again commercial availability and data availablity. The selected kick stages cover a range of performances and weight classes. For the bi-propellant system, a selection had to be made, striking a balance between reliability and performance. The de-facto standard for in-space propulsion, a hypergolic system with MMH/MON as propellant is chosen.

In terms of methods, the chosen theoretical framework consists of often-used preliminary design tools. The Lambert targeter, and its implementation in the python package Pykep [28], is used to find the transfer trajectory. The assumptions are that the orbits of Earth, the asteroid and the transfer are Keplerian, and the interaction between the bodies is ignored. The planetary departure is based on the

assumption that the velocity change is supplied by an impulsive shot, so the acceleration phase and associated gravity losses are not modelled. Furthermore, the patched conics approach is chosen, so the departure starts with an hyperbolic orbit and is patched to an elliptical transfer orbit at the border of the sphere of influence.

For the low-thrust trajectory, which is an interesting alternative to the ballistic elliptical transfer, a shape-based method with exponential sinusoids is chosen. Because the shape of the transfer is modelled by a simple function, the parameters of the transfer can be determined with low computational effort. Another advantage is that a Lambert formulation for the exponential sinusoid is implemented, based on Izzo [29], which has the same functionality as the regular ballistic Lambert targeter.

The overall setup ensures a fair comparison between the configurations. Essentially, only the target orbit, a range of departure dates and a range of allowable time of flight is given as an input. Constraints are the launch vehicle, propulsion system performance (for low-thrust, solid motors and bi-liquid) and the physical properties of the asteroid.

An important step in the evaluation of the deflection performance is finding the momentum enhancement factor β. The chosen implementation is based on scaling laws and accounts for an oblique impact [40]. The existing model was extended with the influence of the angle of an ejecta mass element when it escapes the asteroid's gravitational influence. The scaling laws are based on a physical formulation of the point source assumption, meaning that the energy of the impact is released from a single point, which is valid because the length scale of the impact event is much larger than the impactor itself. Furthermore, the scaling laws are based on constants derived from impact simulations and experiments. The resulting β values are an indication and require further simulation with numerical codes.

In summary, the chosen methods are heuristic but yield comparable results to make an informed trade-off between launch vehicles, deployment options and the resulting deflection performance. The conclusions from this chapter are used for a trade-off in Chapter 7.

7

Spacecraft

The results presented in Chapter 6 are used to inform a trade-off between the methods in Section 7.1.The three segments of the mission are discussed, which are the ground segment (Section 7.2), the launcher segment (Section 7.3) and the space segment (Section 7.4).

7.1. Concept Trade-Off

As discussed in Section 6.5, the deflection performance of the kinetic impactor differs for the launch vehicle categories. For a heavy-lift launch vehicle, the likes of Ariane 64 and Vulcan VC6, the highest performance is achieved when the impactor is delivered to the interplanetary trajectory by the launch vehicle and the second stage is kept attached to the spacecraft. The performance is a criterion of the trade-off, with other secondary parameters discussed in the following.

The first aspect is the operational risk of the concept. The capability of the concept to adapt to unforeseen issues or changes in the mission is important to achieve a successful deflection mission. Another criterion is the complexity, which is divided into mission complexity and system complexity. The mission complexity can be described as how involved the steps during the operational mission are. For example, performing multiple burns and stage separations, or achieving high accuracy orbit control is considered as complex items that drive the design process and cost. The system complexity concerns the spacecraft itself, and how complex the concepts are in relation to each other.

The cost criterion is an important metric in order compare the financial commitment necessary to implement the mission and is of high importance for the customer. Lastly, the overall technology readiness of the concept is an indication of the development effort and is also related to cost. A high technology readiness is preferred to reduce the risk of delays and failure of the mission.

A relative comparison between the concepts is done, with the scores being ”+1” meaning good, ’0’ being neutral and ’-1’ indicating worse. The sum of these options gives a final score, which is an indication of a favourable concept. The trade-off table is shown in Figure 7.1.

First of all, the concepts are graded on their operational risk. A circular parking orbit, like ID3 and ID5, is one of the aspects of the mission that result in lower risk. The orbit allows the operators to perform system checks in LEO and then depart from any position along the orbit with the same orbital energy. In contrast to that, an elliptical orbit like a GTO only gives an advantage in reduced velocity change for planetary departure when the orbital velocity is high. So only close to the perigee of the orbit a mass effective departure can be achieved. For direct insertion, the spacecraft is brought on the interplanetary trajectory by the spacecraft and can only use trajectory correction maneuvers to marginally adjust the transfer. Therefore the circular parking orbit with bi-propellant propulsion system has the highest flexibility, not only because of the parking orbit but also because of the possibility to reignite the propulsion system, as opposed to solid motors. The operational risk is reduced because of more possibilities for corrective actions. The electric low-thrust propulsion spacecraft is flexible in the sense that the propulsion system can be used for larger trajectory adjustments.

The mission complexity can be judged for each of the concepts, starting with the the direct insertion options. For both the classic impactor and the assembled version, the mission complexity is moderate. The launch vehicle does most of the work and the spacecraft itself is cruising to the target. The complex part is ensuring the injection inaccuracies are corrected and the spacecraft is precision-guided to the target. For the two bi-propellant options, the mission complexity is higher due to the fact that they are commissioned to a parking orbit first and then depart from Earth.

Criterion \ Concept	Direct insertion, assembled	Direct insertion	circular orbit, biprop	GTO, biprop	EP, direct insertion	circular orbit, solid	GTO, solid
	ID 1	**ID 2**	**ID 3**	**ID 4**	**ID 5**	**ID 6**	**ID 7**
Operational risk	-	-	+	0	0	+	0
System complexity	+	+	-	-	-	0	0
Performance	+	0	0	0	0	0	0
Cost	0	0	0	0	-	+	+
Technology readiness	0	+	+	+	0	0	0
Score	2	1	1	0	-2	2	1

Figure 7.1: The concept trade-off including secondary parameters to determine a recommendation for the best spacecraft concept.

Out of all the options, ID1 offers the best performance and is deemed the winner of the trade-off. Therefore, ID1 is the configuration that is treated in more detail in the following sections.

First of all, the context diagram for the mission, called ”Astraea”, is shown in Figure 7.2. The mission is divided into three segments, the space segment, the ground segment and the launch segment. The ground station is receiving telemetry data and sends telecommands. It exchanges data with the Mission Control and Operations. The launcher shares the launcher-spacecraft interface with Astraea. In the case of the assembled impactor, the launch vehicle second stage is shared between the space segment and the launch segment. The interfaces between the spacecraft and the launcher run through the second stage.

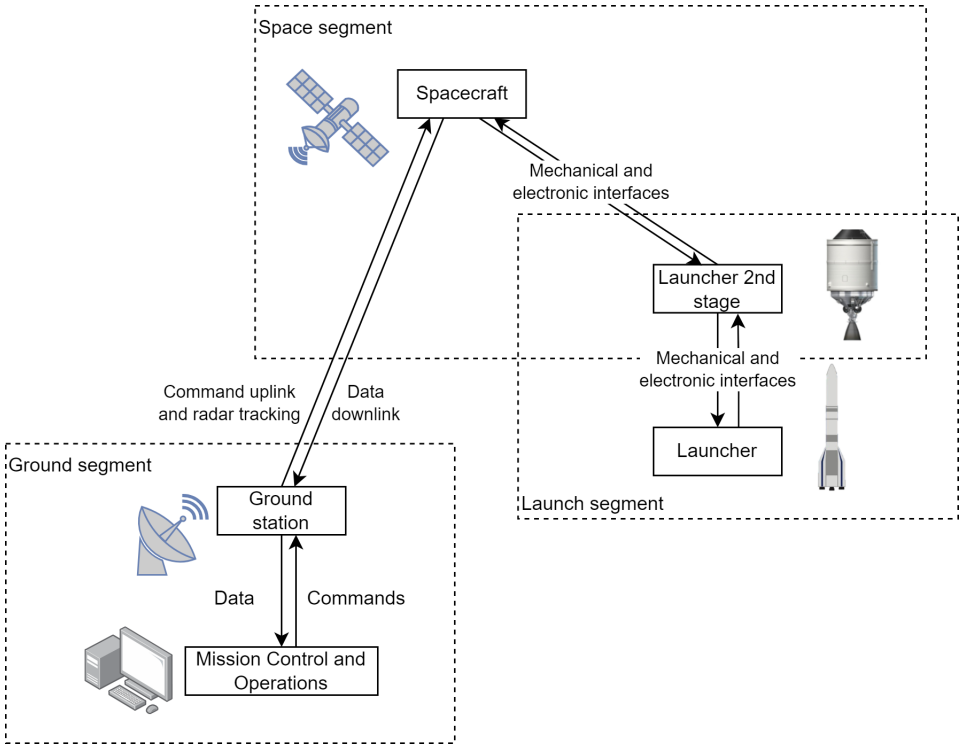

Figure 7.2: The context diagram of the ”Astraea” space mission.

The three segments of the mission are described in more detail in the following sections. For the space

segment, the subsystems of the spacecraft are also discussed.

7.2. Ground segment

The main functions of the ground segment are dealing with uplink and downlink data, and localization of the spacecraft using radar tracking.

The ground station provides a radio interface between the spacecraft and the operators. The data is modulated onto a carrier signal and sent to the spacecraft. The ground station receives housekeeping data, diagnostics and image data on the downlink.

A method for precise localization of the spacecraft is Delta Differential One-way Ranging (DDOR), which is recommended by the DART team to be used on upcoming interplanetary missions [4]. ”One-way” refers to the fact that only the signal downlink from the spacecraft is used for tracking. Two antennas on the ground, which are widely spaced apart, receive the signal. “One-way” means that only the signal downlink from the spacecraft is used. “Differential” means that the path length difference of the signal can be calculated from the difference in time of arrival at the ground stations, such that the position of the spacecraft can be triangulated.

To account for the effects of atmospheric errors, clock offset between the ground stations, instrumental inaccuracies and others, a reference radio source is measured. The reference source is usually a catalogued quasar, for which the angular position is very well known. By measuring the position of the spacecraft, and then right after calibrating the measurement with the reference source, the errors can be removed. “Delta” means comparing the measurements of the reference source and the target spacecraft. DDOR can be performed by ESA ESTRACK [30]. A schematic of the method is shown in Figure 7.3.

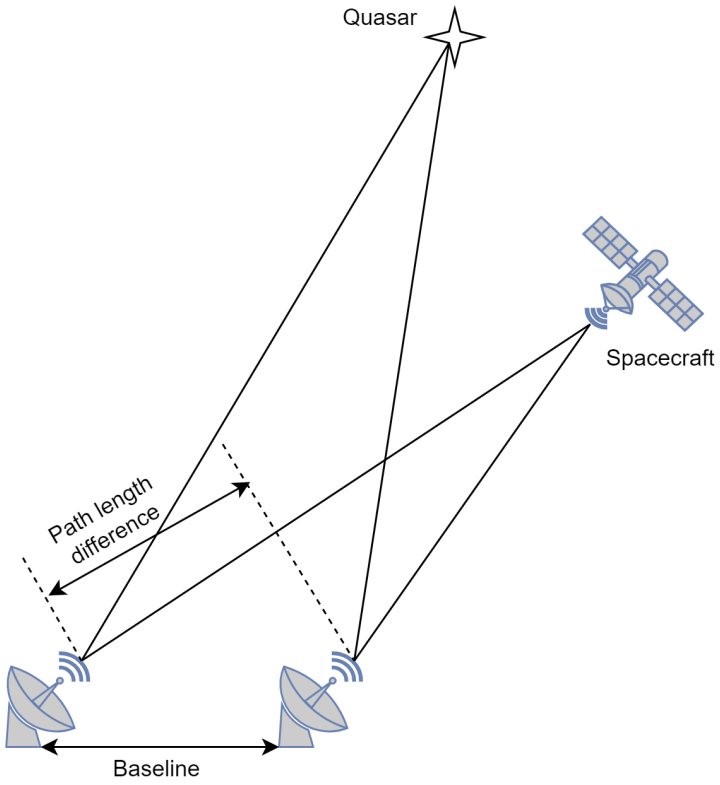

Figure 7.3: The delta differential one-way ranging method measures the path length difference between between a signal received by two ground stations. A quasar is used as a reference source to reduce the position error.

Some caveats of the method are that two antennas have to be available and need line of sight with the spacecraft. Furthermore, operation is costly and time-consuming. However, the accurate measure-

ments are necessary to make the mission a success, as demonstrated by DART [4].

GROUND-1 The ground operations system shall be able to exploit recurring DDOR measurements.

GROUND-2 The ground operations system shall determine orbit solutions of the spacecraft during the mission duration.

GROUND-3 The ground operations systems shall process downlinked images from the spacecraft.

GROUND-4 The ground operations systems shall process uplink telemetry and downlink telecommand data.

7.3. Launcher segment

The launch vehicle second stage shared by the launch segment and the space segment. In order to keep the complexity of the assembled impactor at a manageable level, the interfaces between the spacecraft and the upper stage shall be kept to a minimum. A possible challenge, which was also experienced during the Moon cratering mission LCROSS [46], are propellant or gas leaks in the upper stage during the cruise phase. The leaks have to be accounted for in the design of the attitude control system and the expected magnitude of a resulting disturbance torque can be estimated.

A passivation procedure for the upper stage has to be derived, in order to minimize disturbance torques and reduce the risk of damage to the system. The controlled release of propellant is necessary to avoid larger leaks in the later stage of the cruise phase. Propellant release also reduces the risk of high-energy release or anexplosion of the upper stage. The passivation procedure has to be designed in conjunction with the AOCS to maintain attitude control.

STAGE-1 The launcher second stage shall be passivated at the beginning of the cruise phase.

7.4. Space segment

The space segment includes the spacecraft and the attached launcher second stage. The product tree of the spacecraft is shown in Figure 7.4. The product tree is split up by subsystems. Astraes features the standard subsystems for an interplanetary mission, with a special focus on Guidance, Navigation and Control (GNC), due to the fact that the objective is to hit a small asteroid target.

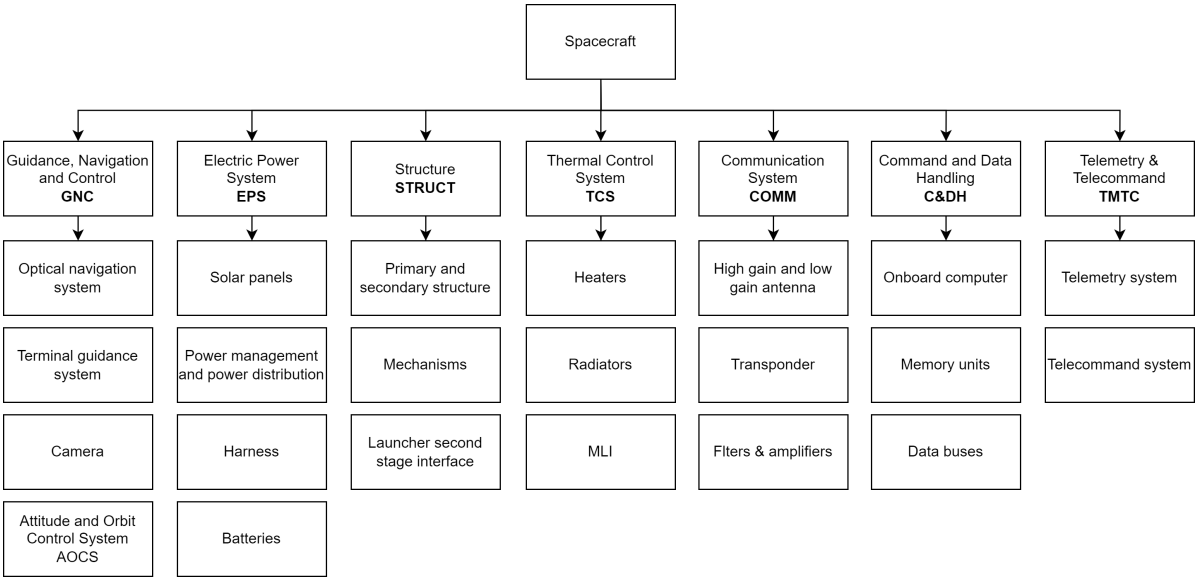

Figure 7.4: The product tree of the ”Astraea” kinetic impactor mission.

7.4.1. GNC

According to the European Cooperation for Space Standardization (ECSS), the term GNC is used when the navigation and control functions are performed on-board [14]. In general, GNC is a broader term that includes the Attitude and Orbit Control System (AOCS). A kinetic impactor mission is especially challenging for the GNC system. Inspired by the DART mission and its successful impact [12], the main challenges and components for GNC are described.

As indicated in the product tree (Figure 7.4), the main constituents of the GNC are the optical navigation system, the terminal guidance system, the camera and the AOCS. The optical navigation system, and especially the camera, serves multiple purposes, such as ground based optical navigation, centroiding for autonomous guidance and the characterization of the asteroid surface.

Ground based optical navigation means that, during the cruise phase, the camera is commanded from ground to take multiple long exposure images of the distant target, which can be used to improve the orbit solution determined from radar measurements. For terminal guidance, the cadence in which images are acquired is increased, in order to to update the guidance commands for the last hours of the mission before impact. A secondary priority is the scientific aspect of the images. The pictures of the surface can be used to characterize the impact site, in terms of topography, boulder location and the impact location with respect to the center of gravity of the asteroid.

An important requirement for the navigation system is the handover accuracy between the approach phase and the terminal phase. This requirement is defined as a circle projected on the B-plane of the asteroid. The circle defines the maximum deviation from the center of the target and is sketched in Figure 7.5. The circle defines the maximum deviation from the center of the target. The diameter of this circle shall be no larger than the orbit correction that the terminal guidance system can deliver. In the case of DART, the requirement was a circle of 15 km radius, with a desirement of 2 km [5]. The vector $\hat{S}$, also called the asymptote vector, is parallel to the incoming asymptote direction. The vector $\hat{R}$ is perpendicular to the orbital plane of the asteroid, with the vector $\hat{T}$ completing the right-handed coordinate system. The center of the coordinate system coincides with the center of the asteroid target.

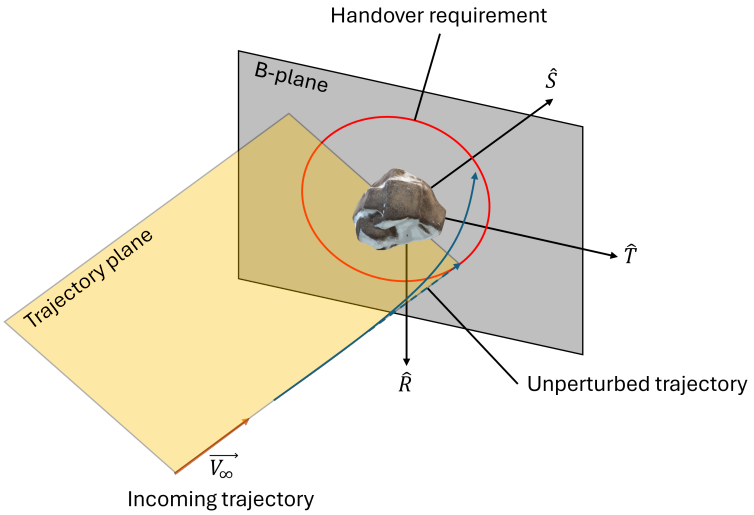

Figure 7.5: The B-plane of the asteroid and spacecraft approach situation, with the handover uncertainty indicated as a circle.

ONS-1 The ONS shall take long-exposure images of the target during the cruise phase.

ONS-2 The handover uncertainty from the cruise phase to the terminal phase shall be no larger than the maximum orbit adjustment deliverable by the Terminal Navigation System.

The Terminal Guidance System (TGS) is the system that takes over from the end of the cruise phase for the terminal phase right before impact. Autonomous guidance is necessary and was demonstrated during the DART mission [5].

TERMINAL-1 The TGS shall autonomously guide the spacecraft to impact on the asteroid

surface.

TERMINAL-2 The TGS shall be capable of diverting the asteroid orbit from the handover uncertainty to the center of the asteroid.

The terminal guidance system uses the optical telescope to capture images and derive guidance commands. The process for acquiring the images is given in Figure 7.6 and is inspired by the methods used on DART misson [5]. During image processing, the raw data is cropped into a suitable image format. A process called binning is applied to enhance the signal to noise ratio, where a certain number of pixels are combined. The navigation system takes the image data and applies a threshold to sort out other light sources which are not the target. Centroiding is applied, where an algorithm finds the center of the brightest pixels. After filtering and calculating the center of the target with respect to the spacecraft, the GNC system is issuing a suitable guidance command.

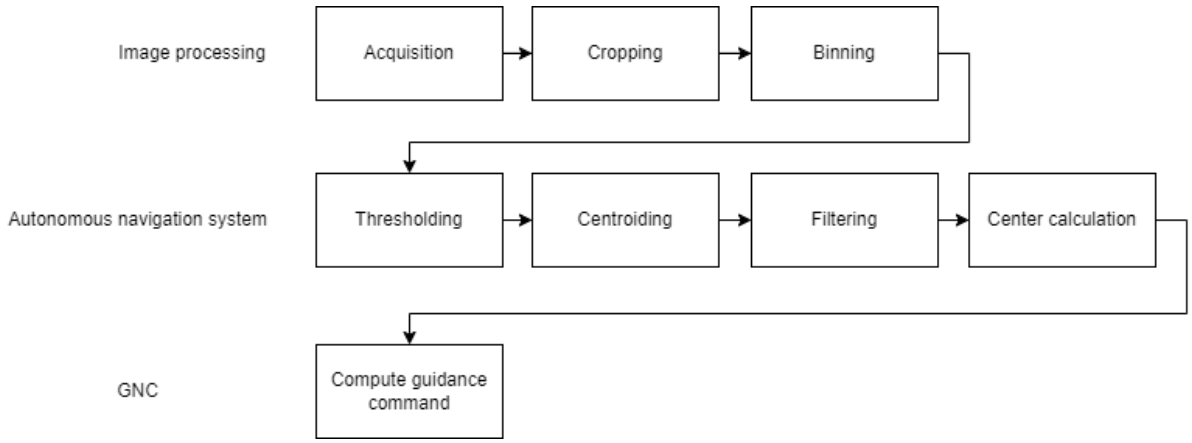

Figure 7.6: The image processing timeline for the terminal navigation system.

An important parameter of a representative telescope, based on the Didymos Reconnaissance and Asteroid Camera for OpNav (DRACO) [43], is the instantaneous field of view (IFOV) of a single detector element. The IFOV of the reference camera is 2.48 μrad, and the total array has a resolution of 2560 by 2160 pixels. The IFOV determines at what distance from the spacecraft the target is detectable. The optical telescope is a Ritchey-Chretien type, with a primary and secondary hyperbolic mirror and a single lense. The lense flattens the image onto the sensor array, which is a COTS component. For terminal guidance, a realistic cadence of image acquisition is every 5 seconds for full resolution and every 2 seconds for a binned image [43].

The high-level requirements for the camera are given in the following.

CAMERA-1 The camera shall be able to resolve the target asteroid before the beginning of the terminal navigation phase.

CAMERA-2 The camera shall take images in the visible light spectrum.

The Attitude and Orbit Control System (AOCS), is a subset of GNC and is comprised of sensors and actuators. Star trackers are generally used on spacecraft for absolute attitude measurements. For redundancy reasons, two separate units are selected. The star trackers capture images and compare them to a reference catalog of stars to infer attitude information. As a backup way of determning absolute attitude information, two sun sensors are selected.

For relative attitude measurements, an Inertial Measurement Unit (IMU) is required. The IMU combines accelerometers and a gyroscope. Linear accelerations are measured by the accelerometers, and the rotational accelerations are measured by the gyroscope, resulting in information for all 6 degrees of freedom. A fibre-optic gyroscope is selected for its high accuracy and reliability.

In terms of control actuators, the spacecraft shall feature control moment gyros, due to their high torque and fine control. For the assembled impactor, a high control torque is necessary due to the attached launcher stage, so control moment gyros are selected over reaction wheels. An external reaction

control system with monopropellant hydrazine thrusters and Helium as a pressurant is a traditional and well-proven choice. Due to the size of the spacecraft and its required agility in the terminal phase, a set of divert thrusters is proposed, with their thrust axis perpendicular to the spacecraft centerline. The thrusters need to be positioned such that, for the assembled impactor, the thruster plume does not interfere with the launcher second stage to avoid damage.

For the assembled impactor, special challenges are posed for attitude control. The position of the center of gravity of the assembled impactor is likely to be in the second stage, which causes stricter requirements for the control system. A higher control torque might be necessary to achieve the required rotational rate. Decoupling attitude and orbit control is an additional challenge for the assembled impactor.

AOCS-1 The AOCS shall provide full three axis control over the spacecraft.

AOCS-2 The AOCS shall feature divert thrusters to steer the spacecraft during the terminal phase.

AOCS-3 The reaction control thruster plumes shall not interfere with the second stage structure.

7.4.2. EPS

The electrical power system consists of solar panels for power generation, a power management and distribution unit, the cable harness and batteries for power storage. A solar panel and battery architecture is suitable for long-term interplanetary flight and ensures continuous power generation. Lithium-ion batteries have volumetric advantages over other types and are selected for Astraea.

EPS-1 The EPS shall supply electric power to all subsystems during the operational phase of the mission.

7.4.3. STRUCT

The structure of the spacecraft consists of a central tube hosting the monopropellant for the reaction control thrusters and the divert thrusters, as well as a composite overwrapped pressure vessel for the Helium pressurant. Four side panels are attached with mounting points for the subsystem units.

In order to maximize the impact mass, the spacecraft structure shall be manufactured such that it maxes out the payload capacity of the launch vehicle. Lightweight structures are therefore not absolutely necessary, depending on the distribution of the mass budget. The structure has a large influence on the overall mass of the system and can be easily adjusted. The inclusion of a dead weight as additional impact mass can be considered.

The spacecraft structure also includes a launch vehicle attachment that connects the second stage to the spacecraft bus. From a structural perspective, the highest loads occur during launch, so the design of the structural interface can be based on existing adapters.

STRUCT-1 The structure shall provide structural integrity and protection during all phases of the mission and all load cases.

STRUCT-2 The structure shall maximize the spacecraft mass within the payload constraints.

7.4.4. TCS

The thermal subsystem for the assembled impactor has to ensure that the components are kept within their thermal range. Usually, batteries are the most critical component because of their narrow operating range. The standard components of the TCS include heaters, radiators and Multi-Layer Insulation (MLI).

Special attention has to be paid to extra conduction paths through the adapter to the launcher second stage. The additional large surface area absorbs more heat which is conducted into the spacecraft. Similarly, additional view factors between the second stage and the spacecraft can increase radiative heat transfer.

TCS-1 The TCS shall maintain the temperature of the spacecraft components within their thermal range.

7.4.5. COMM, C&DH and TMTC

The communication subsystem includes a high gain antenna and a low gain antenna. For the majority of the data transfer, the high gain antenna is utilized. A high gain antenna usually has a smaller beamwidth and has to be pointed more accurately towards the ground station.

For redundancy and guaranteed communication when the pointing is not possible, a low gain antenna is selected. With a wide field of transmission, basic commands can still be transferred to the spacecraft when the high gain antenna is not available.

An important component of the subsystem is the transponder. A transponder usually includes receiving, transmitting, and ranging functions. Serial data and clock signals for downlink telemetry and uplink command are incorporated. The processing of telemetry and telecommand is represented by a separate subsystem in Figure 7.4. A filter is used to eliminate noise and select a specific range of frequencies. Amplifiers increase the downlink power. Lastly, the Command and Data Handling System (C&DH) includes the onboard computer, memory units and required data buses. A specific challenge for this mission are the radiation environment in deep space. Radiation hardened components shall be used to mitigate the risk of damage. The C&DH system shall also feature redundancy such that radiation-induced failures do not critically affect the mission. Furthermore, the C&DH system shall able to handle the high data rates required to deal with the images generated for terminal guidance.

8

Conclusion

To begin the conclusions, the research questions are explicitly repeated and answered. The first research question is the following.

> (1) What is the design and mission concept of a kinetic impactor, optimized for the momentum transfer to the asteroid target?

In order to answer the research question, a criterion for an optimal deflection attempt has to be defined. The velocity change given to the asteroid is selected, because it encompasses the momentum enhancement and the spacecraft momentum. The momentum enhancement is modelled with scaling laws derived from impact simulations. The velocity change depends on the asteroid orbit as well as the incidence angle of the spacecraft. A hypothetical impact scenario is assumed, where a population of orbits is used as an input to determine the transfer trajectory from Earth to the asteroid. A number of design concepts, numbered from ID1 to ID7, are evaluated and the deflection performance is compared. The optimal concept is obtained by running the model for a range of departure dates and travel time from Earth to the asteroid. The velocity change, which is positively correlated to the momentum transfer, is determined and the maximum value is selected.

> (1.a) What is the high level spacecraft and mission design of the kinetic impactor?

In terms of the spacecraft design concept, an assembled impactor is a promising candidate for an effective planetary defense mission. For the concept ID1, the second stage of the launch vehicle stays attached to the spacecraft and is brought as additional impact mass to the asteroid for an improved deflection performance.

The low-thrust trajectory is generally less advantageous in terms of deflection performance than a ballistic transfer. Due to the launch vehicle payload capability, the spacecraft mass has an upper bound. Along the trajectory, the spent fuel reduces the impact mass, which is not compensated by the impact speed advantage due to the continuous acceleration. It was found that when the spacecraft completes a full revolution around the Sun before impacting the asteroid, the deflection is higher than for zero or two rotations. One revolution strikes a balance between fuel consumption and impact speed.

> (1.b) What are the sensitivities of the kinetic impactor design with respect to the design variables?

The sensitivity study on the impact parameters revealed that the scaling constants and therefore the asteroid properties have a large influence on the resulting β-factor. It was decided to choose a representative set of constants for an asteroid target and focus on the variables that can be controlled by the designer of the mission, which are mass and impact speed of the asteroid. These are the factors that have a large influence on the impact efficiency and can be significantly manipulated by the mission design.

The deflection performance is also sensitive to the asteroid orbit. The impact speed depends on the relative orbital velocity between the asteroid and the spacecraft. As such, depending on the exact

orbit geometry, the momentum transfer varies. In order to account for this effect, and to make a fair comparison between the proposed concepts, the transfer trajectory is evaluated for the same range of departure dates. Then the transfer with the maximum momentum is selected. A constant reference asteroid is chosen, with similar properties as Dimorphos, the target of the DART mission. The selected diameter are 150m, with a mass of $5 \cdot 10^9$ kg.

The choice of launch vehicle has an effect on the resulting performance. A super heavy-lift launch vehicle, like Falcon Heavy, has a high payload capability to Low-Earth orbit, resulting in a high impact mass for a spacecraft that departs with a bi-propellant propulsion system from a circular parking orbit and gives an average deflection performance of 0.562 m/s. For the European launcher Ariane 64, the configuration ID1 comes out on top, with an average deflection of 0.298 m/s. ID 1 is an assembled impactor, directly deployed onto the transfer trajectory by the launch vehicle.

The results for the deflection as a function of impact mass show that each configuration has a mass limit, which is determined by the characteristic energy required for the interplanetary transfer and the launcher payload capability.

The departure with a solid kick motor, either from a circular parking orbit or a GTO, does not show a significant advantage over the other methods. In a trade-off, taking into account secondary parameters, the assembled impactor is selected for further analysis. The analysis glances over the driving requirements for the spacecraft and highlights the passivation procedure of the second stage and the GNC system as critical subsystems. Also, the ground tracking is an important part of the mission operations.

The proposed assembled impactor is an improved system over the DART spacecraft and features the best deflection performance within the capabilities of the Ariane 64 launcher. The performance was evaluated for a large population of existing asteroids and is a realistic concept for a future planetary defense mission.

Limitations

The second set of research questions is dealing with the limits of the kinetic impactor concept and the implementation.

(2) What are the limits of applicability of the proposed kinetic impactor concept?

> (2.a) What are the limits of the parametric model implementation for the kinetic impactor design?

The limitations of the design framework have to be discussed. The scaling laws assume that the impact energy stems from a point source and that the asteroid is only locally affected. With increasingly higher impact energy, the risk of reshaping or dispersing parts of the asteroid increase. Close to the reshaping and dispersion threshold, the scaling laws are not valid. The scaling laws are based on numerical simulations and are validated with a single data point, the DART impact. The scaling laws for an oblique impact were shown to slightly underestimate the impact efficiency of DART.

The ballistic transfer trajectory is Keplerian, while the low-thrust transfer is assumed to have the shape of an exponential sinusoid. The assumption for the exponential sinusoid is that the thrust is always tangentially applied, while other control modes are possible. The influence of disturbing factors, such as other solar system bodies or propellant leaks are not taken into account and trajectory correction maneuvers are ignored. The patched conics approach and impulsive shot assumptions are popular tools for preliminary mission design and sufficiently accurate for the initial trade-off, but neglect the effect of gravity losses and simplify the Earth departure.

(2.b) What is the performance and the limits of the kinetic impactor concept in a realistic asteroid threat scenario?

The selection of the asteroid target is based on a catalog of observed asteroids. Due to the fact that it is more challenging to detect asteroids from Earth when they are close to the Sun, the population is biased towards Apollo asteroids.

Nevertheless, the potentially hazardous asteroids are filtered by a set of requirements that ensure a scenario that is representative of an impact scenario. The asteroids have to Near-Earth objects and have an Earth-crossing orbit.

The design framework assumes generic launch vehicle performances. Depending on the specific orbit requirements and the required inclination change, the available characteristic energy and payload capability might differ.

In terms of the required Δv for a successful deflection attempt, an analytical estimation is compared to the results. The estimation assumes a near-circular orbit for the asteroid, and requires a deflection of the asteroid by one Earth radius. The Δv requirement is given as a function of time remaining between the kinetic impact of the spacecraft and the projected impact of the asteroid on Earth. With the given setup in this thesis, the time remaining until impact is between 3 and 7 years. With those preconditions, it turns out that the average Δv of all options is roughly an order of magnitude higher and would be sufficient to deflect the object within the given time frame. The estimated required velocity change is between 0.01 m/s and 0.024 m/s, and the achieved deflection with an assembled impactor and Ariane 64 as the launch vehicle is on average 0.298 m/s with a 99% confidence interval between 0.284 m/s and 0.313 m/s. Further work is required to constrain the requirement for different impact scenarios.

Recommendations for future work

In terms of future work, the feasibility of an assembled impactor and the implications for the spacecraft design have to be further studied. The thesis reveals on a preliminary basis that an assembled impactor promises an advantage in deflection, due to the higher impact mass. It is suggested that the impact is numerically studied with hydrocodes, to confirm the predictions of the β-factor and the deflection. The behaviour of what is essentially a large hollow container, the second stage of the launch vehicle, in a hypervelocity impact shall be investigated.

A critical subsystem is Guidance, Navigation, and Control (GNC), and with an assembled impactor, certain challenges have to be dealt with. The coupling of orbital and attitude control, the center of gravity location and the impingement of thruster plumes on the second stage are areas of further study. The terminal guidance system has to be agile enough to steer the impactor towards the target. The control system design and the sizing of the actuators is an important step towards the realization of the proposed concept.

The theoretical framework developed in this thesis allows for a quick estimation of the deflection of an asteroid by a kinetic impactor. A range of departure dates and an allowed time of flight is given, as well as a selection of the launch vehicle. Further assumptions include the selection of a reference bi-propellant on-board propulsion system and a choice of available solid kick motors. Suitable departure windows are determined and the transfer trajectory, as well as the deflection performance is evaluated on a grid of departure dates and time of flights. The inputs are subject to further study, when the characteristics of the spacecraft are determined in more detail, such as the system mass, the propulsion system efficiency and the choice of components.

The thesis does not investigate the actual deflection needed to avoid an Earth impact. The requirement is analytically derived, but only for a general case and not for each of the specific impact scenarios. Therefore, it is worth investigating which design options provides a sufficient deflection for which part of the NEO population.

In summary, the thesis contributes to the body of research by integrating the β-estimation in a preliminary design tool and giving an indication what overall architecture is advantageous for a future kinetic impactor mission. The next steps are to investigate the proposed concept in terms of practical aspects.

References

[1] Thomas J. Ahrens and Alan W. Harris. “Deflection and fragmentation of near-Earth asteroids”. In: *Nature* 360.6403 (Dec. 1992). Number: 6403 Publisher: Nature Publishing Group, pp. 429–433. ISSN: 1476-4687. DOI: 10.1038/360429a0. URL: https://www.nature.com/articles/360429a0 (visited on 10/24/2023).

[2] Masahiko Arakawa et al. “An artificial impact on the asteroid 162173 Ryugu formed a crater in the gravity-dominated regime”. In: *Science* 368 (Mar. 19, 2020), eaaz1701. DOI: 10.1126/science.aaz1701.

[3] Arianespace. *Ariane 6 User’s Manual*. Feb. 2021. URL: https://www.arianespace.com/wp-content/uploads/2021/03/Mua-6_Issue-2_Revision-0_March-2021.pdf.

[4] Justin Atchison et al. “Dart Mission Design and Navigation Lessons learned for future Planetary Defense Missions”. In: Apr. 3, 2023.

[5] Julie Bellerose et al. “Double Asteroid Redirection Test (DART): Navigating to obliteration”. In: *Acta Astronautica* 219 (June 1, 2024), pp. 417–427. ISSN: 0094-5765. DOI: 10.1016/j.actaastro.2024.02.021. URL: https://www.sciencedirect.com/science/article/pii/S0094576524000857 (visited on 05/28/2024).

[6] Mark Carney. *Performance Website*. NASA Launch Services Program. Feb. 29, 2024. URL: https://elvperf.ksc.nasa.gov/Pages/Default.aspx (visited on 05/23/2024).

[7] Nancy Chabot et al. “DART: Latest results from the Dimorphos impact and a look forward to future planetary defense initiatives”. In: *Acta Astronautica* 220 (July 1, 2024), pp. 118–125. ISSN: 0094-5765. DOI: 10.1016/j.actaastro.2024.04.001. URL: https://www.sciencedirect.com/science/article/pii/S0094576524002005 (visited on 06/30/2024).

[8] Andrew F. Cheng et al. “Momentum transfer from the DART mission kinetic impact on asteroid Dimorphos”. In: *Nature* 616.7957 (Apr. 2023). Number: 7957 Publisher: Nature Publishing Group, pp. 457–460. ISSN: 1476-4687. DOI: 10.1038/s41586-023-05878-z. URL: https://www.nature.com/articles/s41586-023-05878-z (visited on 07/09/2023).

[9] Andrew. F. Cheng et al. “Asteroid Impact & Deflection Assessment mission: Kinetic impactor”. In: *Planetary and Space Science* 121 (Feb. 1, 2016), pp. 27–35. ISSN: 0032-0633. DOI: 10.1016/j.pss.2015.12.004. URL: https://www.sciencedirect.com/science/article/pii/S0032063315300337 (visited on 10/17/2023).

[10] Space Exploration Technologies Corp. *Falcon User’s Guide*. Sept. 2021. URL: https://www.spacex.com/media/falcon-users-guide-2021-09.pdf.

[11] Howard D. Curtis. “Chapter 5 - Preliminary Orbit Determination”. In: *Orbital Mechanics for Engineering Students (Third Edition)*. Ed. by Howard D. Curtis. Third Edition. Boston: Butterworth-Heinemann, 2014, pp. 239–298. ISBN: 978-0-08-097747-8. DOI: https://doi.org/10.1016/B978-0-08-097747-8.00005-0. URL: https://www.sciencedirect.com/science/article/pii/B9780080977478000050.

[12] R. Terik Daly et al. “Successful kinetic impact into an asteroid for planetary defence”. In: *Nature* 616.7957 (Apr. 2023). Number: 7957 Publisher: Nature Publishing Group, pp. 443–447. ISSN: 1476-4687. DOI: 10.1038/s41586-023-05810-5. URL: https://www.nature.com/articles/s41586-023-05810-5 (visited on 07/09/2023).

[13] *Definitions & Assumptions*. European Space Agency Near-Earth Objects Coordination Centre. URL: https://neo.ssa.esa.int/definitions-assumptions (visited on 05/21/2024).

[14] European Cooperation for Space Standardization. *Satellite attitude and orbit control system (AOCS) requirements*. Standard ECSS-E-ST-60-30C. ECSS, 2013.

[15] Jack Fisher. “NEXT-C Flight Ion System Status”. In: *AIAA Propulsion and Energy 2020 Forum*. _eprint: https://arc.aiaa.org/doi/pdf/10.2514/6.2020-3604. American Institute of Aeronautics and Astronautics, Aug. 17, 2020. DOI: 10.2514/6.2020-3604. URL: https://arc.aiaa.org/doi/abs/10.2514/6.2020-3604 (visited on 11/07/2023).

[16] Bevan M. French. *Traces of Catastrophe: A Handbook of Shock-Metamorphic Effects in Terrestrial Meteorite Impact Structure*. LPI Contribution 954. Houston: Lunar and Planetary Institute, 1998. URL: https://ntrs.nasa.gov/citations/19990071201 (visited on 10/16/2023).

[17] Ken Galal et al. “Trajectory Design and Orbit Determination for the Lunar CRater Observation and Sensing Satellite (LCROSS)”. In: *Proceedings of the 20th International Symposium on Space Flight Dynamics* (Sept. 24, 2007). URL: https://ntrs.nasa.gov/citations/20080012691 (visited on 05/27/2024).

[18] Herbert Goldstein, Charles Poole, and John Safko. *Classical Mechanics*. 3rd. Addison-Wesley, 2002.

[19] Sheng-Ping Gong, Jun-Feng Li, and Xiang-Yuan Zeng. “Utilization of an H-reversal trajectory of a solar sail for asteroid deflection”. In: *Research in Astronomy and Astrophysics* 11.10 (Oct. 2011), pp. 1123–1133. ISSN: 1674-4527. DOI: 10.1088/1674-4527/11/10/001. URL: https://iopscience.iop.org/article/10.1088/1674-4527/11/10/001 (visited on 05/27/2024).

[20] Tyler Gray. *A new era: Ariane 6 maiden launch campaign gets underway*. NASASpaceFlight.com. Apr. 27, 2024. URL: https://www.nasaspaceflight.com/2024/04/ariane-6-maiden-launch-campaign/ (visited on 05/23/2024).

[21] Northrop Grumman. *Propulsion Products Catalog*. 2016. URL: https://cdn.northropgrumman.com/-/media/wp-content/uploads/NG-Propulsion-Products-Catalog.pdf.

[22] Charles R. Harris et al. “Array programming with NumPy”. In: *Nature* 585.7825 (2020), pp. 357–362. DOI: 10.1038/s41586-020-2649-2.

[23] Keith A. Holsapple and Kevin R. Housen. “Deflecting Asteroids by Impacts: What is Beta?” In: *Lunar and Planetary Institute Science Conference Abstracts* 43 (Mar. 1, 2012), p. 2539.

[24] Keith A. Holsapple and Kevin R. Housen. “Momentum transfer in asteroid impacts. I. Theory and scaling”. In: *Icarus* 221.2 (Nov. 1, 2012), pp. 875–887. ISSN: 0019-1035. DOI: 10.1016/j.icarus.2012.09.022. URL: https://www.sciencedirect.com/science/article/pii/S0019103512003958 (visited on 09/01/2023).

[25] Keith A. Holsapple and Kevin R. Housen. “The catastrophic disruptions of asteroids: History, features, new constraints and interpretations”. In: *Planetary and Space Science* 179 (Dec. 1, 2019), p. 104724. ISSN: 0032-0633. DOI: 10.1016/j.pss.2019.104724. URL: https://www.sciencedirect.com/science/article/pii/S0032063319300509 (visited on 11/18/2023).

[26] Keith A. Holsapple and Robert Schmidt. “Point source solutions and coupling parameters in cratering mechanics”. In: *Journal of Geophysical Research Atmospheres* 92 (July 10, 1987). DOI: 10.1029/JB092iB07p06350.

[27] Kevin R. Housen and Keith A. Holsapple. “Ejecta from impact craters”. In: *Icarus* 211.1 (Jan. 1, 2011), pp. 856–875. ISSN: 0019-1035. DOI: 10.1016/j.icarus.2010.09.017. URL: https://www.sciencedirect.com/science/article/pii/S0019103510003623 (visited on 09/22/2023).

[28] Dario Izzo. *esa/pykep: Official Release of 2016*. Version v1.3.9. 2016. DOI: 10.5281/zenodo.168378. URL: https://doi.org/10.5281/zenodo.168378.

[29] Dario Izzo. “Lambert’s Problem for Exponential Sinusoids”. In: *Journal of Guidance Control and Dynamics* 29 (Sept. 1, 2006), pp. 1242–1245. DOI: 10.2514/1.21796.

[30] Roberto Maddè et al. “Delta-DOR - a new technique for ESA’s Deep Space Navigation”. In: *ESA Bulletin* 128 (Nov. 1, 2006). ADS Bibcode: 2006ESABu.128...68M, pp. 68–74. ISSN: 0376-4265. URL: https://ui.adsabs.harvard.edu/abs/2006ESABu.128...68M (visited on 06/06/2024).

[31] P. Martino et al. “RAMSES — ESAs Study for a Small Mission to Apophis”. In: 2851 (Aug. 2023). ADS Bibcode: 2023LPICo2851.2011M, p. 2011. URL: https://ui.adsabs.harvard.edu/abs/2023LPICo2851.2011M (visited on 05/23/2024).

[32] Patrick Michel et al. “The ESA Hera Mission: Detailed Characterization of the DART Impact Outcome and of the Binary Asteroid (65803) Didymos”. In: *The Planetary Science Journal* 3 (July 1, 2022), p. 160. DOI: 10.3847/PSJ/ac6f52.

[33] Lester Morales. “Return to the Moon: NASA’s LCROSS AND LRO Missions”. In: 2012 Science and Creativity Annual Conference. Dec. 6, 2012. URL: https://ntrs.nasa.gov/citations/20130001563 (visited on 05/27/2024).

[34] Andres Moreno Gonzalez. “Characterisation of Shape-Based Methods and Combination with Coasting Arcs”. PhD thesis. Delft University of Technology, 2020. URL: https://repository.tudelft.nl/islandora/object/uuid%3A1ef439eb-d267-4df8-92d1-2f0fcb2d7be2 (visited on 05/21/2024).

[35] David Morrison. “The Cosmic Impact Hazard”. In: *Planetary Defense: Global Collaboration for Defending Earth from Asteroids and Comets*. Ed. by Nikola Schmidt. Cham: Springer International Publishing, 2019, pp. 15–32. ISBN: 978-3-030-01000-3. DOI: 10.1007/978-3-030-01000-3_2. URL: https://doi.org/10.1007/978-3-030-01000-3_2 (visited on 06/30/2024).

[36] Anastassios E. Petropoulos and James M. Longuski. “Shape-Based Algorithm for the Automated Design of Low-Thrust, Gravity Assist Trajectories”. In: *Journal of Spacecraft and Rockets* 41.5 (Sept. 2004). Publisher: American Institute of Aeronautics and Astronautics, pp. 787–796. ISSN: 0022-4650. DOI: 10.2514/1.13095. URL: https://arc.aiaa.org/doi/10.2514/1.13095 (visited on 05/21/2024).

[37] Anastassios E. Petropoulos et al. “1st ACT global trajectory optimisation competition: Results found at the Jet Propulsion Laboratory”. In: *Acta Astronautica*. Global Trajectory Optimization. Results of the First Competition Organised by the Advanced Concept Team (ACT) of the European Space Agency (ESA) 61.9 (Nov. 1, 2007), pp. 806–815. ISSN: 0094-5765. DOI: 10.1016/j.actaastro.2007.03.013. URL: https://www.sciencedirect.com/science/article/pii/S0094576507001750 (visited on 05/27/2024).

[38] Olga P. Popova et al. “Chelyabinsk Airburst, Damage Assessment, Meteorite Recovery, and Characterization”. In: *Science* 342.6162 (Nov. 29, 2013). Publisher: American Association for the Advancement of Science, pp. 1069–1073. DOI: 10.1126/science.1242642. URL: https://www.science.org/doi/10.1126/science.1242642 (visited on 10/20/2023).

[39] Sabina Raducan. “Deflecting rubble pile asteroids: Lessons learned from the DART impact on Dimorphos”. 8th Planetary Defense Conference. Vienna, Apr. 2023. (Visited on 07/23/2024).

[40] Sabina D. Raducan, Thomas M. Davison, and Gareth S. Collins. “Ejecta distribution and momentum transfer from oblique impacts on asteroid surfaces”. In: *Icarus* 374 (Mar. 1, 2022). Publisher: Academic Press, p. 114793. ISSN: 0019-1035. DOI: 10.1016/j.icarus.2021.114793. URL: https://www.sciencedirect.com/science/article/pii/S0019103521004425 (visited on 07/09/2023).

[41] Sabina D. Raducan and Martin Jutzi. “Global-scale Reshaping and Resurfacing of Asteroids by Small-scale Impacts, with Applications to the DART and Hera Missions”. In: *The Planetary Science Journal* 3.6 (June 1, 2022). Publisher: IOP Publishing, p. 128. ISSN: 2632-3338. DOI: 10.3847/PSJ/ac67a7. URL: https://iopscience.iop.org/article/10.3847/PSJ/ac67a7/meta (visited on 10/25/2023).

[42] Sabina D. Raducan et al. “The role of asteroid strength, porosity and internal friction in impact momentum transfer”. In: *Icarus* 329 (Sept. 1, 2019), pp. 282–295. ISSN: 0019-1035. DOI: 10.1016/j.icarus.2019.03.040. URL: https://www.sciencedirect.com/science/article/pii/S0019103518305645 (visited on 10/13/2023).

[43] Kyle J. Ryan et al. “Design of the Didymos Reconnaissance and Asteroid Camera for OpNav (DRACO) on the double asteroid redirection test (DART)”. In: *Space Telescopes and Instrumentation 2018: Optical, Infrared, and Millimeter Wave*. Space Telescopes and Instrumentation 2018: Optical, Infrared, and Millimeter Wave. Ed. by Howard A. MacEwen et al. Austin, United States: SPIE, July 6, 2018, p. 67. ISBN: 978-1-5106-1949-4 978-1-5106-1950-0. DOI: 10.1117/12.2310136. URL: https://www.spiedigitallibrary.org/conference-proceedings-of-spie/10698/2310136/Design-of-the-Didymos-Reconnaissance-and-Asteroid-Camera-for-OpNav/10.1117/12.2310136.full (visited on 06/02/2024).

[44] Peter Schulte et al. “The Chicxulub Asteroid Impact and Mass Extinction at the Cretaceous-Paleogene Boundary”. In: *Science (New York, N.Y.)* 327 (Mar. 2010), pp. 1214–8. DOI: 10.1126/science.1177265.

[45] Angela M. Stickle et al. “Effects of Impact and Target Parameters on the Results of a Kinetic Impactor: Predictions for the Double Asteroid Redirection Test (DART) Mission”. In: *The Planetary Science Journal* 3.11 (Nov. 4, 2022). Publisher: IOP Publishing, p. 248. ISSN: 2632-3338. DOI: 10.3847/PSJ/ac91cc. URL: https://iopscience.iop.org/article/10.3847/PSJ/ac91cc/meta (visited on 07/09/2023).

[46] Paul D. Tompkins et al. “Flight Operations for the LCROSS Lunar Impactor Mission”. In: SpaceOps 2010. NTRS Author Affiliations: Stinger Ghaffarin Technologies, Inc., NASA Ames Research Center, Northrop Grumman Aerospace Systems NTRS Report/Patent Number: ARC-E-DAA-TN1247 NTRS Document ID: 20100026403 NTRS Research Center: Ames Research Center (ARC). Huntsville, AL, Apr. 25, 2010. URL: https://ntrs.nasa.gov/citations/20100026403 (visited on 06/29/2024).

[47] The International Astronomical Union. *The MPC Orbit (MPCORB) Database*. URL: https://www.minorplanetcenter.net/iau/MPCORB.html (visited on 06/25/2024).

[48] LLC United Launch Alliance. *Vulcan Launch Systems User’s Guide*. Oct. 2023. URL: https://www.ulalaunch.com/docs/default-source/rockets/2023_vulcan_user_guide.pdf?sfvrsn=e9cc773f_4.

[49] Pauli Virtanen et al. “SciPy 1.0: Fundamental Algorithms for Scientific Computing in Python”. In: *Nature Methods* 17 (2020), pp. 261–272. DOI: 10.1038/s41592-019-0686-2.

[50] *Vulcan Cert-1*. URL: https://www.ulalaunch.com/missions/archived-launched/vulcan-cert-1 (visited on 05/23/2024).

[51] Yirui Wang et al. “Assembled kinetic impactor for deflecting asteroids by combining the spacecraft with the launch vehicle upper stage”. In: *Icarus* 368 (Nov. 1, 2021), p. 114596. ISSN: 0019-1035. DOI: 10.1016/j.icarus.2021.114596. URL: https://www.sciencedirect.com/science/article/pii/S001910352100261X (visited on 07/09/2023).

[52] Barry T. C. Zandbergen. *Aerospace Design and Systems Engineering Elements I. Spacecraft (bus) Design and Sizing: AE 1201*. TU Delft, 2010.

A

Table of constants and parameters used in the impact calculation

Table A.1: The dimensionless scaling constants used in the scaling laws.

Name	Symbol	Value	Comment
Velocity scaling constant.	C_1	1.108	
Velocity scaling exponent.	μ	0.42	
Mass scaling constant.	k	0.392	
Lower ejecta velocity cut-off.	n_1	1.2	
Upper ejecta velocity cut-off.	n_2	1	
Density scaling exponent.	ν	0.4	
Crater radius scaling constant in the gravity regime.	H_1	0.8	
Crater radius scaling constant in the strength regime.	H_2	0.48	
Low-speed ejecta constant.	p	0.3	
High-speed ejecta constant.	q	0.2	

Table A.2: The physical parameters used in the scaling laws.

Name	Symbol	Value	Unit	Comment
Impactor radius.	a	2.3	m	
Target density.	ρ	2400	kg/m^3	
Impactor density.	δ	1000	kg/m^3	
Target porosity.	Φ	20	%	Not applied.
Target strength.	Y	27.5	Pa	
Target radius.	r	75	m	
Impact angle.	θ	90	deg	
Ejection angle.	γ	45	deg	

B

Detailed flow chart

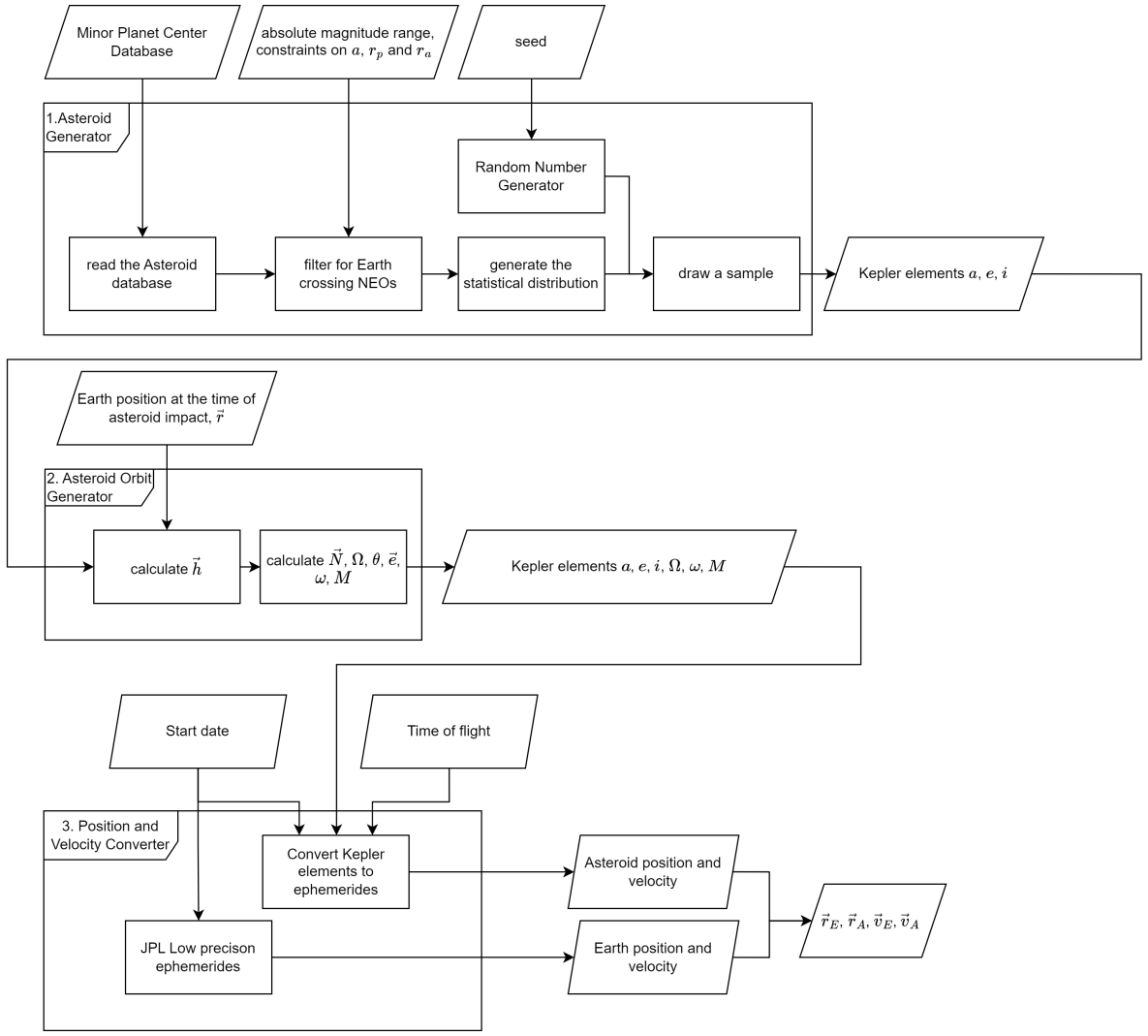

Figure B.1: The flow chart describes how the asteroid orbit is generated and the position and velocity of Earth and the asteroid is determined.

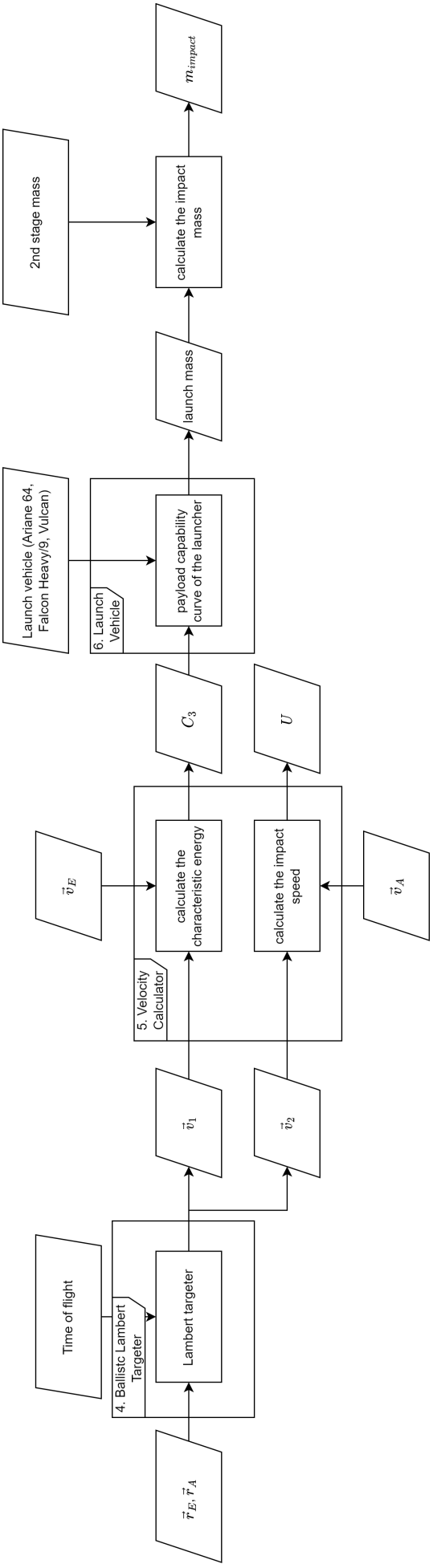

Figure B.2: The process to determine the impact mass for the direct insertion of a kinetic impactor into the transfer trajectory.

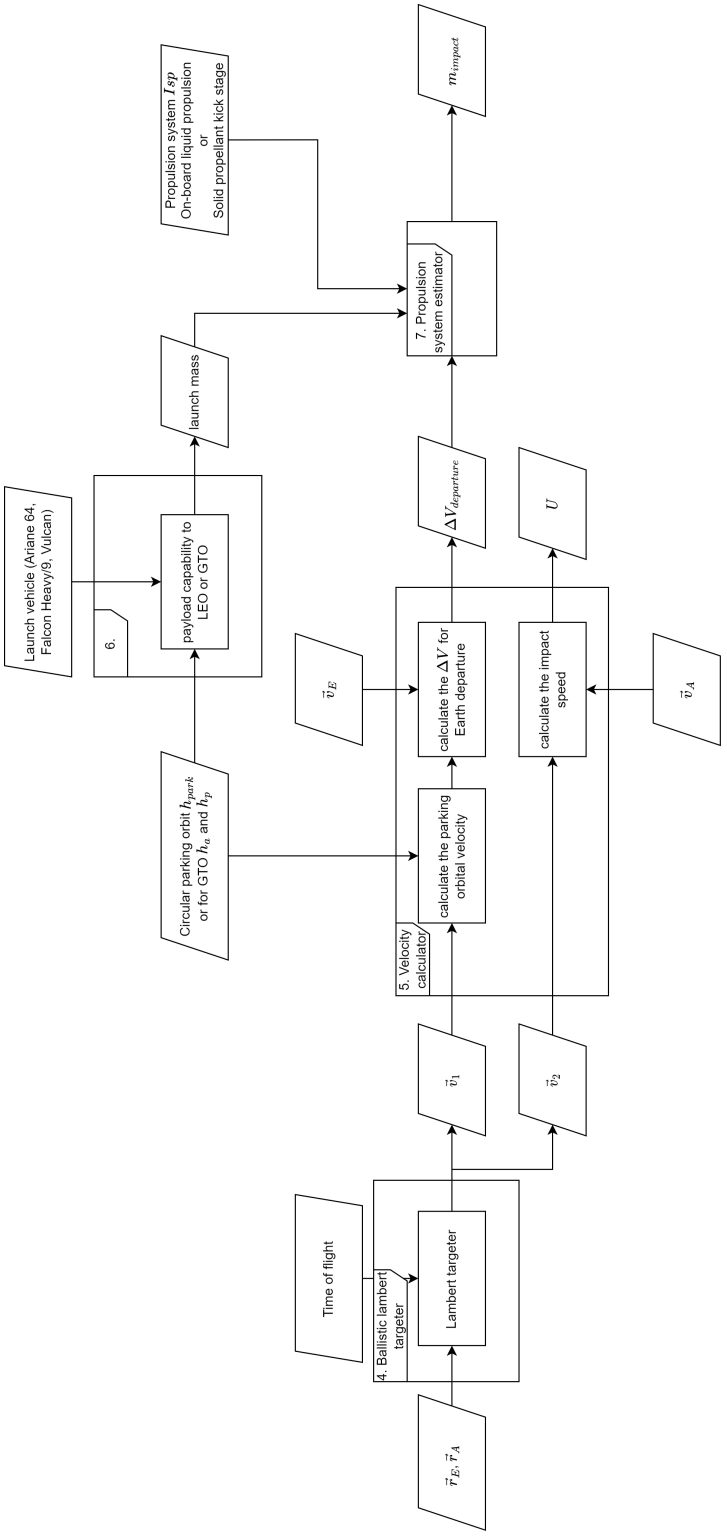

Figure B.3: The process to determine the impact mass for a kinetic impactor departing from a parking orbit.

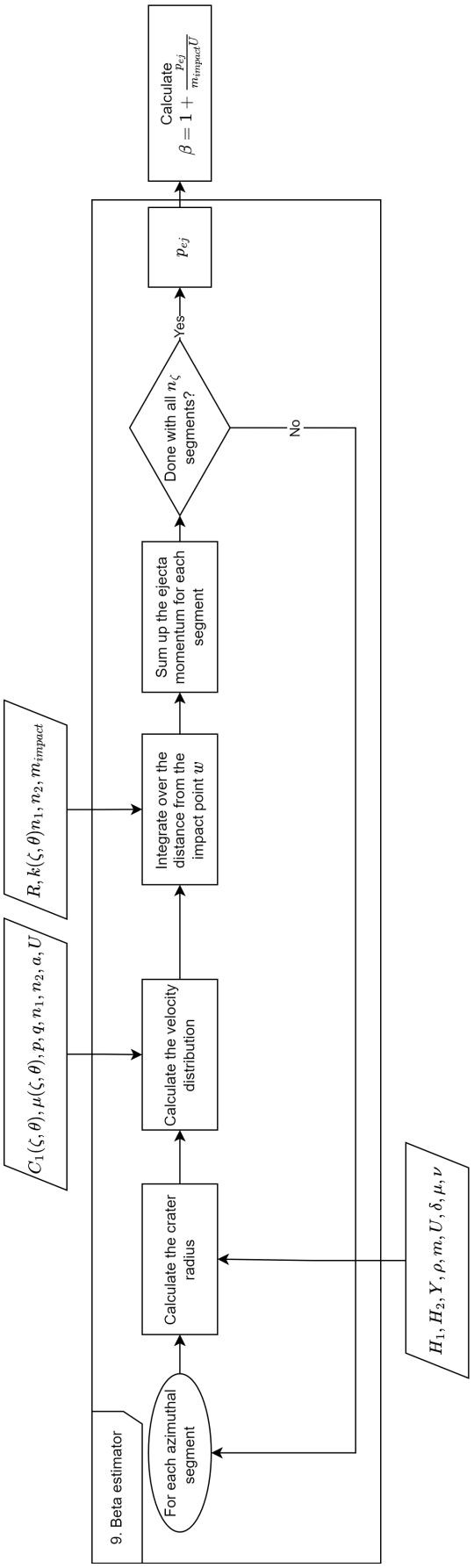

Figure B.4: The flow chart for estimating the momentum enhancement β.

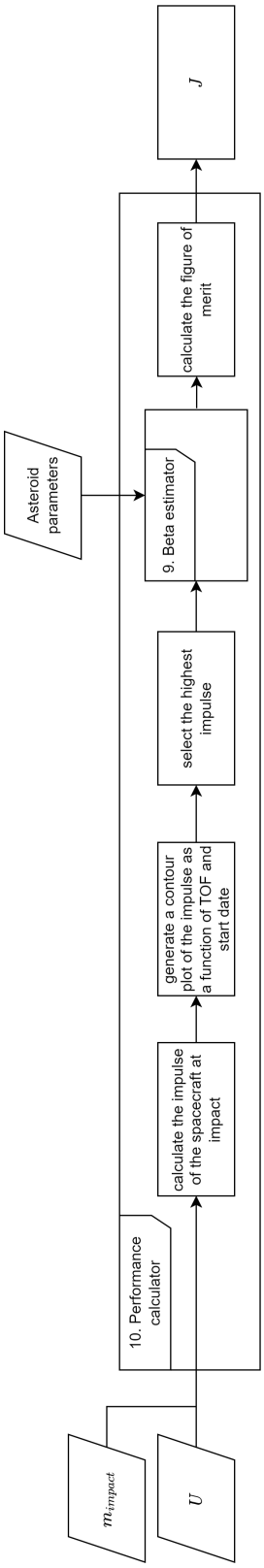

Figure B.5: The flow chart for determining the deflection J

C

Deflection results for a multivariate normal distribution

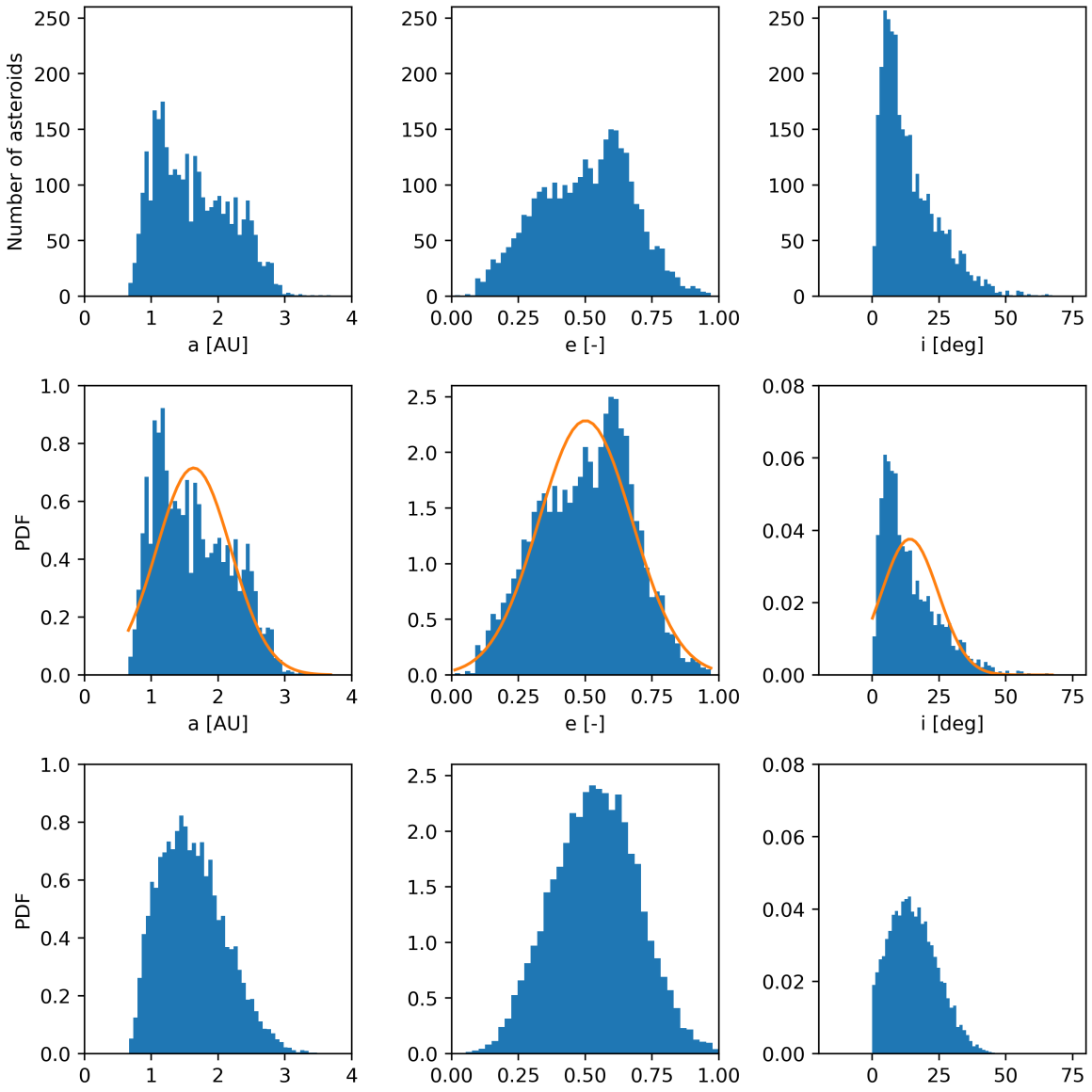

Figure C.1: The first row is the original dataset of Earth-Crossing Near-Earth Asteroids with an absolute magnitude between 21.2 and 23, corresponding to a 150m asteroid. The second row is the normalized distribution with an overlay of a normal distribution. The last row is the recreated distribution by drawing samples from the multivariate distribution.

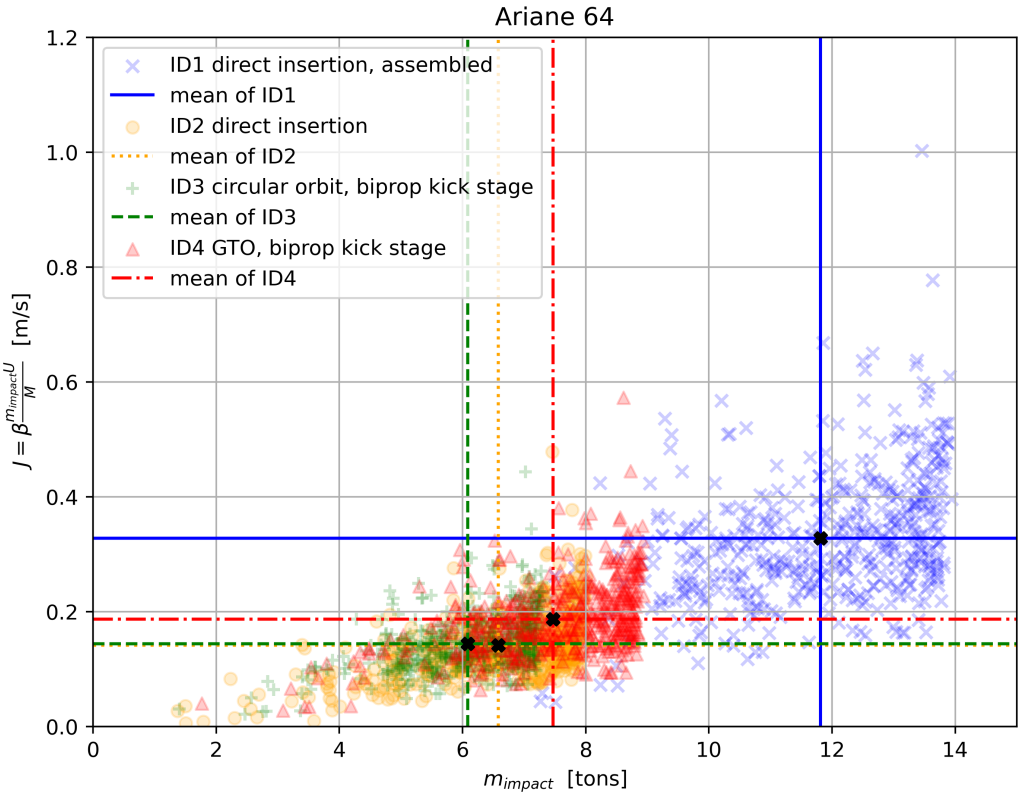

Figure C.2: The deflection performance for 500 asteroid cases from a multivariate normal distribution for configurations ID1 through ID4.

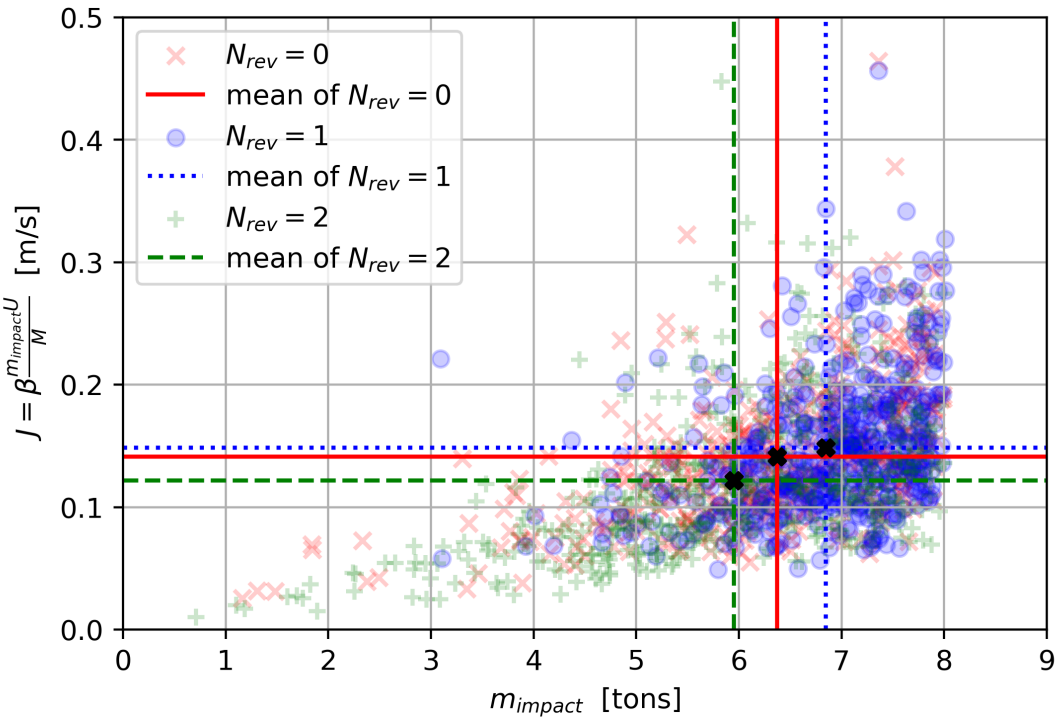

Figure C.3: The deflection performance for 500 asteroid cases from a multivariate normal distribution for configuration ID5, a low-thrust transfer trajectory as a function of allowed revolutions.

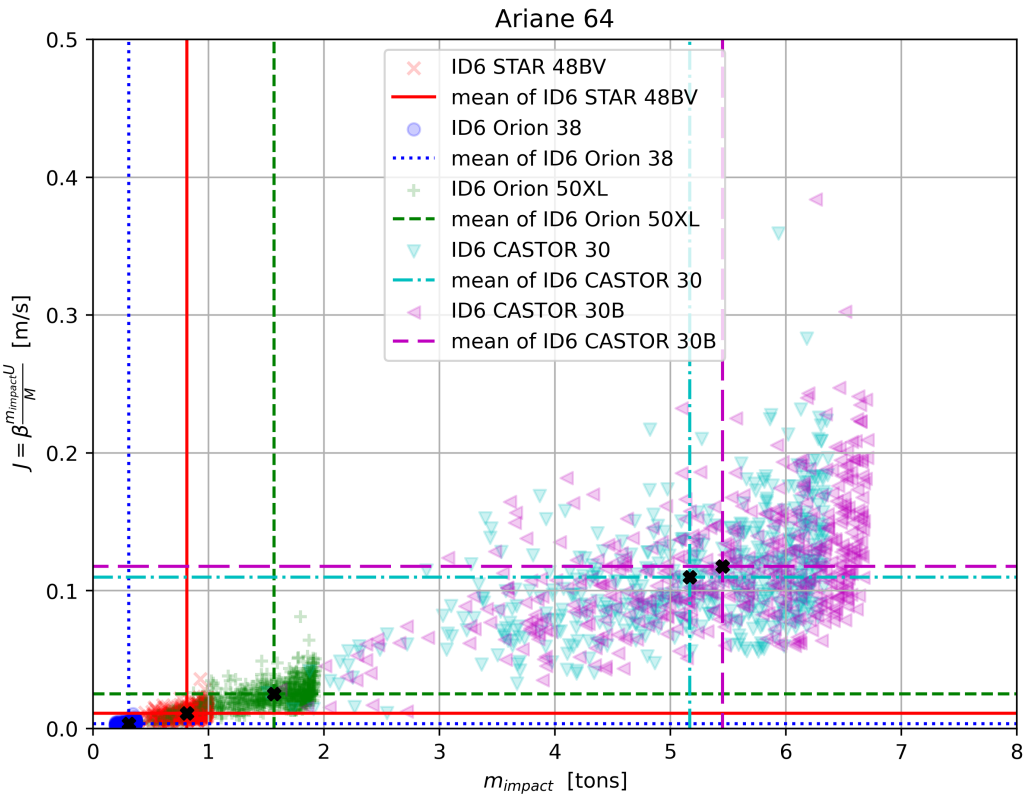

Figure C.4: The deflection performance for 500 asteroid cases from a multivariate normal distribution for configuration ID6, as a function of solid kick motor.

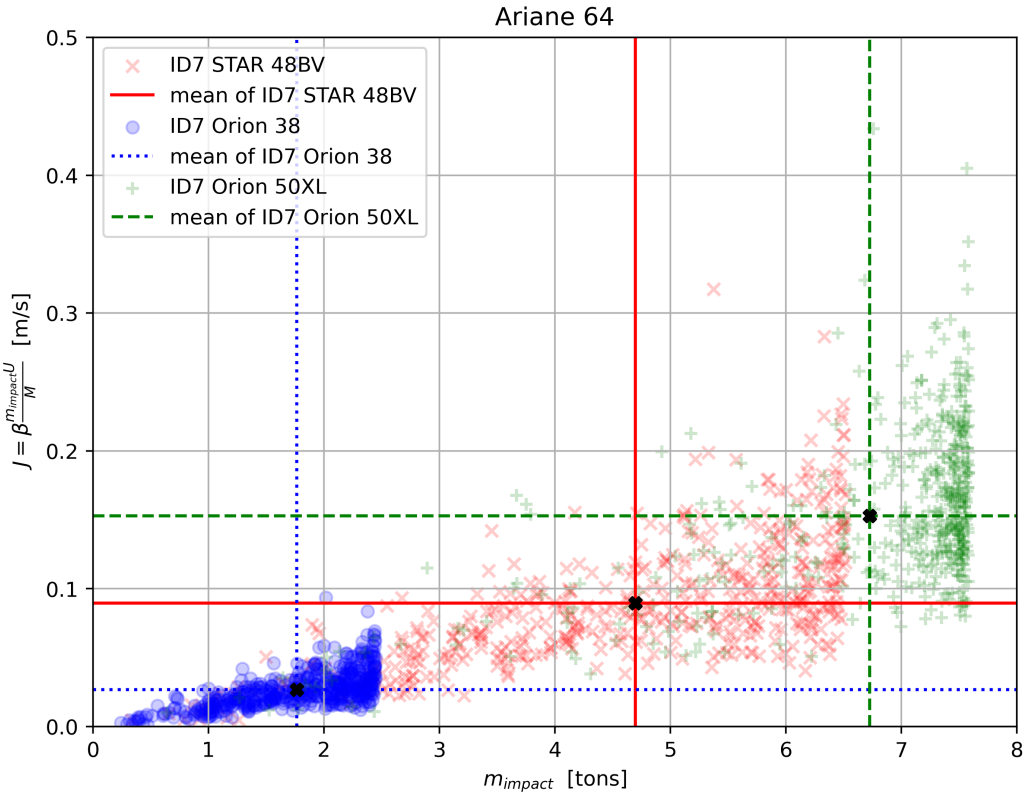

Figure C.5: The deflection performance for 500 asteroid cases from a multivariate normal distribution for configuration ID7, as a function of solid kick motor and departure from a GTO.